THE UNIVERSITY OF MANITOBA

RECONSTRUCTION OF ANTENNA FIELDS IN PRESENCE OF A DIELECTRIC SCATTERER

by

MOHAMED EL-BAKRY EL-ARINI

A THESIS
SUBMITTED TO THE FACULTY OF GRADUATE STUDIES
IN PARTIAL FULFILLMENT
OF THE REQUIREMENTS FOR THE DEGREE OF
DOCTOR OF PHILOSOPHY

DEPARTMENT OF ELECTRICAL ENGINEERING

WINNIPEG, MANITOBA
August 1980

RECONSTRUCTION OF ANTENNA FIELDS IN PRESENCE OF A DIELECTRIC SCATTERER

BY

MOHAMED EL-BAKRY AHMED HELMY EL-ARINI

A thesis submitted to the Faculty of Graduate Studies of the University of Manitoba in partial fulfillment of the requirements of the degree of

DOCTOR OF PHILOSOPHY

TO MY WIFE,

MY PARENTS,

MY SISTERS AND BROTHERS

ABSTRACT

A technique for reconstructing fields using scattering data is developed in this thesis. The problem consists of a dielectric scatterer; i.e., a sphere (or a cylinder), in the vicinity of an antenna whose radiation field is unknown. The technique calculates the near-field of the antenna from experimentally determined total fields near the antenna. From the calculated near-field, the far-field radiation pattern of the isolated antenna, or, the antenna and the scatterer combination is determined. The problem has practical significance since dielectric scatterers are used to shape the radiation patterns of horns, wave-guides and other radiating systems. Dielectric scatterers are also used to scatter the primary field of the antennas. In this manner, the wide angle scattering increases the signal strength in the regions of weak primary field and facilitates the accurate measurement of the near-field especially for the high gain antennas. In addition, this improvement of the field strength enables one to carry out the field measurement on a larger surface than it is normally feasible.

To avoid large scanning systems, required for large

antennas, a stepwise measurement technique is proposed and is developed in this thesis. In this technique, the near-field is measured over a small surface in the vicinity of the scatterer. The required information on the field over a surface enclosing the antenna is then obtained by repeating the measurements at several locations around the antenna. The stepwise approach not only reduces the required scanning surface, but also reduces the expansion of antenna field over a large surface to several expansions over small surfaces.

The analytical expressions for reconstruction of two- and three-dimensional fields are presented. The method is then applied to reconstruct the field of certain elementary sources, such as, a plane wave, an electric dipole and an array of electric dipoles. The effects of various parameters on the accuracy of the reconstructed fields and the usefulness of the stepwise approach are studied in detail.

ACKNOWLEDGEMENTS

The author wishes to express his gratitude to Professor L. Shafai for his guidance, and encouragement not only during the preparation of this thesis, but throughout his entire Ph.D. graduate program. The author would also wish to thank his Advisory Committee members; Professors L. Shafai, W. Lehn, A. Wexler and J.J. Williams for their guidance, help and discussions during his graduate program.

The author would like to thank Dr. A. Mohsen and Dr. F. Rahman for their reviewing of the first manuscript of this thesis.

The financial assistance of the University of Manitoba through a graduate fellowship is greatly appreciated.

Special thanks are also extended to Mrs. Paulette Giardino for her expert typing of the manuscript in the minimum time.

The use of the computing facilities at the University of Manitoba, is also acknowledged.

Special thanks to the author's wife for her patience and encouragement during his study, also for her help for preparing this thesis.

TABLE OF CONTENTS

Page

LIST OF FIGURES

Figure | Page

Figure | Page

Figure | Page

Figure | Page

LIST OF TABLES

LIST OF SYMBOLS

Unless otherwise stated, the symbols most commonly used in this thesis have the following meaning.

Greek Symbols

$\underline{\alpha}$, $\underline{\beta}$	vectors of unknown cylindrical expansion coefficients
ε	permittivity
ε_o	free space permittivity
ε_r	relative permittivity
ε_d	permittivity of the dielectric scatterer material
ε_m =	$\begin{cases} 2 & \text{for } m=0 \\ 1 & \text{for } m\neq o \end{cases}$
η	intrinsic impedance of free space $\simeq 120\ \pi$
θ_a, θ_b	limiting computational aspect angles
θ_r	location of the r^{th} measurement point
θ_{c_i}	the angular location of the center of the i^{th} measurement sphere
λ	free space wavelength
λ_d	the wavelength inside the dielectric scatterer
μ	permeability
μ_o	free space permeability
μ_r	relative permeability
μ_d	permeability of the dielectric scatterer material

π	Pi (3.141592654)
(ρ,ϕ,z)	cylindrical coordinate system
ρ_s	surface electric charge density
ψ	scalar Green's function
ψ_n	elementary cylindrical wave functions
ω	angular frequency, radians/sec.

Latin Symbols

a	radius of dielectric cylinder or sphere
a_n, b_n, c_n, d_n, e_n	cylindrical expansion coefficients of the electromagnetic field
a^{e}_{mn} , b^{e}_{mn}	spherical expansion coefficients of the incident field
A	radius of measurement cylinder or sphere
$\underline{A}$	magnetic vector potential
A^{e}_{mn} , B^{e}_{mn}	spherical expansion coefficients of the incident field on the measurement sphere
c^{e}_{mn} , d^{e}_{mn}	spherical expansion coefficients of the scattered field
d	separation between the center of the dielectric sphere and the phase center of the dipole array
db	decibel
D	largest dimension of the aperture of the antenna
e	base of natural logarithms

e,o	subscripts denote even and odd azimuthal (ϕ-coordinate) dependence
e_{mn}^{e} , f_{mn}^{e}	spherical expansion coefficients of the total field inside the scatterer
$\underline{E}$	electric field vector
$\underline{E}^{i}$, $\underline{E}^{s}$	incident and scattered electric field vectors
E_r, E_θ, E_ϕ	spherical components of the electric field vector
E_ρ, E_ϕ, E_z	cylindrical components of the electric field vector
E_o	amplitude of the incident field
$h_n^{(1)}$, $h_n^{(2)}$	spherical Hankel functions of the first and second kind of order n.
$\hat{H}_n^{(1)}$, $\hat{H}_n^{(2)}$	spherical Riccati-Hankel functions of the first and second kind of order n
$H_n^{(1)}$, $H_n^{(2)}$	cylindrical Hankel functions of the first and second kind of order n
$\underline{H}$	magnetic field vector
$\underline{H}^{i}$, $\underline{H}^{s}$	incident and scattered magnetic field vectors
H_r, H_θ, H_ϕ	spherical components of the magnetic field vector
H_ρ, H_ϕ, H_z	cylindrical components of the magnetic field vector
(i)	subscript represents type of the radial propagation function = (1),(2),(3), or (4)
$\hat{i}_x$, $\hat{i}_y$, $\hat{i}_z$	unit vectors in the Cartesian coordinate sytem
$\hat{i}_r$, $\hat{i}_\theta$, $\hat{i}_\phi$	unit vectors in the Spherical coordinate system
$\hat{i}_\rho$, $\hat{i}_\phi$, $\hat{i}_z$	unit vectors in the Cylindrical coordinate system

$I\underline{\ell}$	moment of the electric dipole
j	$\sqrt{-1}$
j_n, $\hat{J}_n$, J_n	spherical, spherical Riccati-type and cylindrical Bessel functions of the first kind
k	propagation constant
k_o	free space propagation constant
k_d	propagation constant inside the dielectric scatterer
$\underline{K}$	surface electric current density vector
m,n	eigen values of the ϕ and θ coordinates in the spherical coordinate system
$\underline{m}^{(i)}_{e_{mn}}$, $\underline{n}^{(i)}_{e_{mn}}$	spherical vector wave functions
O^m_N	optimization function at constant m and number of measurement points N
$P^m_n(\cos\theta)$	associated Legendre polynomial of first kind of order m and degree n
(r, θ, ϕ)	spherical coordinate system
$\underline{r}_o \equiv (x_o, y_o, z_o)$ $\equiv (r_o, \theta_o, \phi_o)$	location of the dipole
$\lvert\underline{r} - \underline{r}'\rvert$	distance between the field point and source point
R	distance between the antenna aperture and the boundary of the near-field and far-field regions
s_{1ij}, s_{2ij}	elements of the matrices $[S_1]$ and $[S_2]$
$[S]$, $[S_1]$, $[S_2]$	matrices

S	spherical surface enclosing the antenna
S'	spherical surface enclosing the antenna and scatterer
S_1, S_2, S_3	measurement spheres
S_1', S_2', S_3'	expansion spheres
t	time
(x,y,z)	Cartesian coordinate system
y_n, $\hat{Y}_n$, Y_n	spherical, spherical Riccati-type and cylindrical Bessel functions of the second kind
$z_n^{(i)}$, $\hat{Z}_n^{(i)}$, $Z_n^{(i)}$	spherical, spherical Riccati-type and cylindrical radial function

CHAPTER I

INTRODUCTION

Recently, the near-field measurement techniques are receiving an increasing attention for determining the antenna radiation characteristics. Existing literature in the area is numerous, but a general survey of the subject is available in [1] and [2]. Because the methods are applied to different antenna systems and each investigator has selected a particular approach to the problem of near-field far-field transformation, the available methods of mathematical modelling and measurement techniques are often different. However, in all cases the antenna field is measured on a closed, or, open surface near the antenna. This measured field is then utilized to calculate the far-field radiation pattern of the antenna, by a most suitable transformation method, which normally depends on the measurement surface. Mathematically, the transformation of the near-field to the far-field is accurate only if the measurement of the near-field is carried out on a closed surface near the antenna. However, from a practical point of view, in certain occasions, accurate far-field data may also be obtained from the measurement of the near-field on an open surface, such as the aperture field of high gain antennas. In such cases, the measurement of the near-field on a closed surface around the antenna may become

too costly and the increased accuracy of the far-field data may not be too significant to justify the extra cost. Furthermore, an accurate measurement of the near-field beyond the antenna aperture may not be practically feasible, since the field strength in this region is normally too weak. The accurate measurement of the near-field gets more complicated at high frequencies, where the measurement coordinates become too close to each other. The latter requirement imposes increasingly difficult mechanical precision on the scanning system of the near-field measurement setup.

In the above near-field far-field transformation problems one, normally, measures the near-field of an isolated antenna system. In this thesis, we are concerned with field of an unknown antenna in the presence of a spherical or cylindrical scatterer. The problem therefore is to reconstruct the unknown near-field of a radiator from the measurement data of the total near-field in the vicinity of the antenna and the scatterer combination. The problem has practical significance, since, dielectric scatterers are occasionally used to shape the radiation patterns of the waveguides, horns and other radiating systems. Also, the introduction of the scatterer in the vicinity of a radiator can improve the intensity of the wide angle field distributions and facilitate the accurate measurement of the near-field.

To avoid large scanning systems, required for large antennas, a stepwise approach is selected, in which the near-field is measured over small spherical (or cylindrical) surfaces in the vicinity of the scatterer. The required information on the field and over a surface enclosing the antenna is then obtained by repeating the measurement at several locations around the antenna. This stepwise approach not only reduces the required scanning surface, but also reduces the expansion of antenna field over a large surface to several expansions over small surfaces. Note that when the dielectric constant of the scatterer becomes unity the problem reduces to the near-field measurement of an isolated antenna. In the following chapters, the details of the method are described and a mathematical formulation is presented. Several examples are also included and computed data are discussed.

Chapter two presents a summary of the important antenna measurement techniques together with a literature survey on the subject. In this chapter, three different methods for determination of the antenna characteristics are presented. These methods are the plane wave approach, the focusing method and the near-field probing technique.

Chapter two also presents a statement of the problem to

be discussed in this thesis. A method is proposed which can be used to determine the near-field from the measurement of the total field in the near-field zone and in the presence of a dielectric scatterer. A stepwise measurement approach over several small measurement surfaces, in lieu of a large measurement surface, is also presented.

Chapter three is devoted to the solution of two-dimensional inverse source problems. The problem therefore is to reconstruct the unknown near-field of a radiator from the measurement data of the total near-field in the vicinity of the antenna and a cylindrical scatterer. Although two-dimensional problems have less practical significance, nevertheless by discussing this class of problems some important aspects of the near-field far-field transformation are clarified.

The theoretical and numerical investigations of the three-dimensional inverse source problem are presented in chapters four and five, respectively. The technique for solving the three-dimensional problem is similar to the one used in the two-dimensional one. The scatterer in this case is a dielectric sphere. The description of the problem, the mathematical formulations and the method of solution are presented in chapter four. Since in this case a spherical

scatterer is utilized, then a spherical near-field far-field transformation is used to calculate the far-radiation pattern of the test antenna from the calculated near-field data. In chapter five numerical investigations are presented for three known sources. These sources are an incident plane wave, an electric dipole and an array of electric dipoles. The incident field in each case is reconstructed from the numerically generated total field on measurement spheres enclosing the scatterer. The main reason for selecting these sources is that, they are practical, simple and their exact incident field, which are used to generate the experimental data theoretically, are known. The stepwise measurement approach is utilized for the third example to calculate the far-radiation pattern of the isolated test antenna and the antenna in the presence of the spherical scatterer. This approach is used to calculate the near-field on a spherical surface which encloses the isolated antenna, or, the antenna and the scatterer combination.

The summary of the work, the discussion and conclusion of the results, and some suggestions for future research are presented in chapter six.

CHAPTER II

ANTENNA MEASUREMENT TECHNIQUES

2.1 INTRODUCTION

An antenna is a device for accomplishing a transition between a guided electromagnetic wave and a wave which propagates in free space. A knowledge of the antenna characteristics is important for finding a suitable antenna for a certain application. These characteristics include impedance, radiation patterns, gain, phase and polarization, ... etc.

The radiation characteristics of an antenna may be determined experimentally by two different techniques. The first technique is to make the measurements on the actual antenna on- or off- its site. The second one is to build an antenna model, smaller in size than the actual antenna. The measurements can then be done inside a laboratory on this model.

In the first technique, the antenna measurements can be done on-the site of the antenna or off-its site. The measurements of the radiation patterns of a full-scale antenna located on its ultimate site is a laborious and expensive task. Nevertheless, it is sometimes necessary to make such measurements.

This situation occurs when the antenna radiation is significantly affected by the site on which it is located, or when construction of the antenna is practical only at full scale on the site. On-site measurements of an antenna may have additional usefulness as a conclusive demonstration that the antenna is constructed properly, is correctly excited, and interacts with its environment in the predicted manner. When the antenna pattern is essentially independent of the environment, a simple measurement technique can be used off-site the antenna location. This consists of operating the antenna under test as a receiving antenna, rotating it, and measuring the signal it receives from a suitably-located fixed source antenna. The method may be used with success for most microwave antennas and can be applied at any frequency unless restricted by mechanical limitations. In the latter case, however, scale-model measurements may sometimes be suitable.

In the second technique, the actual antenna is simulated by a model. The measurements can be done on this model. The main characteristics of the actual antenna can then be calculated from those of its model [3]. There are two types of antenna models. One is a qualitative or geometrical model and the other is a quantitative or absolute model. In the qualitative models only the geometrical configurations of the

lines of force are modelled and no attempt is made to simulate the power levels of the full-scale system. These models yield data directly on these properties of the system which do not depend on power level such as impedance, polarization, antenna radiation patterns, relative patterns of radar echoes, etc. [3]. The quantitative models are capable of yielding quantitative data on all electromagnetic properties of the system. For example, measurements could be made for field intensity, radar echos, absolute radar echoing area, etc. [3].

This chapter will review the measurement techniques, which are carried out on actual antennas. Two recent textbooks [4] and [5] provide an excellent introduction to these measurement techniques. Three different methods will be discussed, the plane-wave, the focusing and the near-field probing methods. In the plane-wave method the test antenna is illuminated by a plane-wave and may include the far-field measurements, compact antenna ranges and the anechoic chambers. In the focusing method, the test antenna is focused within the radiating near-field for pattern measurements and then refocused to infinity for operation. In the last method, the near-field probing, the measurements are done in the near-field region and by using a suitable near-field far-field transformation, the antenna radiation characteristics are determined.

2.2 FIELD REGIONS

Reference [2] has explained in detail the nature of the field regions surrounding an antenna. In the region close to an antenna, the field will include both reactive as well as radiating components. The strength of the reactive component however, decays rapidly with distance from the antenna so that it soon becomes insignificant compared to the strength of the radiating component. The region in which the reactive component of the field predominates is called the reactive near-field region. The region beyond this is normally divided into the radiating near-field region and the radiating far-field region. Fig. 2.1 shows a pictorial representation of the three regions surrounding an antenna. The boundaries between the regions are not well defined, but for any antenna the reactive near-field region extends only to a short distance (about $\lambda/2\pi$ where λ is the wavelength). For electrically large antennas of the aperture type, the distance to the boundary between the radiating near-field and far-field regions is $R = 2D^2/\lambda$, where D is the largest dimension of the aperture.

2.3 PLANE WAVE TECHNIQUES

In these techniques, the antenna test ranges should be designed to produce a region of nearly "plane" electromagnetic waves within which a test antenna can be placed so that its

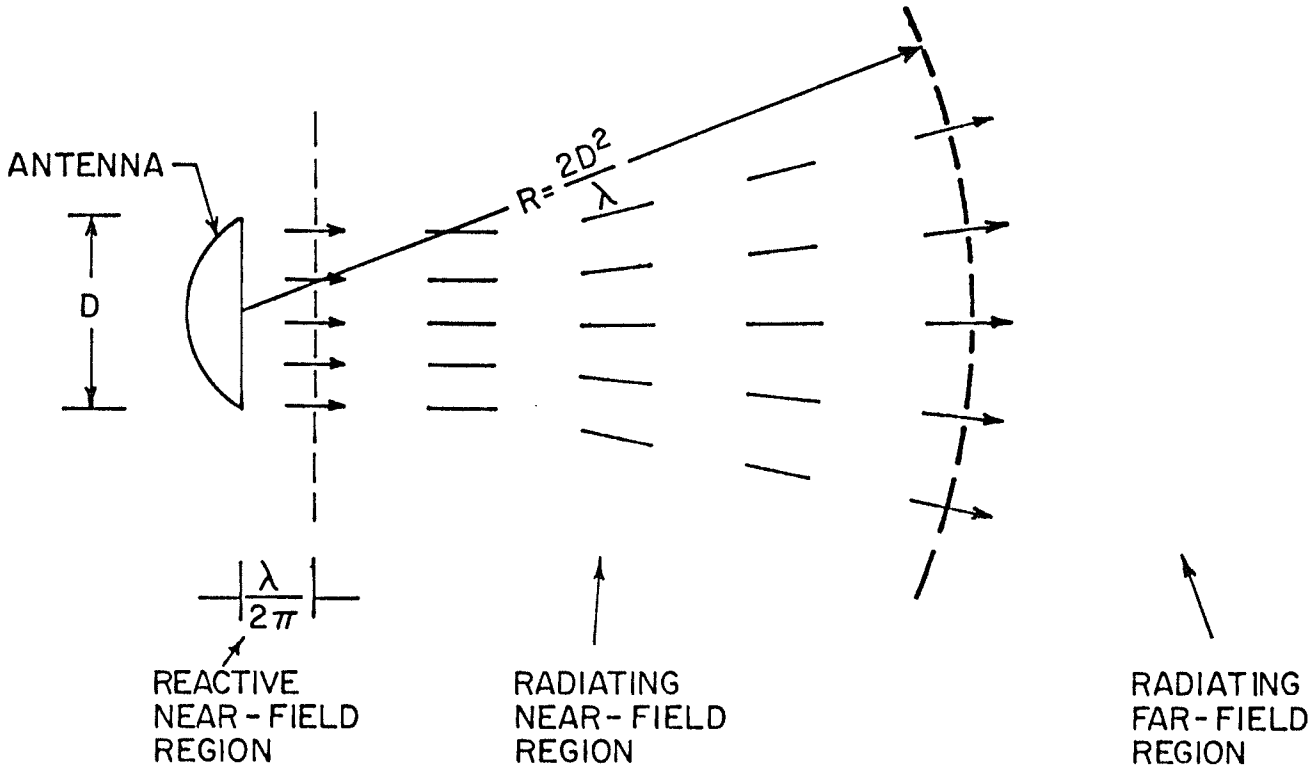

Fig. 2.1: Pictorial representation of the three regions surrounding an antenna (after Johnson et al. [2]).

radiation pattern can be measured and recorded. The resulting patterns may differ from the ideal far-field pattern, due to the fact that the wavefront in the test region may not have a completely constant amplitude and phase distributions. Antenna ranges which utilize a plane wave as a test source for measurements can be divided into three categories, they are:

a) Far-field ranges,

b) Anechoic chambers, and

c) Compact antenna ranges.

2.3.1 Far-Field Ranges

The far-field antenna radiation pattern requirements have been explained in detail in the literature [6], [7] and [8]. In its simplest form, a pattern range will contain a transmitting source, an antenna under test, a mount for turning the antenna under test, and a detector for indicating the relative magnitude of a received field. A set-up of this kind is shown in Fig. 2.2. The equipment used may be completely automatic, may require a point-by-point plot or a variation between these two. In any case, a number of important factors should be considered in order to be assured that the radiation patterns obtained are valid and accurate [6]. Some of these factors are:

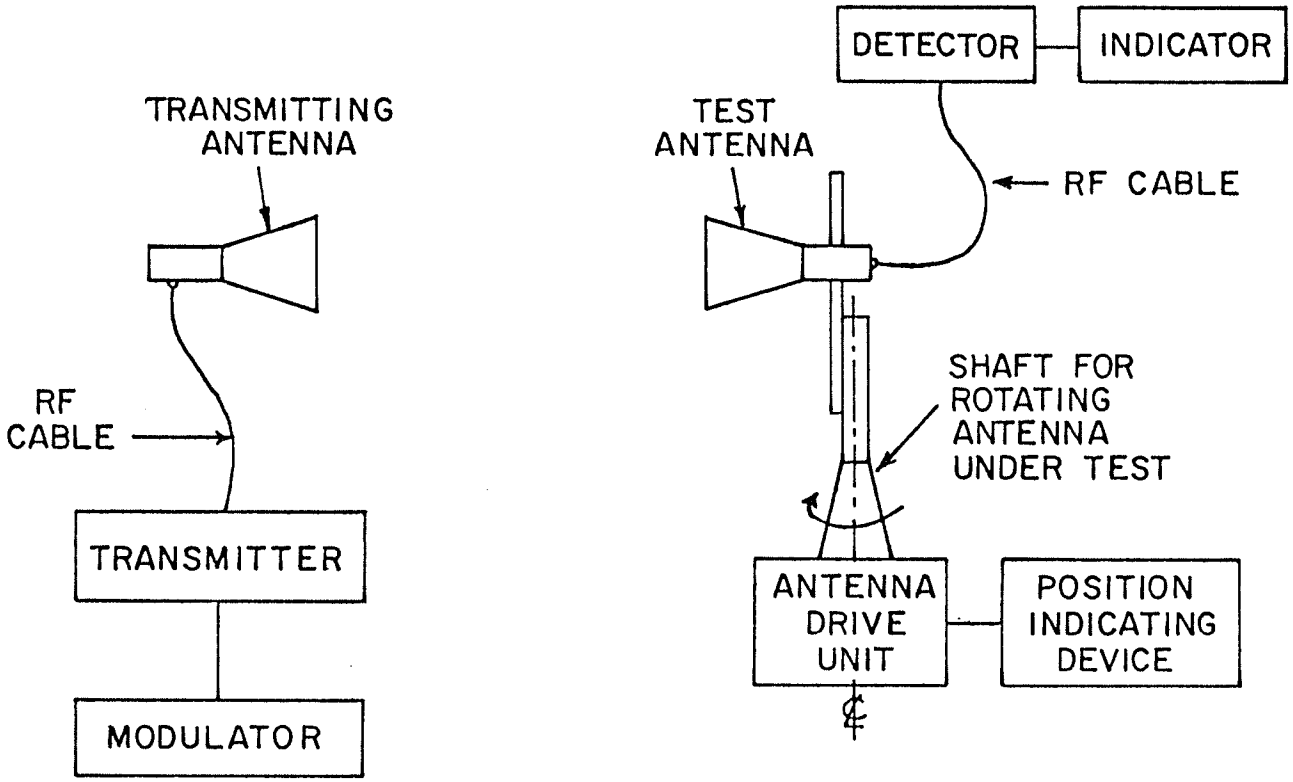

Fig. 2.2: Radiation-pattern measuring setup (after Jasik [6]).

a) Distance between test and transmitting antennas

In order to obtain accurate far-field radiation patterns, it is necessary that the distance between the transmitting antenna and the antenna under test be sufficiently large. For accurate far-field measurements, the antenna under test should be illuminated with a plane wavefront. Since plane wavefronts are obtainable only at infinite distances, some limits must be specified. A common specified criterion is that the phase difference between the center and the edge of the antenna under test should be no greater than $\lambda/16$ (22.5°). If this is the case, the distance R between the test and the transmitting antennas should at least be $R \geq 2D^2/\lambda$ [6], i.e., the test should be in the radiating far-field region.

b) Uniform illumination

A number of site conditions can contribute to a non-uniform field at the antenna under test. In all cases the site conditions result in a reflection of energy which causes cyclic or irregular variations in field intensity. Ground reflection can sometimes be avoided by mounting the antennas high above the ground on towers or making the transmitting antenna more directional in the vertical plane so as to reduce the amplitude of the reflection from the ground. Reference [6] has mentioned three other methods which have been used with some success in overcoming the ground-reflection difficulty.

The main parameters to be measured for an antenna in the far-field regions are: input and mutual impedances, radiation patterns, gain, phase front and polarization [6].

Some of the far-field ranges used are slant and reflection ranges. Slant ranges [7] and [9] are designed with the source antenna near the ground and the test antenna, along with its positioner, mounted on a nonconducting tower at a fixed height as shown in Fig. 2.3. The source antenna is located and oriented so that its free-space radiation pattern maximum points toward the center of the test region while the first null of the pattern points towards the specular reflection point on the ground. In this way, the reflected signal is suppressed. Slant ranges have been designed with towers whose height can be changed so that the spacing between the source and test antennas can be varied. The frequency range over which this range type has been tested and used extends from 100 MHz to 20 GHz [7]. The main advantages of the slant ranges are the ease of obtaining an essentially plane wave at the elevated point and the ease of source adjustment, should it be necessary. Its main disadvantage is the limited range that one may obtain with the available, preferably nonconductive towers. This is especially true if the more desirable large angles are used, but the technique should find wide application where the $2D^2/\lambda$ criterion is easily satisfied [7].

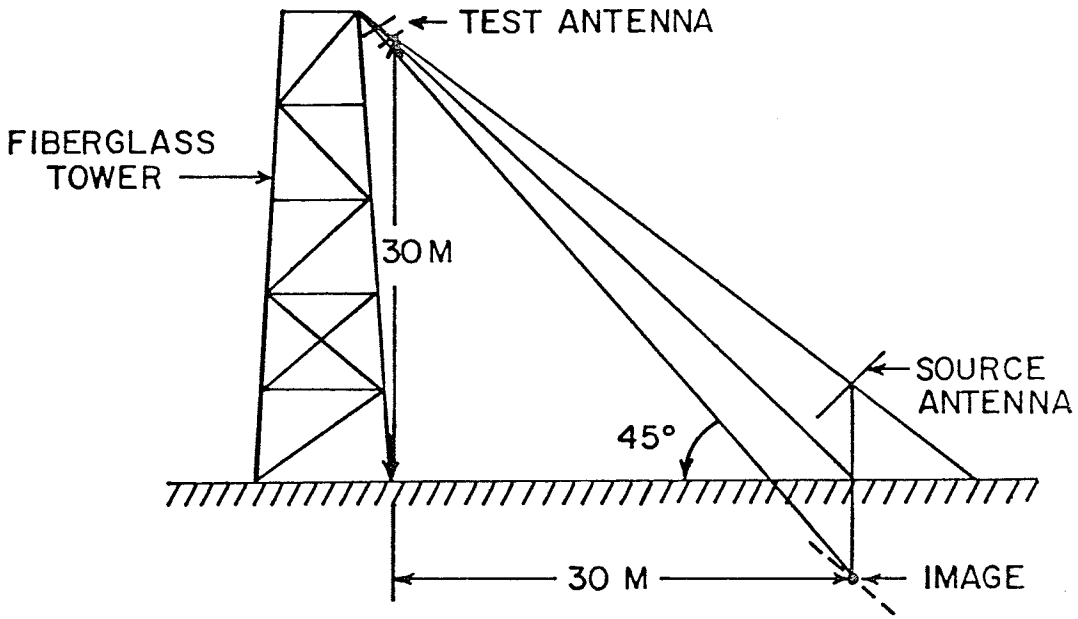

Fig. 2.3: Example of a "Slant" range geometry (after Arnold [7]).

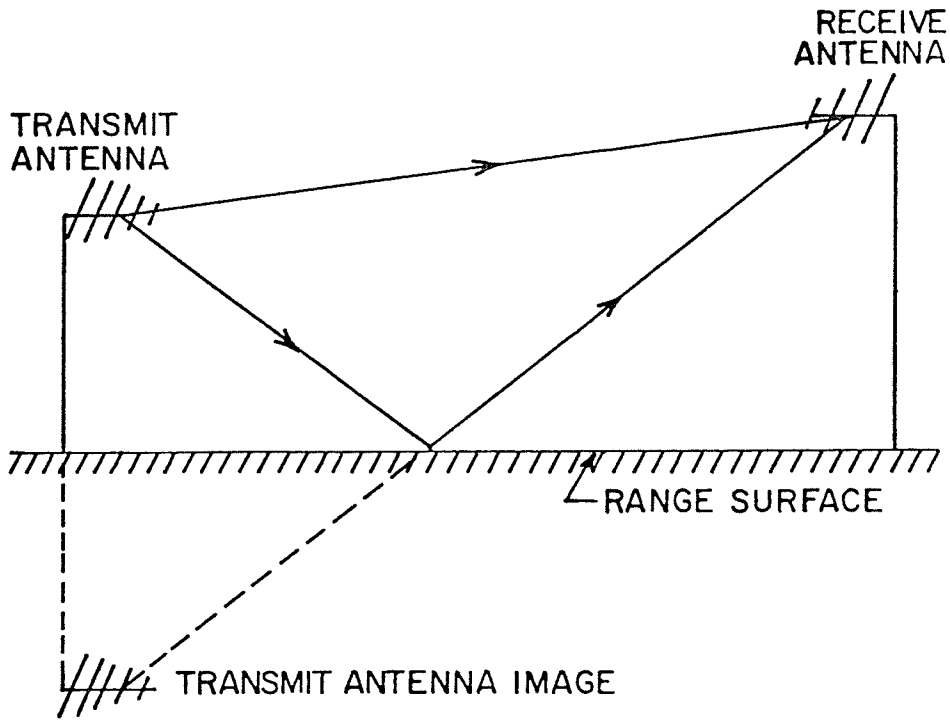

Fig. 2.4: Ground reflection range geometry (after Hemming and Heaton [8]).

The reflection ranges [8] and [9] are designed to make use of the energy which is specularly reflected from the surface of the range to create constructive interference with the energy from the direct path in the region of the test antenna. With proper design, the illuminating field will have small, essentially symmetric amplitude taper. This desired taper is obtained by an adjustment of the height of the source antenna above the range surface with the test antenna maintained at a fixed height. The ground is usually used as the reflecting surface; the reflection coefficient of the ground, as well as the smoothness, play an important part in the overall design [9]. These ranges find ready application in the UHF region for measuring antenna patterns which are moderately broad. Ranges operating from UHF through 16 GHz are being used [9]. Figure 2.4 shows a schematic diagram of one such range.

2.3.2 Anechoic Chambers

A historical summary of the development of microwave absorbing materials and anechoic chambers is presented in [10]. Anechoic chambers consist of two basic types [9]:

a) rectangular anechoic chambers, and

b) tapered anechoic chambers.

The existing chambers range from 175 ft. in length and up to

50 ft. by 50 ft. in cross-section [10]. Chambers may operate at frequencies as low as 30 MHz and higher than 100 GHz [10]. Some chambers have maximum reflection levels in the test range as low as -70 db below the direct path signal over certain frequency ranges, and some have shielding isolation to as low as -140 db [10].

Chambers have been designed as general purpose facilities and are employed for a wide variety of measurements; others have been designed for particular types of measurements such as antenna impedance, gain, bandwidth, cross-polarized component levels, antenna patterns, monostatic and bistatic radar cross-section patterns, system sensitivity, system susceptibility, system compatibility, effective radiated power, random error and tracking error [10].

Absorbers for chambers are available with a variety of characteristics of which the most important are the following: low normal incident reflection for chamber back wall; low forward scatter at wide angles for the specular regions of side walls, floor and ceiling of pattern measurement chambers; and low backscattering at wide angles for side walls, floor and ceiling [10]. A comparison between the antenna-pattern comparison and free-space VSWR techniques for evaluating the reflectivity level of radio anechoic chambers is presented in

[11]. Reference [9] has explained the rectangular anechoic chambers. The tapered one is also explained in detail in the literature [9] and [12].

2.3.3 Compact Antenna Ranges

The compact antenna range is an alternative to the more traditional far-field range (outdoor or anechoic room) or the new technique of near-field probing combined with numerical transformation to obtain the far-field antenna pattern.

Most aperture antennas are designed to transmit a beam over long distances; therefore, it is desirable to know certain features of the radiation pattern in the radiating far-field. Since the conventional procedure is to operate the test antenna in a receiving mode, it is desirable to illuminate the test antenna with a uniform plane wave. The creation of such a wave is a difficult task, however, one usually resorts to approximation methods.

One can locate the transmitting antenna in the far-field region to illuminate the test antenna for approximating a uniform plane wave. $R = 2D^2/\lambda$ is the minimum distance between the test antenna and the far-field region for aperture type of antennas. If the test antenna is very large and operating at

very high frequency (λ is very small and $D >> \lambda$), then R becomes very large. For this reason, serious problems can arise due to unwanted reflections from the ground and surrounding objects on an antenna range. In order to overcome these difficulties, a plane wave which is approximately uniform in amplitude and phase is created by a feed and large reflector in the immediate vicinity of the test antenna. This type is called compact antenna range.

The compact antenna range was first developed by Johnson et. al. [13]. Many references have discussed in detail this kind of antenna range and its uses [2], [9] and [13] to [16].

Fig. 2.5 shows the schematic representation of a compact range employing a reflector and a feed. The compact antenna range is used to take direct measurements of antenna patterns, gain, directivity, polarization and phase. It can also be used to measure radar cross-section [2] and [13]. In some situations a compact range can replace an outdoor range up to 200 meters long. The chief advantage of this range is its small size which allows it to be located indoors. The small size also reduces the requirements for microwave absorbing material [2] and [13]. It reduces the expenses by shortening the test time. Also a vast area of expensive real estate is not needed. It also allows to make and keep schedules which are not affected by weather or daylight, and

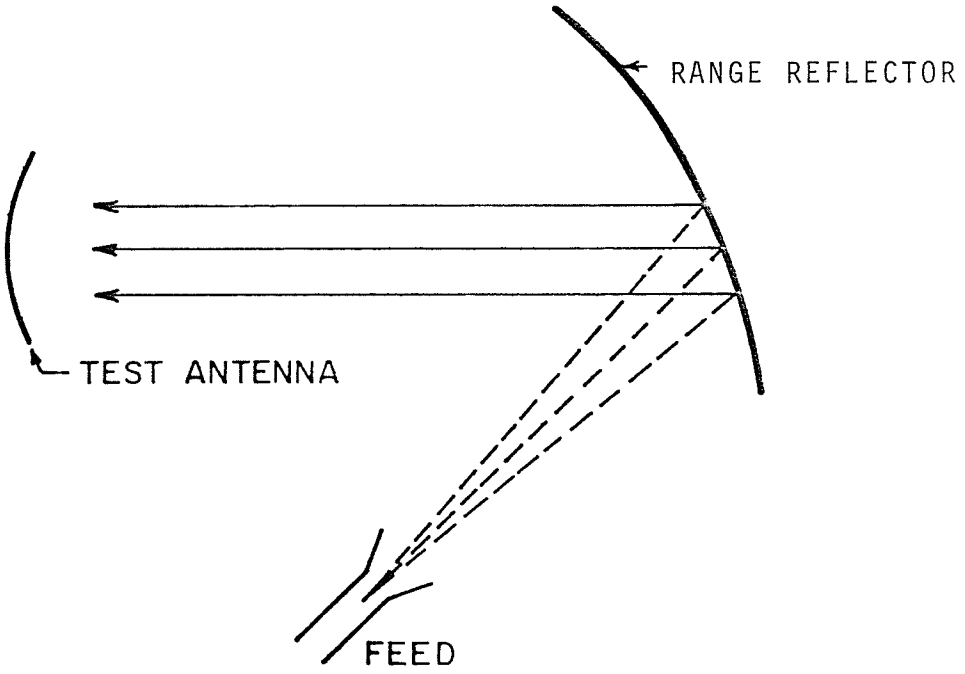

Fig. 2.5: Schematic representation of a compact range.

prevents unwanted surveillance. It works in a controlled, stable environment which produces uniform results [2], [9] and [13].

The chief limitation is that the range reflector must be larger than the antenna under test; in addition, the reflector must be constructed very accurately [2]. The useful frequency range of a compact range is limited on the upper end by fabrication errors of the range reflector and on the lower end by diffraction effects of the reflector edges and by direct radiation from the feed [2], [9], [13] and [16]. At lower frequencies, it is more difficult to use absorbing material to reduce direct radiation from the range feed to the test antenna [2]. A comparison of far-field ranges (outdoor and indoor anechoic-chamber) and compact antenna range is given in [15].

2.4 FOCUSING TECHNIQUE

Reference [2] has explained this technique in detail. The test antenna is focused within the radiating near-field for pattern measurements. It is applicable only to antennas which can be focused for testing and then refocused to infinity for operation.

The chief advantage of this technique is that pattern measurements can be made in the radiating near-field for many

antennas when available ranges are not long enough for far-field measurements. This technique usually is employed only when a far-field range of sufficient length is not available.

The technique of focusing at a short range is applied to paraboloids or lenses which can be focused by axial positioning of the feed, linear arrays which can be physically bent along a circular arc of radius equal to the test distance, and to electronically phased arrays whose element phasing can be altered to provide focusing at the test distance [2]. It is also applied to antennas with parabolic-cylinder reflectors and line-source feeds and to planar arrays which can be physically deformed to focus the array at the test distance [2]. If focusing of an extended aperture is accomplished in only one plane, patterns can be made only in the plane of focus, and the gain of the antenna will be reduced from the far-field gain because of the aperture phase error in the orthogonal plane [2].

2.5 THE NEAR-FIELD TECHNIQUE

This modern technique includes near-field probing (or scanning) and near-field far-field transformation.

The suitability of a given method of determining an antenna pattern of course depends upon the antenna and the use

of the data. For an antenna which is small both physically and in terms of wavelength, near field techniques seldom compete with conventional methods. However, for larger antennas, near-field techniques have the following distinct advantages [17].

Near-field measurement systems are closely coupled and therefore subject to laboratory-type control which yields high accuracy. The data are expressed as linear combinations of exact complex vector solutions of Maxwell's equations, with high signal-to-noise ratio, averaging over 10,000 or more measurements for each pattern value, full correction for proximity effects, and absence of ground and grazing angle reflections, as in an anechoic chamber. Further, it provides quite detailed pattern information, and it can yield phase and amplitude of each component of the electromagnetic six-vector for any distance. Not only it is independent of weather but it also permits measurements to be made in a clean room and in atmospheric absorption bands.

Near-field measurements are somewhat limited by the availability of absorbers, say below a few hundred megahertz for antennas. However, the antenna may be directed toward the zenith and ferrite absorbers used, consistent with their cost. Further, at very high frequencies, measurement of phase

as a function of position becomes more difficult, particularly measurement to a small fraction of a cycle over a large area, all referred to a single reference [17].

In many cases, it is impractical or impossible to measure antenna patterns on a conventional far-field range. This is due to the fact that for large antennas, the distance to the radiating far-field $R(=2D^2/\lambda)$ becomes very large. For this reason and due to the distinct advantages of the near-field scanning techniques as mentioned before, it is desirable or necessary to determine far-field antenna patterns from measurements made in the radiating near-field region. Therefore, near-field measurements have received considerable attention. Two different principles have been used in an attempt to determine far-field antenna patterns from measurements of the near-field of an antenna, they are:

2.5.1 The Integral Method

This method is based on the fact that the complete electromagnetic field at a point outside a closed surface enclosing all sources can be determined from an integral equation satisfied by the field vectors over the surface [18]. If this surface coincides with the antenna surface, then the fields can be obtained from the measurements of only the surface magnetic field [1] and [2]. For aperture antennas, the Huygens-

Fresnel principle [18] was utilized to form an equivalent source from the aperture field distributions. Reference [18] has shown that, the complete electric $\underline{E}$ and magnetic $\underline{H}$ fields within a given volume can be expressed in terms of the current densities of the sources within the volume and the values of the field itself over the boundaries of the volume. If the volume of interest is defined to contain no sources and to be bounded by a closed surface S and the sphere at infinity, the $\underline{E}$ and the $\underline{H}$ fields at a point P within the volume are given by [18]:

$$\underline{E}_p = \frac{1}{4\pi} \int_S [-j\omega\mu(\hat{n} \times \underline{H})\psi + (\hat{n} \times \underline{E}) \times \nabla\psi + (\hat{n} \cdot \underline{E}) \nabla\psi] \, da \quad (2.1)$$

$$\underline{H}_p = \frac{1}{4\pi} \int_S [j\omega\varepsilon(\hat{n} \times \underline{E})\psi + (\hat{n} \times \underline{H}) \times \nabla\psi + (\hat{n} \cdot \underline{H}) \nabla\psi] \, da \quad (2.2)$$

where $\hat{n}$ is the unit vector normal to the surface and a time variation exp ($j\omega t$) is assumed. The function ψ is the scalar Green's function,

$$\psi = \frac{e^{-jkr}}{r} \quad (2.3)$$

where k is the free space propagation constant and r is the distance from a point on the surface to a field point. Equations (2.1) and (2.2) require the tangential and the

normal components of the electromagnetic field over the surface S. Reference [19] has mentioned formulas similar to Equations (2.1) and (2.2) which require only the tangential components of the electromagnetic field on the surface S to be known.

If it is desirable to determine the electric and magnetic fields at a point P in terms of current or charge distribution on the surface of the antenna, then we can use Equations (2.1) to (2.3) and the boundary conditions (the closed surface S is assumed to be perfectly conducting) [18],

$$\begin{aligned} \hat{n} \times \underline{E} &= \underline{0} \\ \hat{n} \times \underline{H} &= \underline{K} \\ \hat{n} \cdot \underline{E} &= \frac{\rho_s}{\varepsilon} \\ \hat{n} \cdot \underline{H} &= 0 \end{aligned} \tag{2.4}$$

where $\underline{K}$ is the surface electric current density and ρ_s is the surface electric charge density. By using the continuity equation which relates the current and the charge densities, then one obtains [18]:

$$\underline{E}_p = \frac{j}{4\pi\omega\varepsilon} \int_S [(\nabla \cdot \underline{K})\nabla - k^2 \underline{K}] \frac{e^{-jkr}}{r} \, da \tag{2.5}$$

$$\underline{H}_p = \frac{1}{4\pi} \int_S [\underline{K} \times \nabla] \frac{e^{-jkr}}{r} da \ . \qquad (2.6)$$

Thus in summary, the method of determining field patterns from source distributions involves the application of Equations (2.1) and (2.2) for aperture distributions or Equations (2.5) and (2.6) for current distributions.

2.5.2 Modal Expansions

This method is based on expressing the total electromagnetic field in terms of a modal functions. The amplitudes and phases of these modes can be determined from measurements of the electromagnetic field over an appropriate surface in the near-field. In this case, the modes may be plane waves [20] to [24], cylindrical waves [20] to [22] and [24] to [27], axial waves [28], spherical waves [20], [21] and [29] to [38], or any other set of functions which form a basis for wave solutions to Maxwell's equations.

In this method, the pattern of the probe is transformed to obtain a modal expansion in terms of wave numbers. The basic theory of probe-compensated and scanning near-field measurements and their applications using plane and cylindrical wave expansions are explained in detail in [20], [24] and [39] and spherical wave expansions in [20], [30] and [31]. In

this thesis, the emphasis will be on the cylindrical (chapter three) and spherical (chapters four and five) wave (modal) expansions.

A general survey of the near-field measurements are available in the literature [1] and [2].

2.6 STATEMENT OF THE PROBLEM DISCUSSED IN THIS THESIS

In the near-field measurement techniques, the antenna field is measured on a closed, or, open surface near the antenna. The measured field is then utilized to calculate the far radiation field of the antenna, by a suitable transformation method, which normally depends on the measurement surface. Mathematically, the transformation of the near-field to the far-field is accurate only if the measurement of the near-field is carried out on a closed surface near the antenna. However, from a practical point of view, in certain occasions accurate far-field data may also be obtained from the measurement of the near-field on an open surface, such as the aperture field of high gain antennas. In such cases, the measurement of the near-field on a closed surface around the antenna may become too costly and the increased accuracy of the far-field data may not be too significant to justify the extra cost. Furthermore, an accurate measurement of the near-field beyond the antenna aperture may not be practically

feasible, since the field strength in this region is normally too weak. The accurate measurement of the near field is further complicated at high frequencies, where the measurement coordinates become too close to each other. The latter requirement imposes increasingly difficult mechanical precision on the scanning system of the near-field measurement setup.

In the near-field far-field transformation problems one, normally, measures the near-field of an isolated antenna system. In this work, the field of an unknown antenna in the presence of a dielectric scatterer, e.g., cylinder or sphere will be considered. The problem therefore is to reconstruct the unknown near-field of a radiator from the measurement data of the total near-field in the vicinity of the antenna and the scatterer combination. The problem has practical significance, since, spherical dielectrics are occasionally used to shape the radiation patterns of the waveguides, horns and other radiating systems. Also, the introduction of the scatterer in the vicinity of a radiator can improve the intensity of the wide angle field distributions and facilitate the accurate measurement of the near-field.

To avoid large scanning systems, required for large antennas, a stepwise approach is selected, in which the near-field is measured over a small surface in the vicinity of the

scatterer. The required information on the field and over a surface enclosing the antenna is then obtained by repeating the measurement at several locations around the antenna. This stepwise approach not only reduces the required scanning surface, but also reduces the expansion of antenna field over a large surface to several expansions over small surfaces. Note that when the dielectric constant of the scatterer becomes unity, the problem reduces to the near-field measurement of an isolated antenna.

2.6.1 Method of Measurements

In this section, the suggested method of measurements to evaluate a test antenna in presence of a spherical scatterer is discribed. Fig. 2.6 shows the geometry of the problem. A scattering sphere is located in the vicinity of an antenna with unknown radiation characteristics. When the spherical surface S enclosing both scatterer and the antenna is small in size, the measurement can be carried out over this sphere to obtain the total field. In addition, the field outside S can be described by spherical wave functions with unknown coefficients. These unknown coefficients can then be obtained by matching the measured and the spherical wave expansion fields over the spherical surface S.

On the other hand, when the antenna, or its separation distance from the scattering sphere is large, the spherical

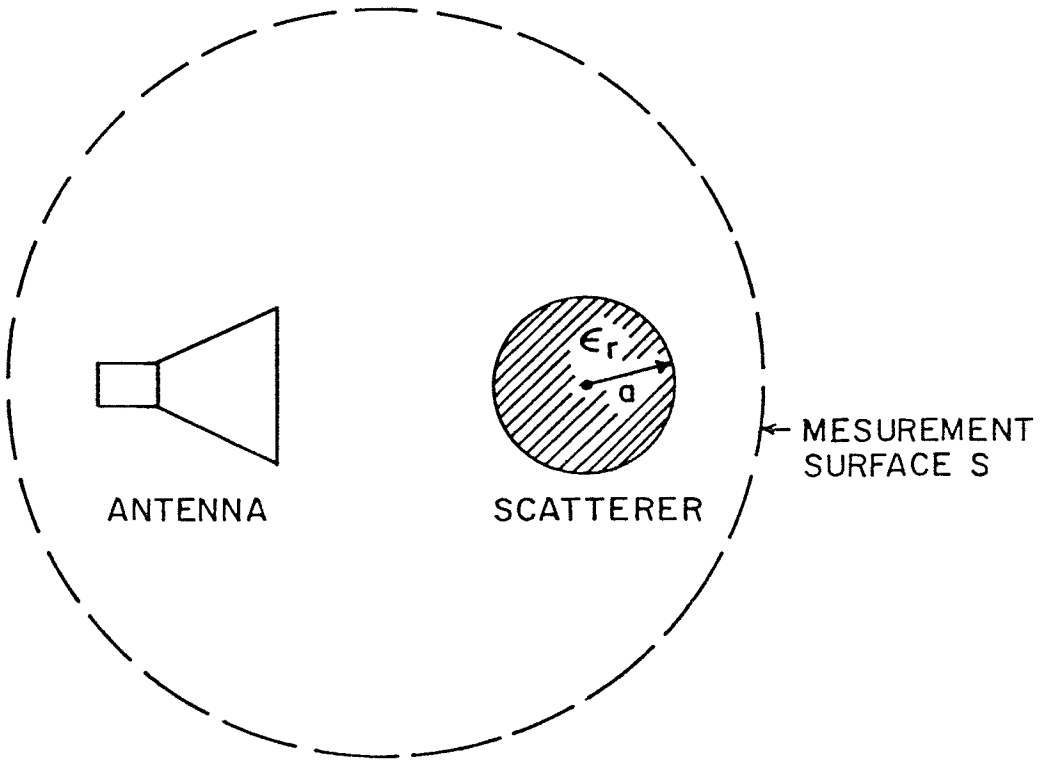

Fig. 2.6: Schematic diagram showing the antenna, scatterer and the scanning surface S.

surface enclosing them becomes large. The measurement of the field over such a large surface requires large scanning systems, which in practice is undesirable. To utilize a small scanning system, we propose to use the measurement steps of Fig. 2.7. In this system, the measurements are carried out over smaller surfaces defined as S_1, S_2, S_3, ... These results are then used to compute the field over the surface S, which encloses the antenna and the scatterer. The required field outside S can therefore be obtained using the above mentioned spherical wave expansion approach.

To obtain the field over the surface S we use the following steps:

1. Within the expansion sphere S_1' which includes both the scatterer and the measurement sphere S_1, the fields inside the scattering sphere and between its surface and S_1' are described by spherical wave functions with unknown coefficients. These unknown coefficients are obtained by matching the calculated and the measured fields over S_1.

2. Within S_2', S_3', ... the fields are described by spherical wave functions about the origin of each surface and their unknown coefficients are found after the matching of their respective fields. Following these steps the total fields are known within the expansion spheres S_1', S_2', ..., and can be

used to calculate the required field components over the surface S. Note that, the expressions for the field inside S_2', S_3' ... can be obtained from the expressions of the field inside S_1' by replacing its dielectric constant with unity. The problem therefore reduces to the evaluation of the unknown field coefficients for field inside S_1' and calculation of the required field components over S which falls within S_1'.

Note that, the above method can also be used to study the radiation characteristics of two-dimensional field sources. Although, such sources have limited practical significance, their investigation can provide useful information for understanding of the proposed measurement methods. In the next chapter the method is used to study the problem related to the convergence of the modal expansions, dependence of the results on the accuracy of the measurement data and importance of other pertinent parameters. A two-dimensional problem is selected to study these parametric effects, due to the fact that, it is simpler, requires less computation time and its results can directly be extended to more general three-dimensional cases discussed in the following chapters.

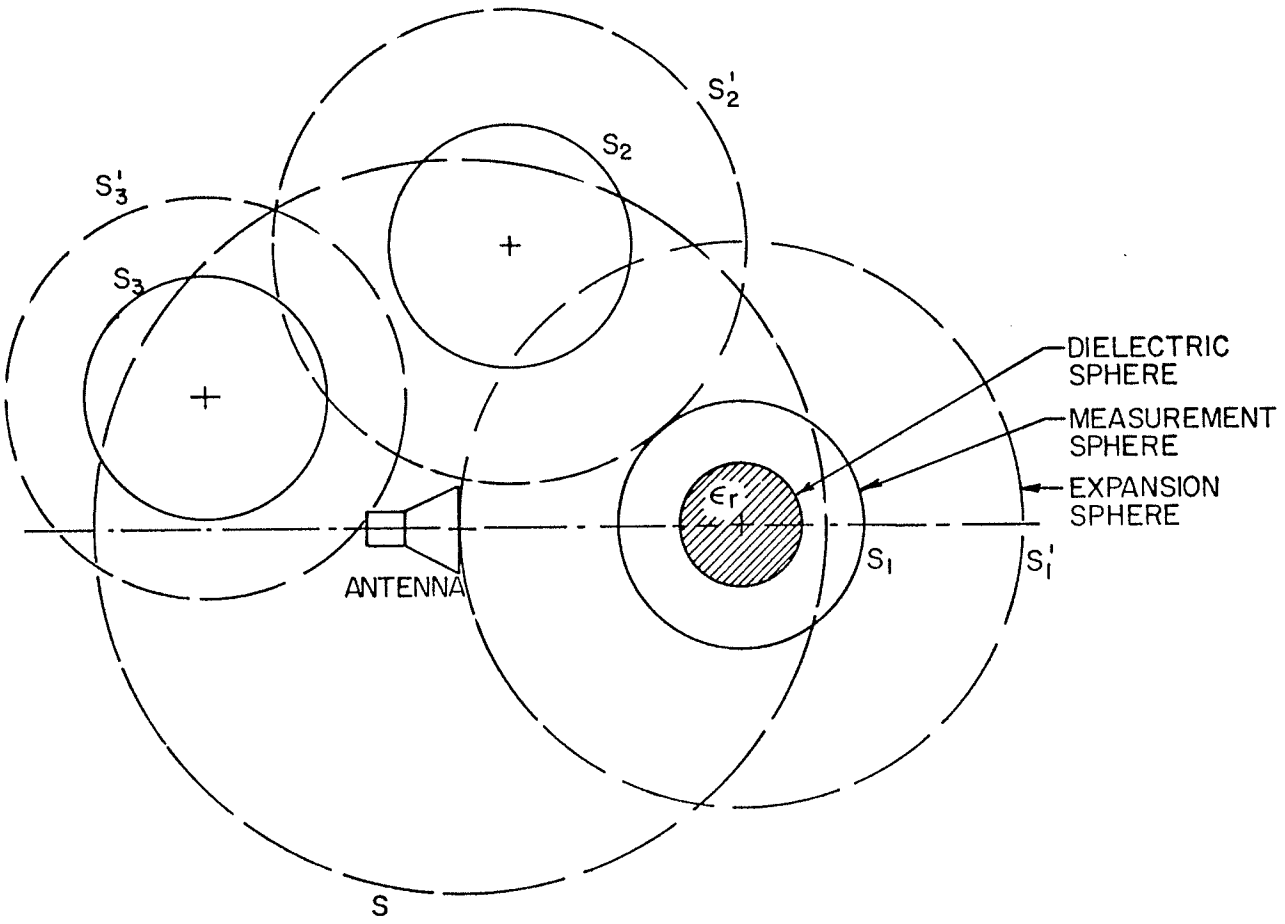

Fig. 2.7: Schematic diagram showing the antenna, scatterer, measurement spheres S_1, S_2, S_3, ..., expansion spheres S_1', S_2', S_3', ..., and the spherical surface S which encloses the antenna and the scatterer.

CHAPTER III

TWO-DIMENSIONAL INVERSE SOURCE PROBLEM

3.1 INTRODUCTION

In this chapter, the two-dimensional field of an unknown antenna in presence of a dielectric cylindrical scatterer will be considered. The problem therefore is to reconstruct the unknown near-field of a radiator from the measured data of the total near-field in the vicinity of the antenna and the scatterer combination. A two-dimensional problem is defined by assuming that, the electromagnetic fields and the cross-sectional geometry of the scatterer are independent of one of the coordinates. The two-dimensional problem has less practical importance than the three-dimensional one. Nevertheless, its investigation will provide useful information and may be a basis for the three-dimensional one. This has also some applications, for example, in calculating the radiation pattern of a long line source or an array of line sources in the vicinity of long dielectric cylinder. In this chapter, the theoretical analysis of this problem is presented together with the numerical results for a plane-wave source. Three practical problems are investigated numerically. The first one examines the convergence of the cylindrical wave functions in the expansion of the electromagnetic field for a certain scatterer size, while the

second one investigates the restriction on the size of the measurement cylinder. The last problem studies the effect of the measurement accuracy on the generated data, which is simulated here by adding certain noise levels to the amplitude and the phase of the measurement data. The measurement data are generated numerically using the well known solution of the plane wave scattering from a dielectric cylinder.

Fig. 3.1 shows the geometry of the problem. It shows a cylindrical scatterer in the vicinity of an antenna and the cylindrical coordinate system ρ, ϕ and z. The axis of the dielectric cylinder lies on the z-axis and the radius of its cross-section is a. The field in this problem is assumed to be independent of the z-coordinate.

Since the dielectric scatterer is placed in the incident electromagnetic field $\underline{E}^i$ and $\underline{H}^i$ of the test antenna, a scattered field will be generated due to the scattering of the incident field by the scatterer. By measuring the total electromagnetic field on certain cylindrical measurement surface of radius $\rho = A > a$ outside the scatterer, one can recover the incident field of the test antenna. The total electromagnetic field outside the scatterer is the sum of both the incident and the scattered fields in the same region.

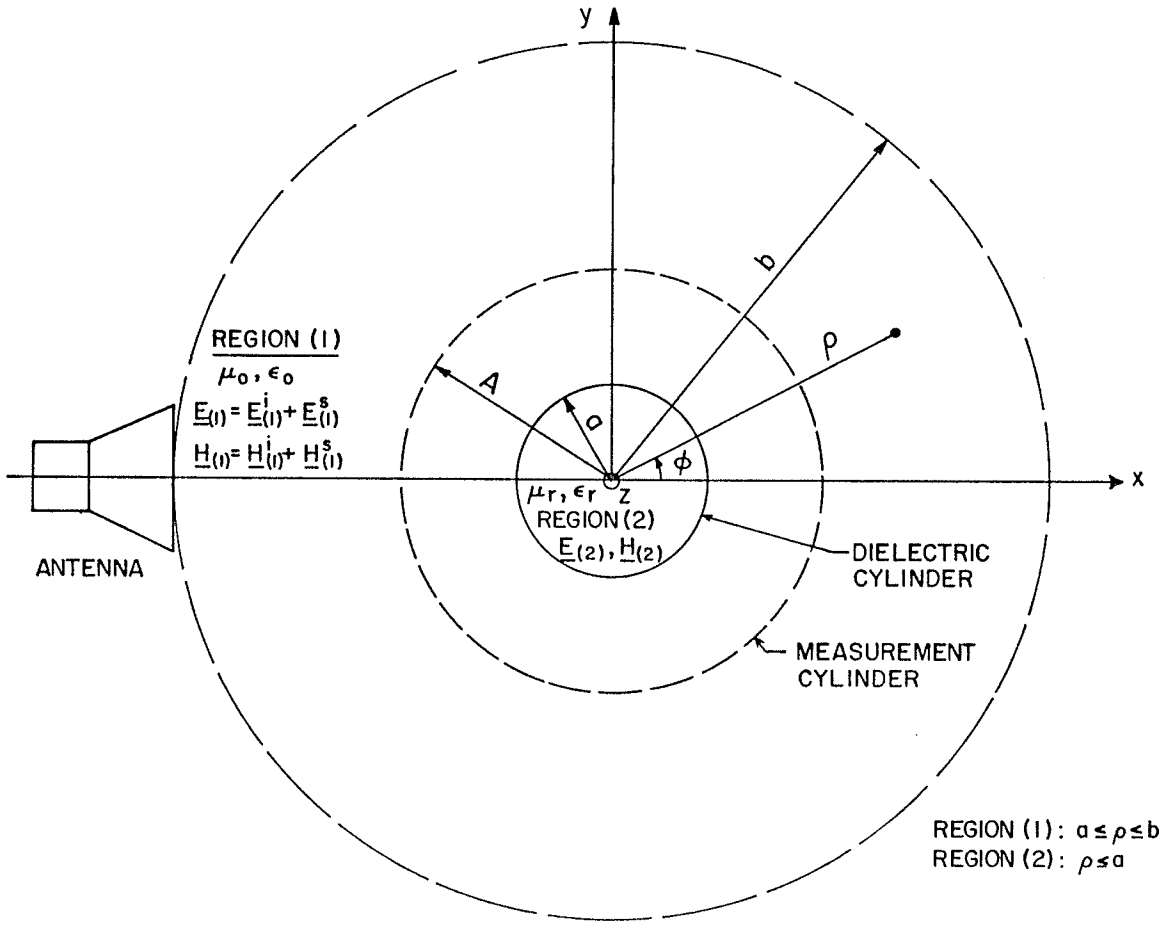

Fig. 3.1: The cross-section of the cylindrical coordinate system, antenna, dielectric scatterer and the measurement cylinder.

To formulate the problem, let the region outside the dielectric cylinder and between the test antenna and the scatterer be called region (1) ($\rho \geq a$). Also, let the region inside the dielectric cylinder be called region (2) ($\rho \leq a$). Both regions are considered here to be source free, linear, homogeneous and isotropic. In region (1), the total electromagnetic fields are given by: (the time dependence exp ($j\omega t$) is implicitly assumed in the analysis of this chapter)

$$\underline{E}_{(1)} = \underline{E}^{i}_{(1)} + \underline{E}^{s}_{(1)} \tag{3.1}$$

and

$$\underline{H}_{(1)} = \underline{H}^{i}_{(1)} + \underline{H}^{s}_{(1)} \quad . \tag{3.2}$$

Since $\underline{E}^{s}_{(1)}$ and $\underline{H}^{s}_{(1)}$ are functions of the unknown incident fields $\underline{E}^{i}_{(1)}$ and $\underline{H}^{i}_{(1)}$, then from Equations (3.1) and (3.2) the total electromagnetic fields in region (1), $\underline{E}_{(1)}$ and $\underline{H}_{(1)}$, are functions of the incident field $\underline{E}^{i}_{(1)}$ and $\underline{H}^{i}_{(1)}$. From these relationships, if the total fields are known on a certain surface, i.e., the measurement cylinder with radius $\rho = A > a$, then the incident field of the test antenna in region (1) may be determined. The incident and the scattered electromagnetic fields in region (1) can be expanded in terms of the appropriate cylindrical wave functions weighted by their unknown coefficients. Also the total electromagnetic fields

in region (2) can be expanded using the appropriate cylindrical wave functions with unknown coefficients. The boundary conditions require the continuity of the tangential components of the electromagnetic fields on the boundary of the dielectric cylinder $\rho = a$. These boundary conditions give a relationship between the unknown coefficients of the scattered field in region (1) and the total field in region (2) in terms of the unknown coefficients of the incident field in region (1). By measuring the total field on the surface of the measurement cylinder in region (1), one can therefore calculate the unknown coefficients of the incident field, from which the incident field of the test antenna in region (1) can be determined.

3.2 MATHEMATICAL FORMULATION OF THE SCATTERING PROBLEM

3.2.1 Expansion of the Electromagnetic Fields Using the the Cylindrical Wave Functions

It is well known that any electromagnetic field in regions which are source free, linear, homogeneous and isotropic can be expanded in terms of the cylindrical wave functions [21] and [37] which forms a basis for the wave solution of Maxwell's equations. In the two-dimensional problem, where the electromagnetic field is independent of one of the coordinates, the elementary cylindrical wave functions ψ_n can be written as:

$$\psi_n(\rho, \phi) = Z_n^{(i)}(k\rho)\, e^{jn\phi} \tag{3.3}$$

where ρ and ϕ are the radial and the azimuthal coordinates in the conventional cylindrical coordinate system as shown in Fig. 3.1. Also, $Z_n^{(i)}$ is a radial function representing one of the following J_n, Y_n, $H_n^{(1)}$ or $H_n^{(2)}$ cylindrical Bessel functions for (i) = (1), (2), (3) or (4), respectively, and k is the propagation constant $(2\pi/\lambda)$. The choice of the appropriate radial function $Z_n^{(i)}$ depends upon the nature of the electromagnetic field in a given region and will be discussed later.

In general, the electromagnetic field may be expressed as [29], [37] and [40]

$$\underline{E}(\rho,\phi) = \frac{\mu\omega}{\rho} \sum_{n=-\infty}^{\infty} n d_n \psi_n \hat{i}_\rho + j\mu\omega \sum_{n=-\infty}^{\infty} d_n \frac{\partial \psi_n}{\partial \rho} \hat{i}_\phi$$

$$+ k^2 \sum_{n=-\infty}^{\infty} e_n \psi_n \hat{i}_z \tag{3.4}$$

and

$$\underline{H}(\rho,\phi) = -\frac{k^2}{\mu\omega} \frac{1}{\rho} \sum_{n=-\infty}^{\infty} n e_n \psi_n \hat{i}_\rho - \frac{jk^2}{\mu\omega} \sum_{n=-\infty}^{\infty} e_n \frac{\partial \psi_n}{\partial \rho} \hat{i}_\phi$$

$$+ k^2 \sum_{n=-\infty}^{\infty} d_n \psi_n \hat{i}_z \tag{3.5}$$

where d_n and e_n are constants, ψ_n is given by Equation (3.3) and $\hat{i}_\rho$, $\hat{i}_\phi$ and $\hat{i}_z$ are the unit vectors in ρ,ϕ and z directions, respectively.

In Equations (3.4) and (3.5) if $d_n = 0$ for all values of n, then the field is transverse magnetic (TM) to the z-direction. Also, if $e_n = 0$ for all values of n, then the field is transverse electric (TE) to the z-direction. In the analysis of this chapter, only TM case is considered. However a similar study can readily be carried out for the TE case. A linear combination of both TE and TM cases represents a general electromagnetic field problem, which should be considered for an unknown source problem.

Considering only the TM case, in region (1) as shown in Fig. 3.1 ($\rho \geq a$), the incident and the scattered electromagnetic fields can be written in terms of the cylindrical wave functions by putting $d_n = 0$ and $k^2 e_n = a_n$ in Equations (3.4) and (3.5). One therefore obtains,

$$\underline{E}^i_{(1)} = \sum_{n=-\infty}^{\infty} a_n J_n(k_o\rho)\, e^{jn\phi}\, \hat{i}_z \qquad (3.6)$$

and

$$\underline{H}^i_{(1)} = -\frac{1}{\mu_o\omega}\frac{1}{\rho}\sum_{n=-\infty}^{\infty} n a_n J_n(k_o\rho)\, e^{jn\phi}\, \hat{i}_\rho - \frac{jk_o}{\mu_o\omega}\sum_{n=-\infty}^{\infty} a_n J_n'(k_o\rho)\, e^{jn\phi}\, \hat{i}_\phi \ . \qquad (3.7)$$

The expansion of the scattered field in the same region (1) yields:

$$\underline{E}^{s}_{(1)} = \sum_{n=-\infty}^{\infty} b_n H_n^{(2)} (k_o \rho)\, e^{jn\phi}\, \hat{i}_z \tag{3.8}$$

and

$$\underline{H}^{s}_{(1)} = -\frac{1}{\mu_o \omega}\frac{1}{\rho} \sum_{n=-\infty}^{\infty} n b_n H_n^{(2)} (k_o \rho)\, e^{jn\phi}\, \hat{i}_\rho$$

$$-\frac{jk_o}{\mu_o \omega} \sum_{n=-\infty}^{\infty} b_n H_n^{(2)'} (k_o \rho)\, e^{jn\phi}\, \hat{i}_\phi \tag{3.9}$$

where a_n and b_n are the incident and the scattered fields expansion coefficients, respectively. k_o is the propagation constant in the free space. In Equations (3.6) and (3.7) the radial function of the incident field is chosen to be the Bessel function of the first kind, J_n, which is finite at the origin $\rho = 0$. Also, in Equations (3.8) and (3.9), the radial function of the scattered field is chosen to be the Hankel function of the second kind $H_n^{(2)}$ to satisfy the radiation condition at infinity. J_n' and $H_n^{(2)'}$ in Equations (3.7) and (3.9) are the derivatives of J_n and $H_n^{(2)}$ with respect to their arguments, respectively. Substituting Equations (3.6) to (3.9) into Equations (3.1) and (3.2), the total electromagnetic field in region (1) can be written in the form:

$$\underline{E}_{(1)} = \underline{E}^{i}_{(1)} + \underline{E}^{s}_{(1)}$$

$$= \sum_{n=-\infty}^{\infty} [a_n J_n(k_o\rho) + b_n H_n^{(2)}(k_o\rho)] e^{jn\phi}\, \hat{i}_z \qquad (3.10)$$

and

$$\underline{H}_{(1)} = \underline{H}^{i}_{(1)} + \underline{H}^{s}_{(1)}$$

$$= -\frac{1}{\mu_o \omega}\frac{1}{\rho} \sum_{n=-\infty}^{\infty} n[a_n J_n(k_o\rho) + b_n H_n^{(2)}(k_o\rho)]\, e^{jn\phi}\, \hat{i}_\rho$$

$$-\frac{jk_o}{\mu_o \omega} \sum_{n=-\infty}^{\infty} [a_n J_n'(k_o\rho) + b_n H_n^{(2)'}(k_o\rho)]\, e^{jn\phi}\, \hat{i}_\phi \,. \qquad (3.11)$$

Denoting the total electromagnetic field in region (2), $\rho \leq a$, as $\underline{E}_{(2)}$ and $\underline{H}_{(2)}$, they can similarly be written in the form:

$$\underline{E}_{(2)} = \sum_{n=-\infty}^{\infty} c_n J_n(k_d\rho)\, e^{jn\phi}\, \hat{i}_z \qquad (3.12)$$

and

$$\underline{H}_{(2)} = -\frac{1}{\mu_d \omega}\frac{1}{\rho} \sum_{n=-\infty}^{\infty} n c_n J_n(k_d\rho)\, e^{jn\phi}\, \hat{i}_\rho$$

$$-\frac{jk_d}{\mu_d \omega} \sum_{n=-\infty}^{\infty} c_n J_n'(k_d\rho)\, e^{jn\phi}\, \hat{i}_\phi \qquad (3.13)$$

where c_n is the weighting coefficient of the total electromagnetic field. Also, in region (2), $k = k_d = \omega\sqrt{\mu_d \varepsilon_d} = \frac{2\pi}{\lambda_d}$, λ_d is the wavelength in this region and μ_d and ε_d are the permeability and permittivity of the dielectric scatterer material, respectively.

The boundary conditions of this problem which assures the continuity of the tangential components of the electromagnetic fields across the boundary of the infinite dielectric cylinder ($\rho = a$) are given by:

$$\left.\begin{aligned} \hat{n} \times \underline{E}_{(1)} &= \hat{n} \times \underline{E}_{(2)} \\ \text{and} \\ \hat{n} \times \underline{H}_{(1)} &= \hat{n} \times \underline{H}_{(2)} \end{aligned}\right\} \quad \text{at } \rho = a \qquad (3.14)$$

where $\hat{n}$ is the unit vector normal to the boundary $\rho = a$ and directed outside the scatterer. Equation (3.14) can be written in the form:

$$E_{z_{(1)}}(a, \phi) = E_{z_{(2)}}(a, \phi)$$

and

$$H_{\phi_{(1)}}(a, \phi) = H_{\phi_{(2)}}(a, \phi) \quad . \qquad (3.15)$$

A substitution of Equations (3.10) to (3.13) into Equation (3.15) and using the orthogonality relationship of the exponential function gives relationship between the scattered field coefficients b_n in region (1) and the total field coefficients c_n in region (2) in terms of the incident field coefficients a_n in region (1). This can be written in the form:

$$\left.\begin{aligned} b_n &= B_n\, a_n \\ \text{and} \qquad c_n &= C_n\, a_n \end{aligned}\right\} \tag{3.16}$$

where:

$$B_n = \frac{\sqrt{\frac{\varepsilon_r}{\mu_r}}\; J_n(k_o a)\; J_n'(k_d a) - J_n'(k_o a)\; J_n(k_d a)}{-\sqrt{\frac{\varepsilon_r}{\mu_r}}\; H_n^{(2)}(k_o a)\; J_n'(k_d a) + H_n^{(2)'}(k_o a)\, J_n(k_d a)} \tag{3.17}$$

and

$$C_n = \frac{-\frac{2j}{\pi k_o a}}{-\sqrt{\frac{\varepsilon_r}{\mu_r}}\, H_n^{(2)}(k_o a)\; J_n'(k_d a) + H_n^{(2)'}(k_o a)\; J_n(k_d a)} \quad . \tag{3.18}$$

Thus from Equations (3.16), (3.10) and (3.11), the total electromagnetic field in region (1) can be written in terms

of the cylindrical wave expansion weighted by the unknown incident field coefficients a_n by the following expressions:

$$\underline{E}_{(1)}(\rho,\phi) = \sum_{n=-\infty}^{\infty} a_n[J_n(k_o\rho) + B_n H_n^{(2)}(k_o\rho)]\, e^{jn\phi}\, \hat{i}_z \qquad (3.19)$$

and

$$\underline{H}_{(1)}(\rho,\phi) = -\frac{1}{\mu_o\omega}\frac{1}{\rho} \sum_{n=-\infty}^{\infty} n a_n [J_n(k_o\rho) + B_n H_n^{(2)}(k_o\rho)]\, e^{jn\phi}\, \hat{i}_\rho$$

$$-\frac{jk_o}{\mu_o\omega} \sum_{n=-\infty}^{\infty} a_n [J_n'(k_o\rho) + B_n H_n^{(2)'}(k_o\rho)]\, e^{jn\phi}\, \hat{i}_\phi \quad . \qquad (3.20)$$

3.2.2 Determination of the Unknown Coefficients a_n of the Incident Field

To determine the incident electromagnetic field of the test antenna in region (1), the unknown coefficients a_n must be determined. These coefficients can be determined by matching the tangential components of the total fields over a measurement cylinder using one of the following methods:

3.2.2.1 The integration method

The coefficients a_n can be derived from Equations (3.19) and (3.20) by using the orthogonality relation in the ϕ-coordinate. The results are:

$$a_n = \frac{1}{J_n(k_o A) + B_n H_n^{(2)}(k_o A)} \frac{1}{2\pi} \int_0^{2\pi} E_{z(1)}(A,\phi)\, e^{-jn\phi}\, d\phi \qquad (3.21)$$

or

$$a_n = \frac{j\eta}{J_n'(k_o A) + B_n H_n^{(2)'}(k_o A)} \frac{1}{2\pi} \int_0^{2\pi} H_{\phi(1)}(A,\phi)\, e^{-jn\phi}\, d\phi \qquad (3.22)$$

where η is the free space interinsic impedance, $E_{z(1)}$ and $H_{\phi(1)}$ are the tangential components of the total electric and magnetic fields in region (1), on the surface of the measurement cylinder $\rho = A$. In these equations the integrals can be evaluated numerically by using the measurement data of E_z, or H_ϕ over a measurement cylinder. The results when used in the above equations give the required expansion coefficients.

3.2.2.2 The matrix method

The coefficients a_n of the incident field can also be evaluated by using matrix method. This method requires the truncation of the infinite series in Equations (3.19) or (3.20) to a finite number of terms. If these series are truncated to K terms, from n=-(N-1) to n=(N-1), then the number of unknowns will be K=2N-1. These K unknowns can be determined by matching the expansion fields with the measure-

ment ones at K points in space to set up a matrix equation. In the present work, all matching points are assumed to be on the surface of a cylinder. A solution of these linear algebraic equations with K-unknowns gives the unknown coefficients a_n. Once these coefficients are known, the field of the antenna can be calculated anywhere in space. If the measurements are done at K(=2N-1) azimuthal angles $\phi=\phi_o$, ϕ_1, ... and ϕ_{2N-2}, the resulting system of linear algebraic equations can be written in the form:

$$S\ \underline{\alpha} = \underline{\beta} \tag{3.23}$$

where S is a KxK matrix. From Equations (3.19) and (3.20) the matrix S is given by:

$$S = \begin{pmatrix} e^{-j(N-1)\phi_o} & e^{-j(N-2)\phi_o} & \cdots & e^{-j\phi_o} & 1 & e^{j\phi_o} & \cdots & e^{j(N-2)\phi_o} & e^{j(N-1)\phi_o} \\ e^{-j(N-1)\phi_1} & e^{-j(N-2)\phi_1} & \cdots & e^{-j\phi_1} & 1 & e^{j\phi_1} & \cdots & e^{j(N-2)\phi_1} & e^{j(N-1)\phi_1} \\ \vdots & & & & & & & & \vdots \\ e^{-j(N-1)\phi_{2N-2}} & e^{-j(N-2)\phi_{2N-2}} & \cdots & e^{-j\phi_{2N-2}} & 1 & e^{j\phi_{2N-2}} & \cdots & e^{j(N-2)\phi_{2N-2}} & e^{j(N-1)\phi_{2N-2}} \end{pmatrix} \tag{3.24}$$

The vector $\underline{\alpha}$ contains the K-unknown coefficients of the incident field and its transpose is:

$$\underline{\alpha}^T = [\alpha_{-(N-1)} \alpha_{-(N-2)} \cdots \alpha_{-1} \alpha_0 \alpha_1 \cdots \alpha_{N-2} \alpha_{N-1}] \quad . \quad (3.25)$$

The right hand side of Equation (3.23) is the K element measurement vector $\underline{\beta}$ which can be determined by measuring the tangential components of the total electric (or magnetic) field on the surface of the measurement cylinder. The transpose of this vector $\underline{\beta}$ is given by:

$$\underline{\beta}^T = [E_{z_{(1)}}(A, \phi_0) \quad E_{z_{(1)}}(A, \phi_1) \cdots E_{z_{(1)}}(A, \phi_{2N-2})] \quad (3.26)$$

when the tangential components of the total electric field are known. Or:

$$\underline{\beta}^T = [H_{\phi_{(1)}}(A, \phi_0) \quad H_{\phi_{(1)}}(A, \phi_1) \cdots H_{\phi_{(1)}}(A, \phi_{2N-2})] \quad (3.27)$$

if the tangential components of the total magnetic field

are known.

By solving Equation (3.23), the unknown coefficients of the incident field which are included in the vector $\underline{\alpha}$ can be determined from one of the following equations. If the right hand side of Equation (3.23) is given by the tangential components of the total electric field as in Equation (3.26), then:

$$a_n = \frac{\alpha_n}{J_n(k_o A) + B_n H_n^{(2)}(k_o A)} \quad .... \quad -(N-1) \leq n \leq (N-1) \qquad (3.28)$$

where A is the radius of the measurement cylinder and B_n is given by Equation (3.17). On the other hand, if the right hand side of Equation (3.23) is known by measuring the tangential components of the magnetic field as given by Equation (3.27), then:

$$a_n = \frac{jn\ \alpha_n}{J_n'(k_o A) + B_n H_n^{(2)'}(k_o A)} \quad ... \quad -(N-1) \leq n \leq (N-1) \ . \qquad (3.29)$$

The matrix S given in Equation (3.24) is the general form for an arbitrary field distribution with respect to the ϕ-coordinate. If the geometry and the field have certain

symmetries about the x and the y coordinates, the field expansion can be selected to obey these symmetrical properties. In such cases the dimension of the S matrix can be reduced considerably, with corresponding reduction in the computational labour.

3.3 NUMERICAL INVESTIGATION OF THE TWO-DIMENSIONAL PROBLEM

The theory of this chapter is applied here to one of the simple field problems for which the exact solution is known, the scattering of a plane electromagnetic wave by a dielectric cylinder. The incident electric field can be written in its closed form as:

$$\underline{E}^i = E_o\, e^{-jk_o x}\, \hat{i}_z = E_o\, e^{-jk_o \rho \cos\phi}\, \hat{i}_z \quad . \tag{3.30}$$

Using a cylindrical wave transformation [21], we can express the incident field as:

$$\underline{E}^i = E_o \sum_{n=-\infty}^{\infty} j^{-n} J_n(k_o\rho)\, e^{jn\phi}\, \hat{i}_z$$

$$= E_o \{J_o(k_o\rho) + 2 \sum_{n=1}^{\infty} j^{-n} J_n(k_o\rho) \cos n\phi\}\, \hat{i}_z \quad . \tag{3.31}$$

Comparing the last equation with Equation (3.6), the exact

incident field coefficients a_n in this case are given by:

$$a_n = E_o\, j^{-n} \quad . \tag{3.32}$$

There is no loss of generality if we consider the amplitude of the incident wave E_o to be unity. These coefficients then become:

$$a_n = j^{-n} \tag{3.33}$$

We will now assume that the incident field is unknown and will attempt to reconstruct it using the theory developed in the last section. To determine the incident field we need the coefficients a_n. These coefficients can be determined by using the integration or the matrix methods described in section 3.2. In this section only the matrix method is utilized. The symmetry of the field and the geometry about the x-axis is used to reduce the number of unknowns by selecting only the cosine series for the field expansion. Truncating the series to N terms, the vector $\underline{\alpha}$ is given by Equation (3.25) for $0 \leq n \leq N-1$. The right hand side of Equation (3.23) can be obtained from the measurements of the tangential components of the total electric field E_z at N points on the measurement cylinder surface and distributed equally according to:

$$\phi_m = m\,\Delta\phi \ , \ m=0,1,2, \ldots, N-1 \qquad (3.34)$$

and

$$\Delta\phi = (\phi_{max} - \phi_{min})(N-1) \qquad (3.35)$$

where

$$\phi_{min} \leq \phi_o < \phi_1 < \ \ldots\ldots \ < \phi_{N-1} \leq \phi_{max} \ . \qquad (3.36)$$

Ideally, ϕ_{min} and ϕ_{max} are zero and 180 degrees, respectively. In the matrix method the point matching technique is utilized and the number of unknowns correspond to the number of measurements electric (or magnetic) field data. If more measurements could be performed, the unknowns may be evaluated using the method of least squares.

In this investigation the effects of the following parameters on the results are studied, they are [40]:

a) The truncation order N.

b) The effect of introducing $\pm$ 1% and $\pm$ 5% noise levels in the input data both in magnitude and phase.

c) The effect of restricting the measurements range in the ϕ direction to less than 180 degrees.

The numerical results of this chapter are obtained by using computer programs specifically prepared for this purpose [41].

3.3.1 Truncation Order and Truncation Errors of the Cylindrical Wave Functions

The cylindrical wave functions representing the electromagnetic field is an infinite series as discussed in the preceeding section. Since it is not practical to calculate such series on a digital computer, or, to solve an infinite number of linear alegbraic equations as in Equation (3.23) with $N \to \infty$ then it is required to truncate the infinite series to a certain order N. Many cases are investigated numerically of which only some cases are presented here. For example, the cases of N=12 to 15 are considered to calculate the unknown coefficients a_n of the incident field by using the matrix method as given by Equation (3.23). The required input data which is the tangential component of the total electric (or magnetic) field at $k_0A=10.0$ generated by inserting the exact coefficients of the incident field given by Equation (3.33) into the Equations (3.19) or (3.20). The unknown coefficients a_n of the incident field can be calculated by solving Equation (3.23) and using the relations in Equations (3.28) and (3.17). These calculated coefficients are used with Equation (3.6) to calculate the incident electric field. The magnitude and phase of this calculated electric field are compared with the exact ones and are shown in Figs. 3.2 and 3.3, respectively. In this investigation the radius of dielectric cylinder is taken to be $k_0a=1.0$, its permittivity $\varepsilon_r=2.0$, and the

incident field is calculated on a cylinder of radius $k_0\rho_1=10.0$. It is clear from these figures that, the series of the cylindrical function representing incident field converge to the exact one, as expected, by increasing the truncation order N.

To study the effect of truncation error in the results, dielectric cylinders of $\varepsilon_r=2.0$ and radii $k_0a=1.0$, 2.0, 3.0, 4.0 and 5.0 are selected. Measurement data are generated on cylinders of radii $k_0A=4.0$, 5.0, 6.0 and 10.0 and the incident field is reconstructed on a cylinder of radius $k_0\rho_1=10.0$. To compare the reconstructed data with the exact one, a percentage truncation error is defined by:

$$\text{Percentage truncation error} = \frac{\left|\,|\text{exact value}| - |\text{calculated value}|\,\right|}{|\text{exact value}|} \times 100\% \qquad (3.37)$$

using this definition, the mean of the percentage truncation error of the magnitude and the phase of the incident field are calculated and plotted against the truncation order N in Figs. 3.4 and 3.5, respectively. These figures are sample examples from many cases which were investigated. All of these have similar results. It is found from this analysis, that to retain the maximum error at less than 0.5% the number

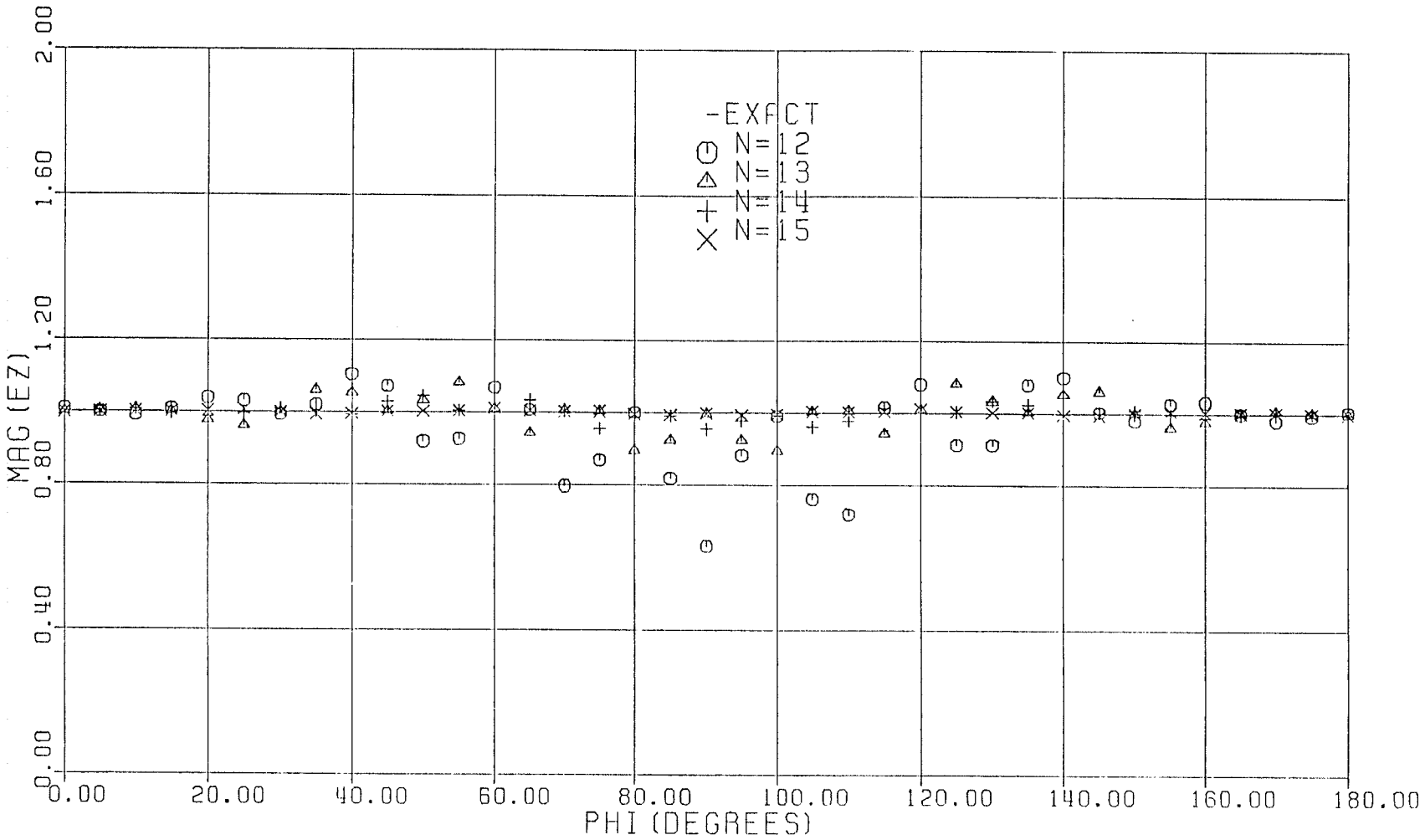

Fig. 3.2: Comparison of the magnitude of the calculated incident electric field using cylindrical expansion functions with the exact one.

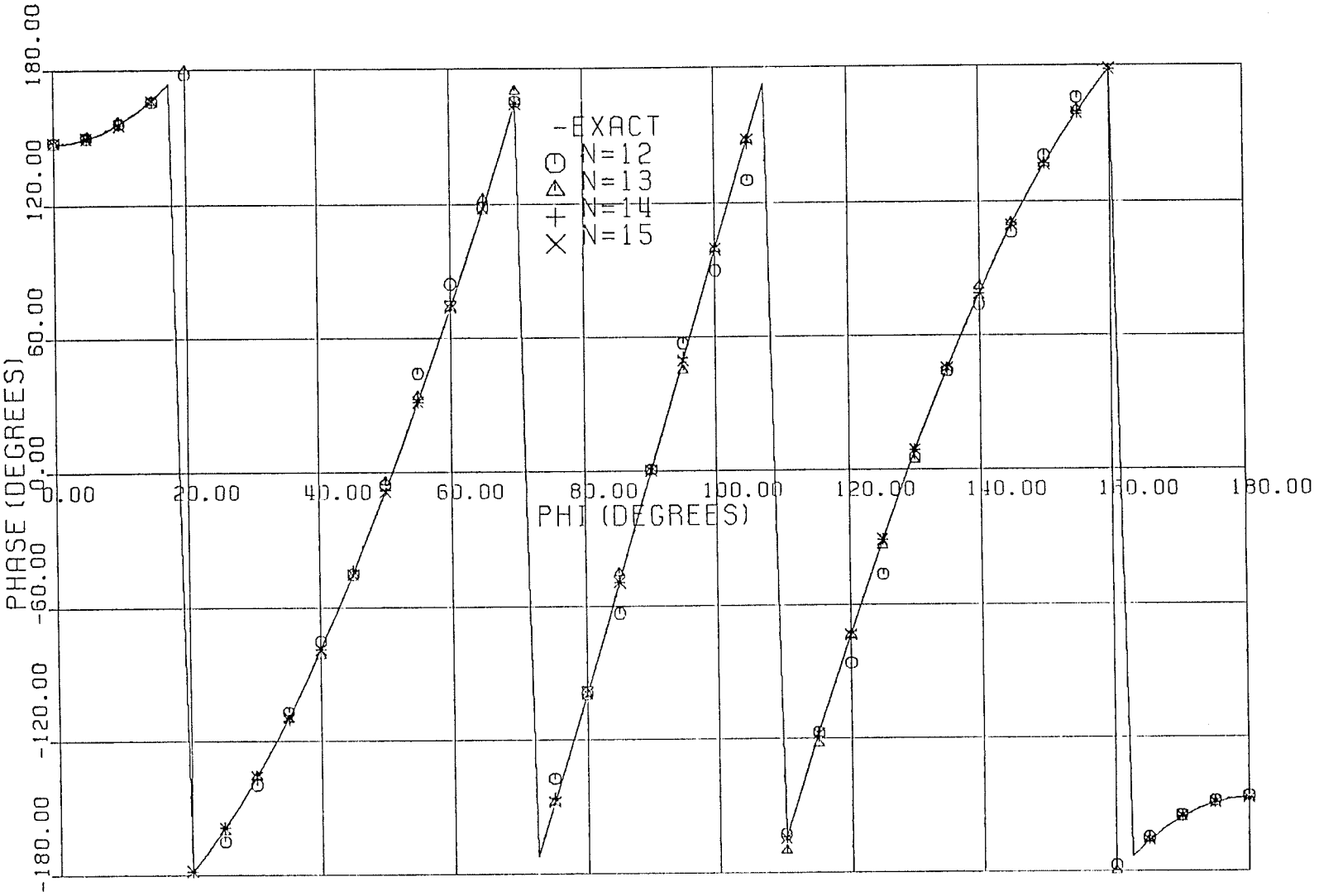

Fig. 3.3: Comparison of the phase of the calculated incident electric field using cylindrical expansion functions with the exact one.

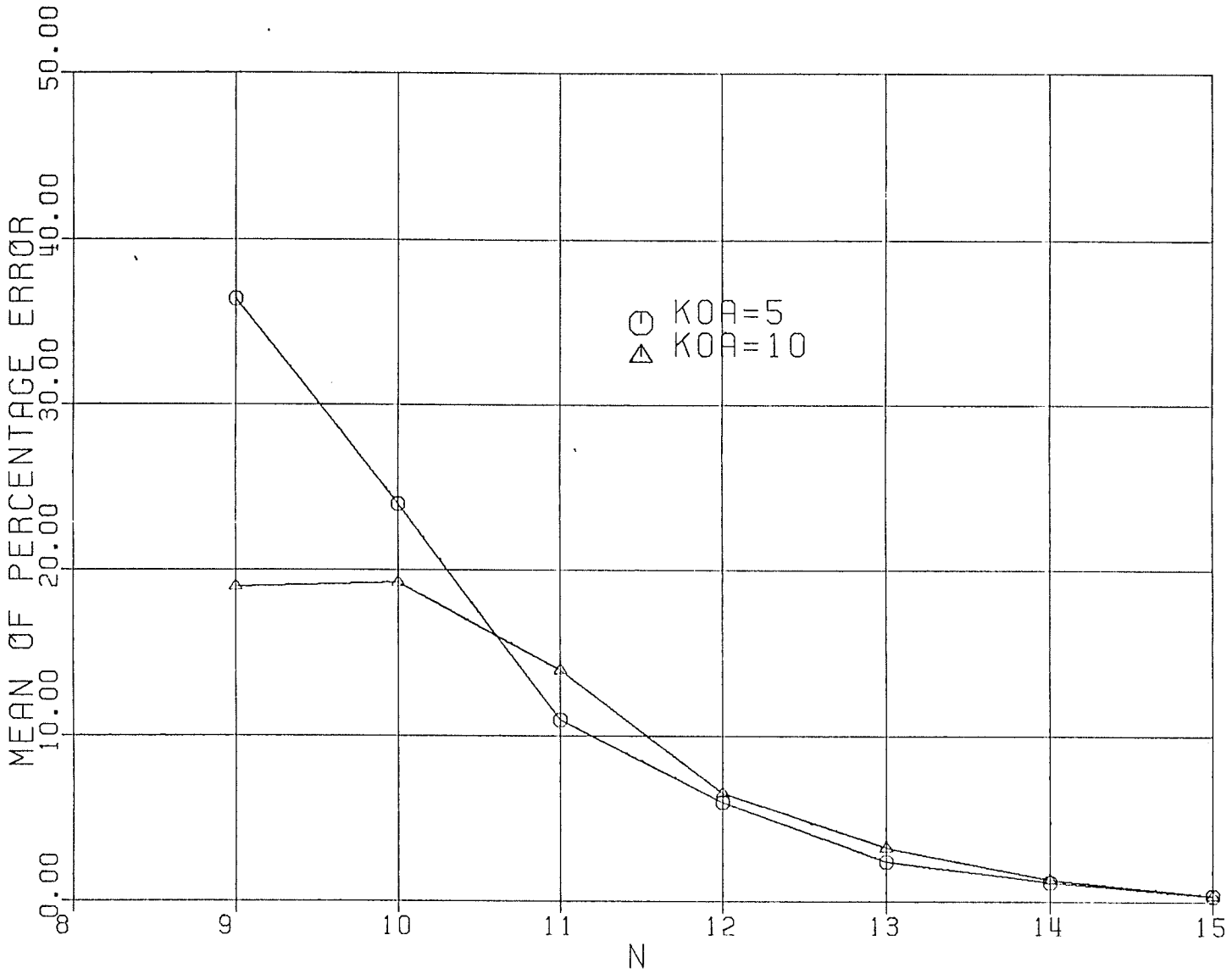

Fig. 3.4: Truncation error of the magnitude of the calculated incident field with truncation order N.

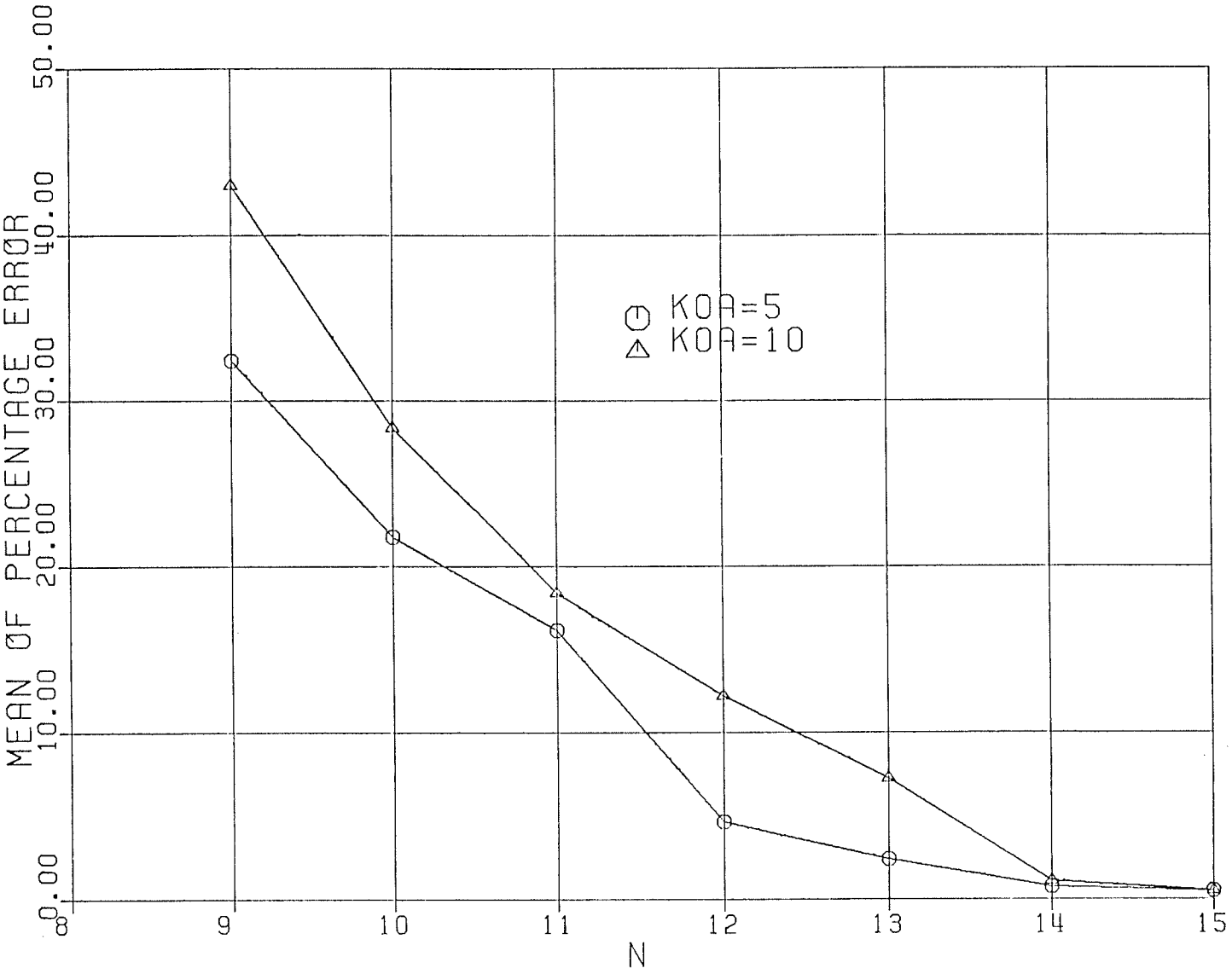

Fig. 3.5: Truncation error of the phase of the calculated incident field with truncation order N.

of cylindrical functions N in the series must satisfy the relationship $N \geq 3\ k_0 a$ and $N \geq 1.5\ k_0 A$.

3.3.2 The Effect of Angular Measurement Range

Ideally, the angular measurement range is limited to $0 \leq \phi \leq 180°$. However, in practice it may be desirable to limit the measurements to a smaller angular range. This section examines the effect of smaller measurement ranges on the accuracy of the reconstructed field. The problem again is an unknown plane wave scattered by a dielectric cylinder and the incident field is obtained from the measurement of the total field.

It is known that in reconstructing the incident field from the measurement data over a cylinder, the matrix inversion of Equation (3.24) is the most stable one if the measurement points are located symmetrically about the $\phi = 90°$ direction [42]. In this study therefore the incident plane wave is reconstructed from the measurements over several ranges located symmetrically about $\phi = 90°$. Figs. 3.6 and 3.7 compare the magnitude and the phase of the calculated incident electric fields, using 15 terms from cylindrical expansion functions with the exact ones. The results of these figures are for different measurement ranges of $0 \leq \phi \leq$

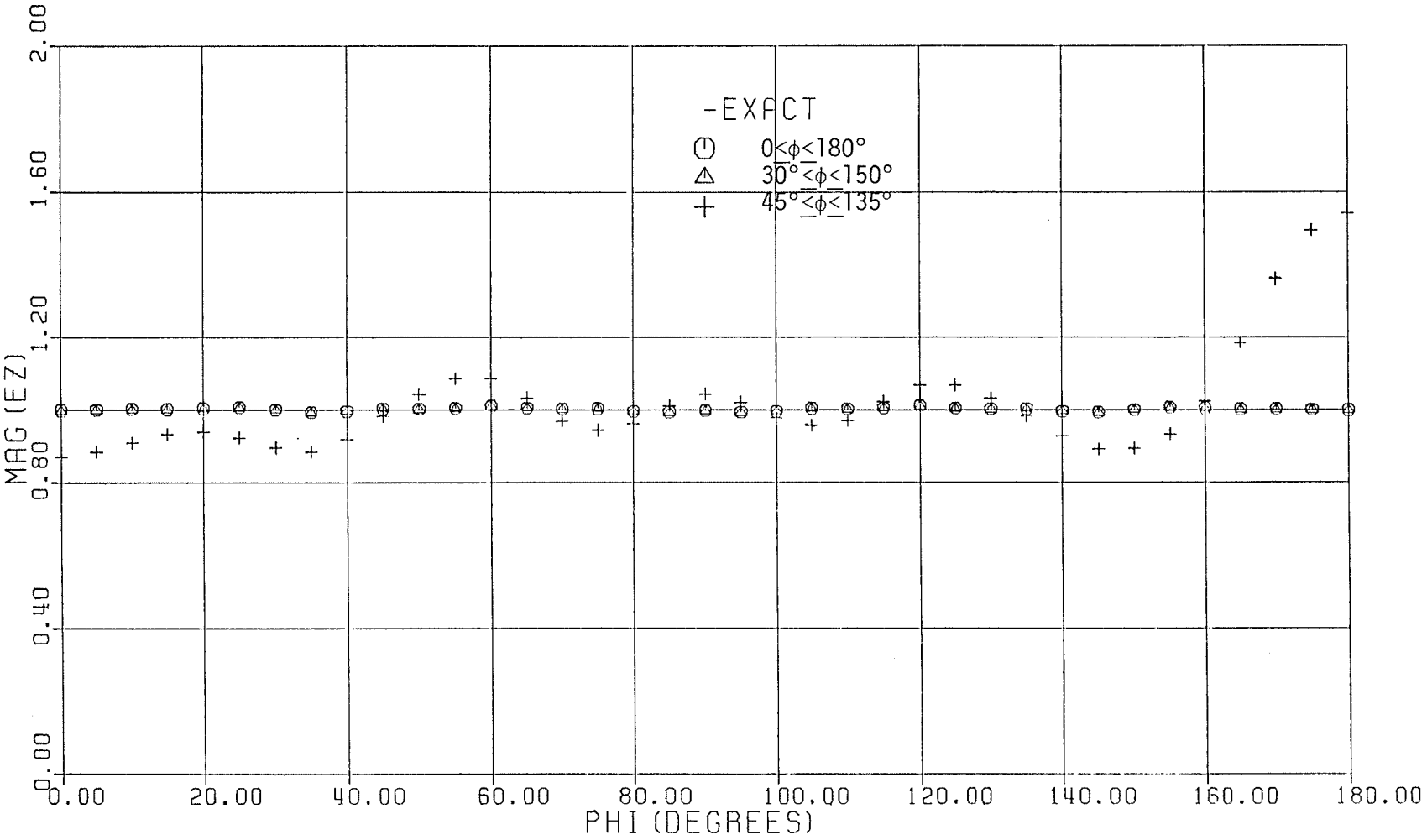

Fig. 3.6: Comparison of the magnitude of the calculated incident field with the exact one, different measurement ranges.

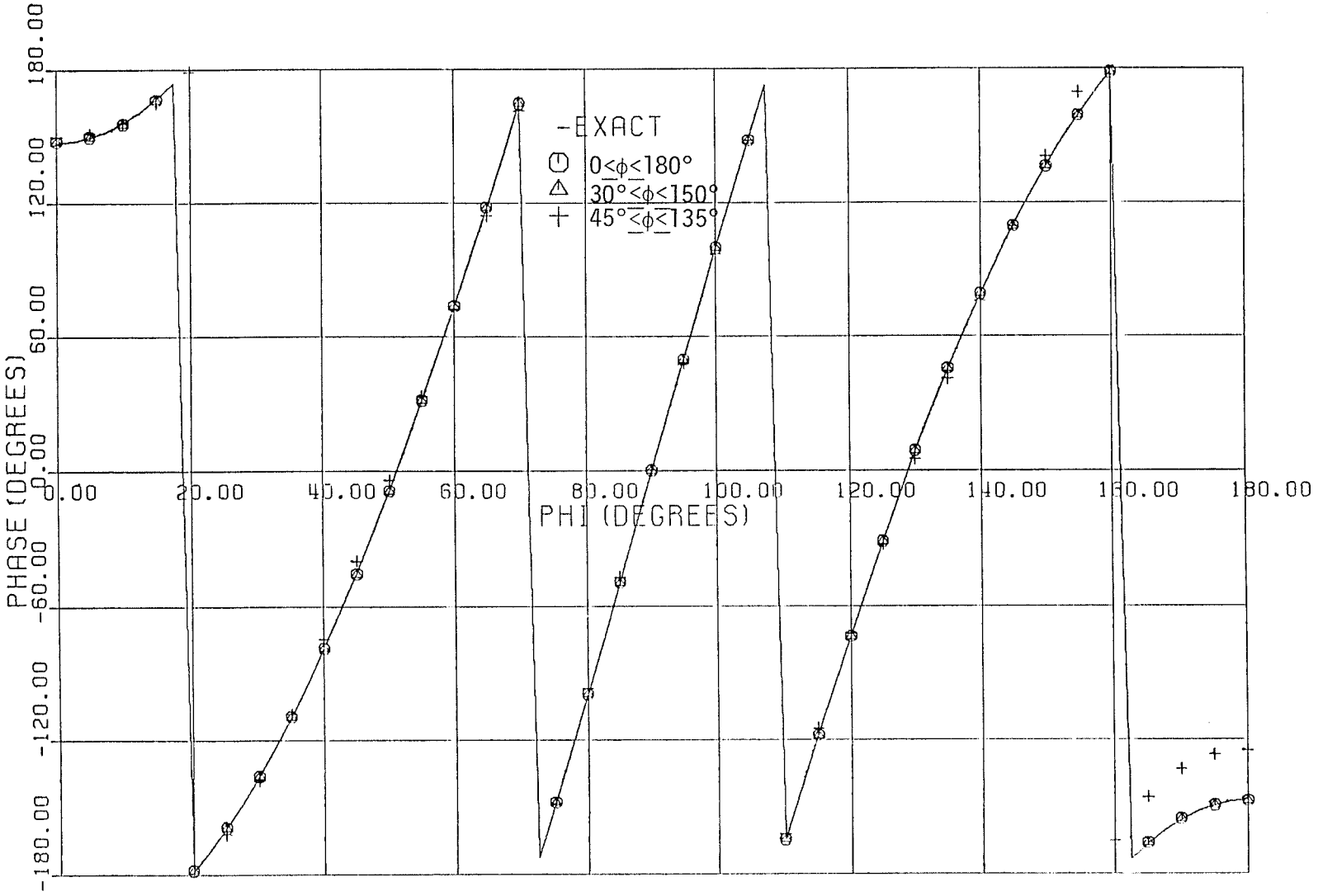

Fig. 3.7: Comparison of the phase of the calculated incident field with the exact one, different measurement ranges.

180°, $30° \leq \phi \leq 150°$ and $45° \leq \phi \leq 135°$. The corresponding percentage errors are 0.326%, 0.335% and 9.22% in the field magnitude and 0.48%, 0.48% and 10.18% in the field phase, respectively.

From these results it is evident that a reasonable data for the reconstructed field can be obtained from smaller ranges of the measurement than $0 \leq \phi \leq 180°$. By decreasing the measurement range, initially, the accuracy of the results decreases slowly, but the increase in the magnitude of the error accelerates when the measurement range decreases below $45° \leq \phi \leq 135°$.

3.3.3 Measurement Noise Effect

To know any component of the electric or the magnetic field, we need to measure its magnitude and phase. From a practical point of view, however, any measurement result will contain certain error components in both amplitude and phase, which may be due to equipment limitations, environmental noise or both. Because, these error components are unwanted portions of the data, they may be considered as, noise signals. They involve both positional error of the probe and the measurement errors. The effect of these noises on the calculated field using the technique of this chapter will be discussed here. A simulation of these noises on the digital computer can be

done by introducing a random error within certain limits to the input data. This input data is the tangential component of the total electric (or magnetic) field at a radius $\rho = A > a$. At each measurement point in space, the magnitude and the phase should be measured. The simulation of these data on the computer can be done using Equation (3.10) for the total electric field at $k_o\rho = k_oA$ and using Equations (3.16) and (3.17). Also, the exact coefficients a_n given by Equation (3.33) can be inserted in Equation (3.10) to generate the required data. In this noise investigation, three cases are considered: (statistically independent noises)

a) $\pm$ 1% and $\pm$ 5% random noises are added to the magnitude of the total electric field.

b) $\pm$ 1% and $\pm$ 5% random noises are added to the phase of the total electric field.

c) $\pm$ 1% and $\pm$ 5% random noises are added to both magnitude and phase of the total electric field.

The calculated incident field using the generated total electric field data with the introduced random noises are compared with the exact one and are shown in Fig. 3.8 to Fig. 3.13. The percentage errors in these cases are given in Table 3.1. The cylindrical expansion functions with 15 terms are used in this investigation. Figs. 3.8 and 3.9 show the effect of introducing $\pm$ 1% and $\pm$ 5% random noises on the

magnitude of the calculated incident electric field at $k_0\rho_1=10.0$. The random noises are added to the magnitude of the total electric field, which is generated on the surface of a measurement cylinder of radius $k_0A=10.0$. As expected, these figures show that the introduction of noise into the amplitude of the electric field deteriorates the accuracy of reconstructed incident field. However, it is interesting to note that the accuracy of the phase results has not deteriorated as much as the amplitude results. It is thus clear that since the noise is introduced only in the magnitude of the input data, the accuracy has worsened more in the magnitude of the incident field than that of its phase. This is also clear in the case of introducing noise in the phase only, which affects the phase of the incident field more than the magnitude as shown in Figs. 3.10 and 3.11. However, comparing the results of the above cases, one notes that the introduction of noise in the phase affects the accuracy of the final results much more than addition of the noise in the amplitude.

In the third case, which is the combination of the last two, the noise is introduced in both magnitude and phase of the input data. For this reason, this case is more practical than the previous cases. Comparing the results of this case, Figs. 3.12 and 3.13, with previous ones, it

becomes evident that an addition of noise in both phase and amplitude does not affect the accuracy as much as adding the noise to only the phase. To investigate this more carefully the percentage errors for each of the above cases are also calculated and are shown in Table 3.1 with those of no noise case. All data of this table are computed by retaining first 15 terms of the expansion series. Comparing the data of these three cases with the exact case, it becomes clear that the addition of noise in the phase has the worst effect on the result. Furthermore, addition of noise only in the phase is worse than its addition to both. In all cases, however, the results tend to deteriorate as the noise level is increased. Since the latter case is the most practical one, it seems a small amount of experimental error does not affect the final data too adversely.

3.4 DISCUSSIONS

This chapter considered the solution of two-dimensional inverse source problem. The theoretical analysis was presented only for the transverse magnetic (TM) fields, but a similar analysis can be carried out for the transverse electric (TE) or any general two-dimensional fields.

The specific problem considered consisted of an unknown incident field and a dielectric cylinder which scattered the

Table 3.1: The percentage errors in the calculated magnitude and phase of the incident electric field E_z^i due to introduction of ± 1% and ± 5% random noises in the input data.

Input data / Output % errors	No Noise Introduced	Noise introduced in magnitude only		Noise introduced in phase only		Noise introduced in magnitude and phase	
		± 1%	± 5%	± 1%	± 5%	± 1%	± 5%
Percentage errors in magnitude of the calculated E_z^i	0.325%	1.104%	3.13%	0.85%	2.544%	0.852%	2.338%
Percentage errors in phase of the calculated E_z^i	0.478%	0.615%	1.66%	3.35%	6.43%	2.044%	6.43%

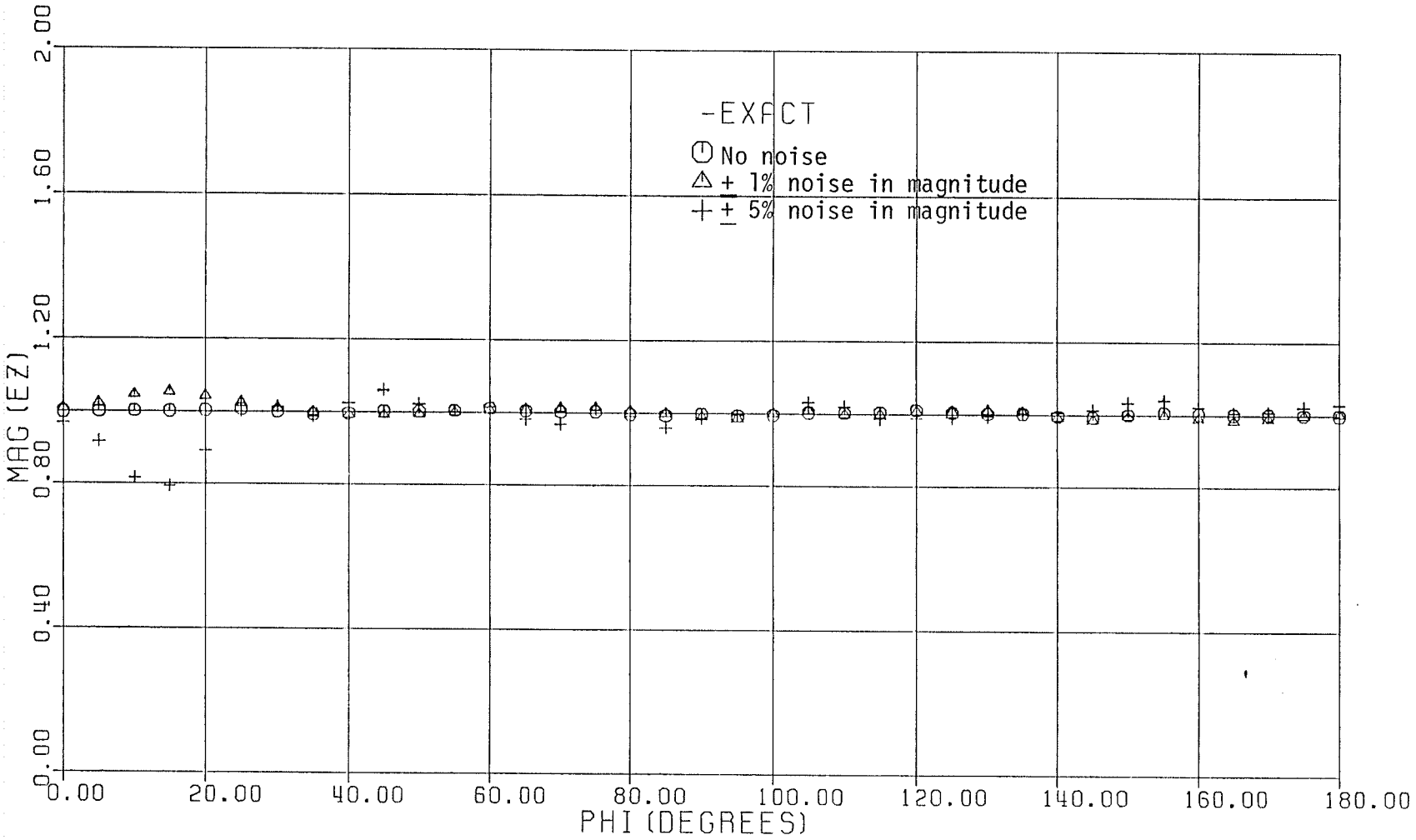

Fig. 3.8: Magnitude of the calculated incident field with ± 1% and ± 5% random noises in the magnitude of the total field.

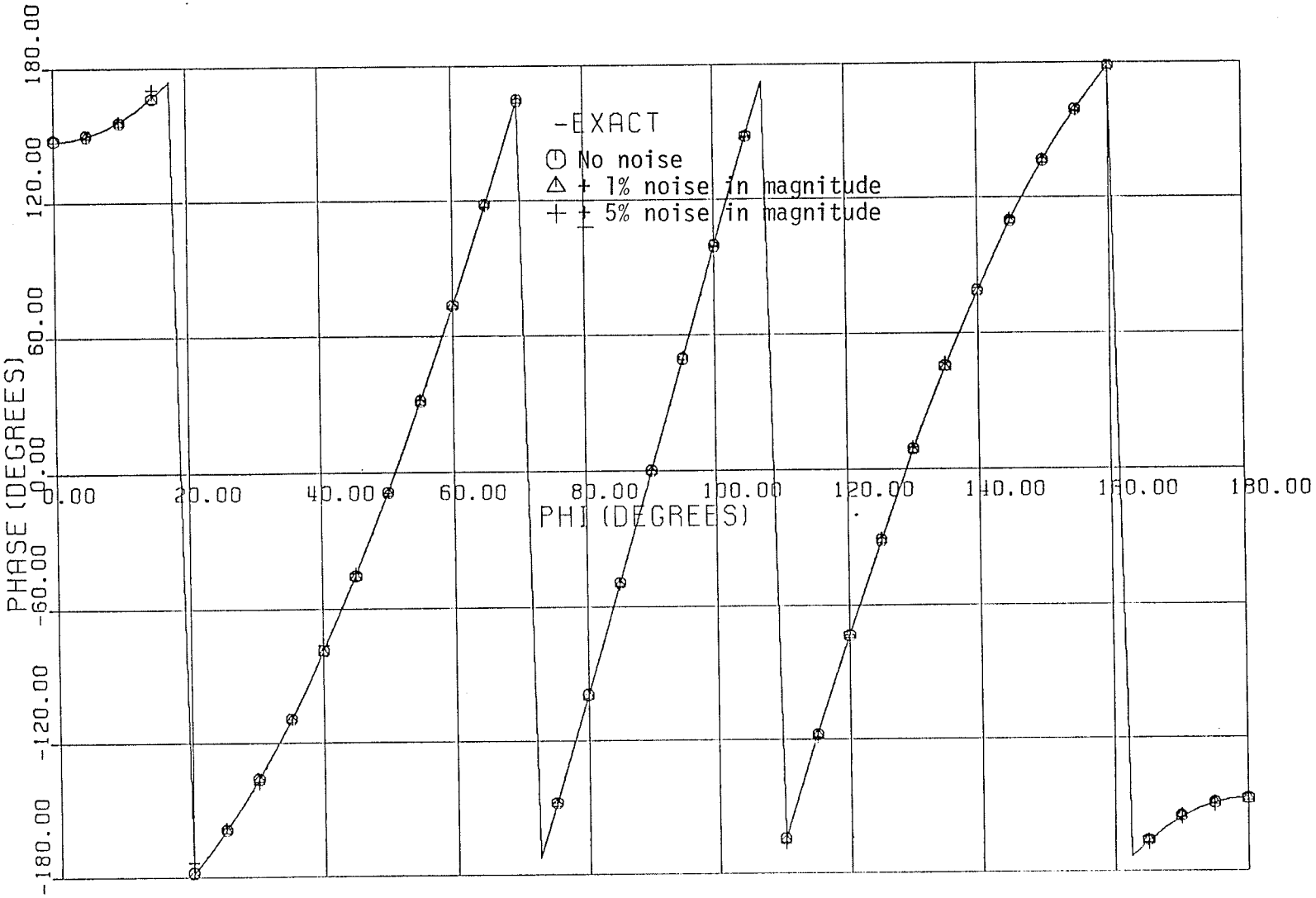

Fig. 3.9: Phase of the calculated incident field with ± 1% and ± 5% random noises in the magnitude of the total field.

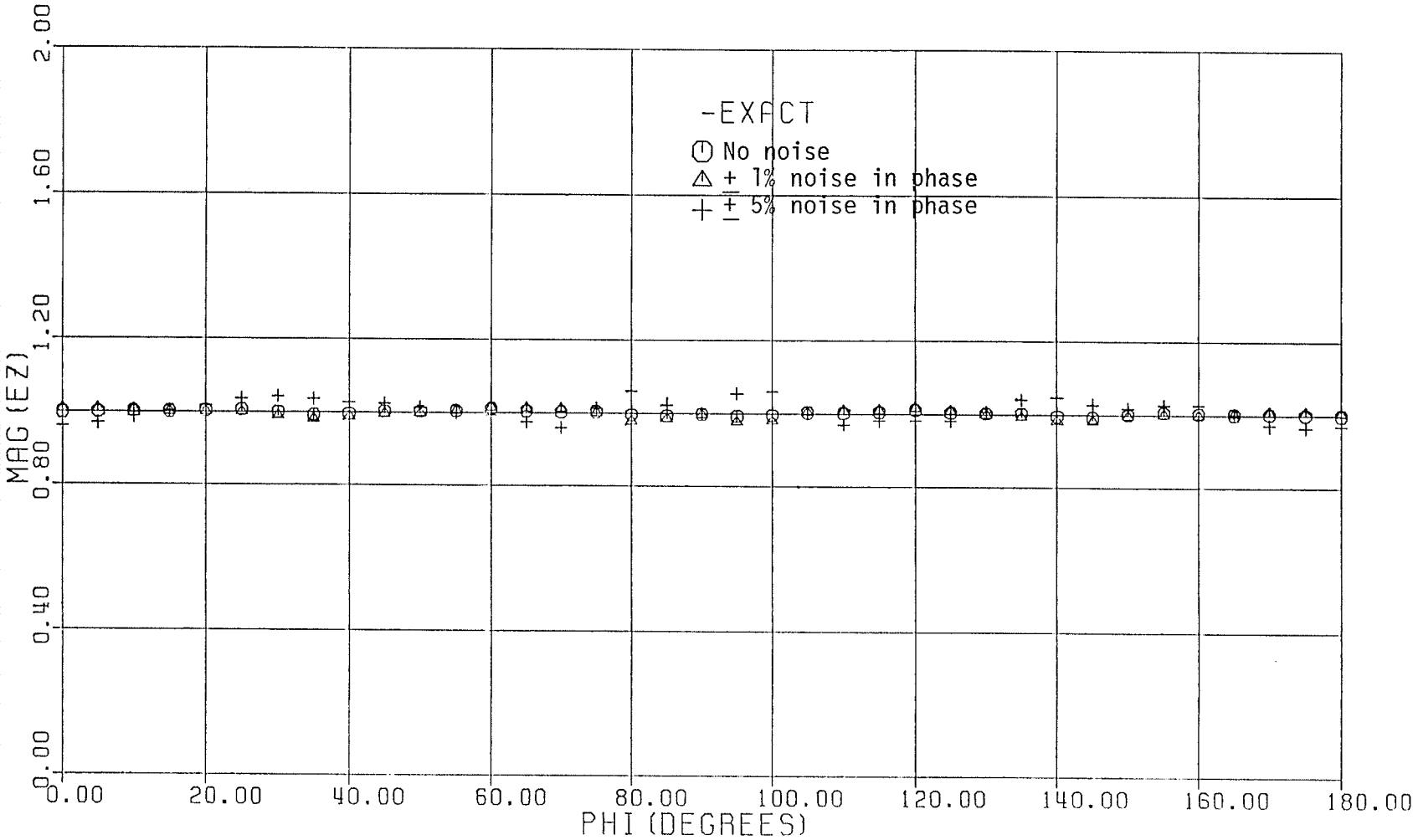

Fig. 3.10: Magnitude of the calculated incident field with ± 1% and ± 5% random noises in the phase of the total field.

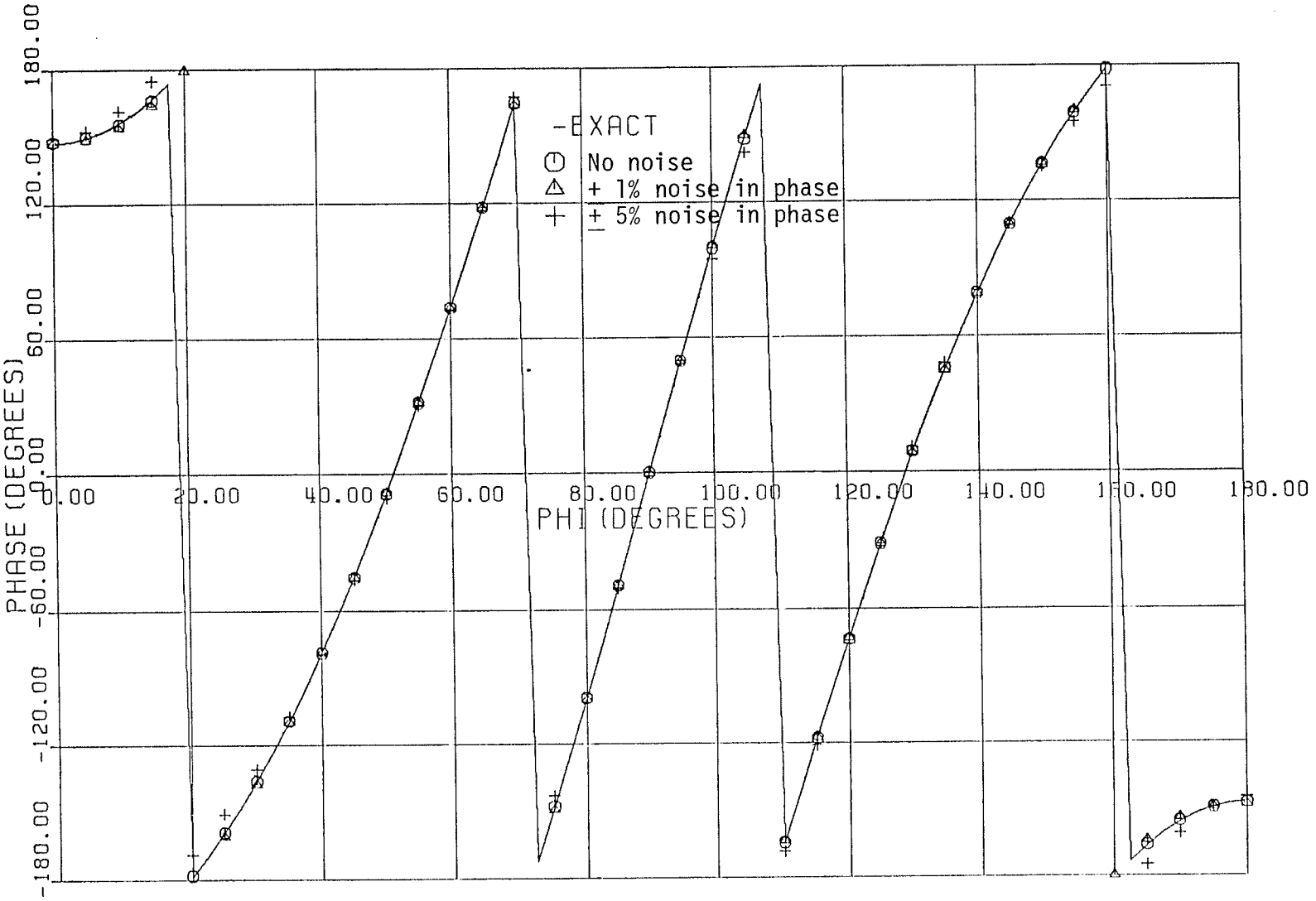

Fig. 3.11: Phase of the calculated incident field with ± 1% and ± 5% random noises in the phase of the total field.

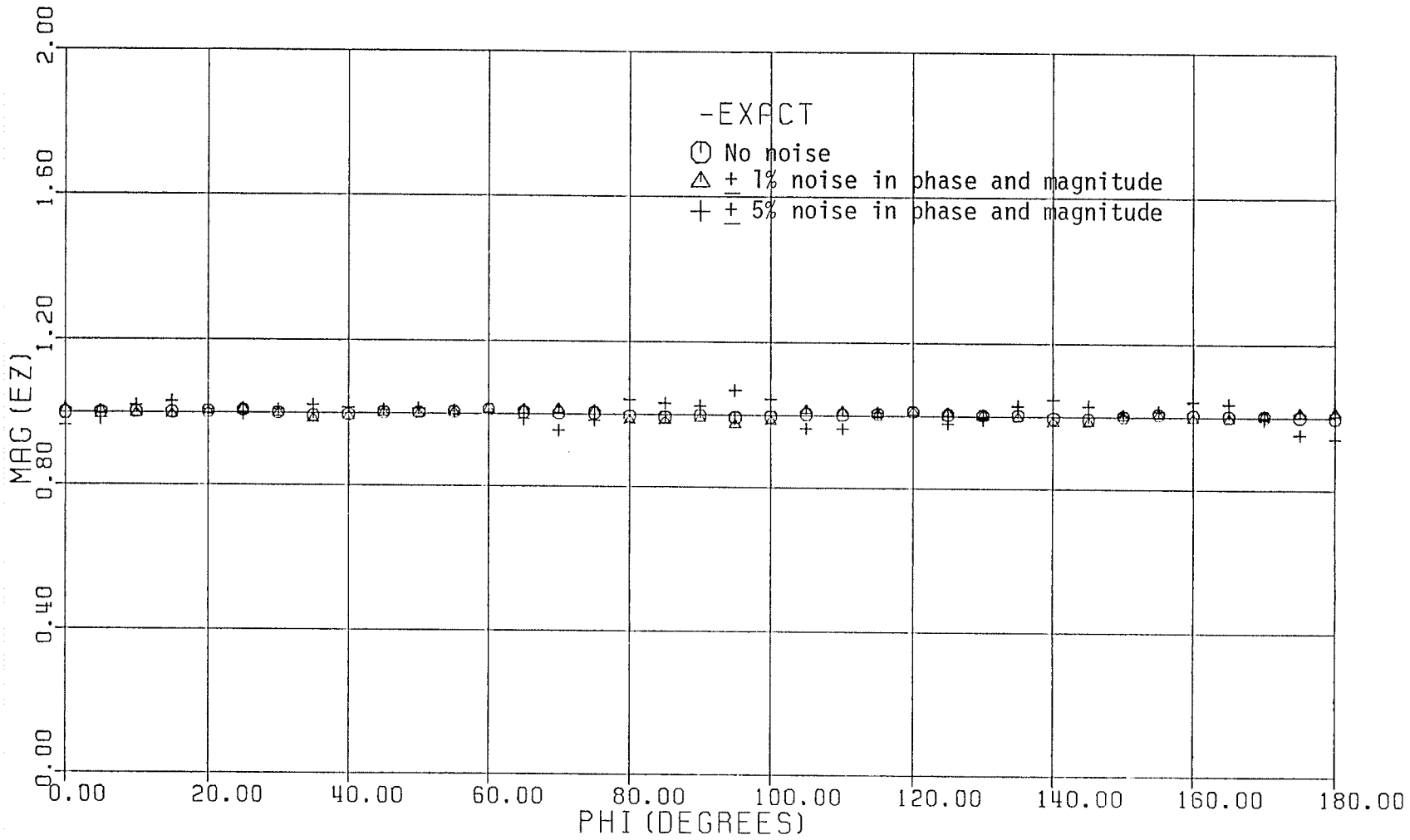

Fig. 3.12: Magnitude of the calculated incident field with ± 1% and ± 5% random noises in the phase and the magnitude of the total field.

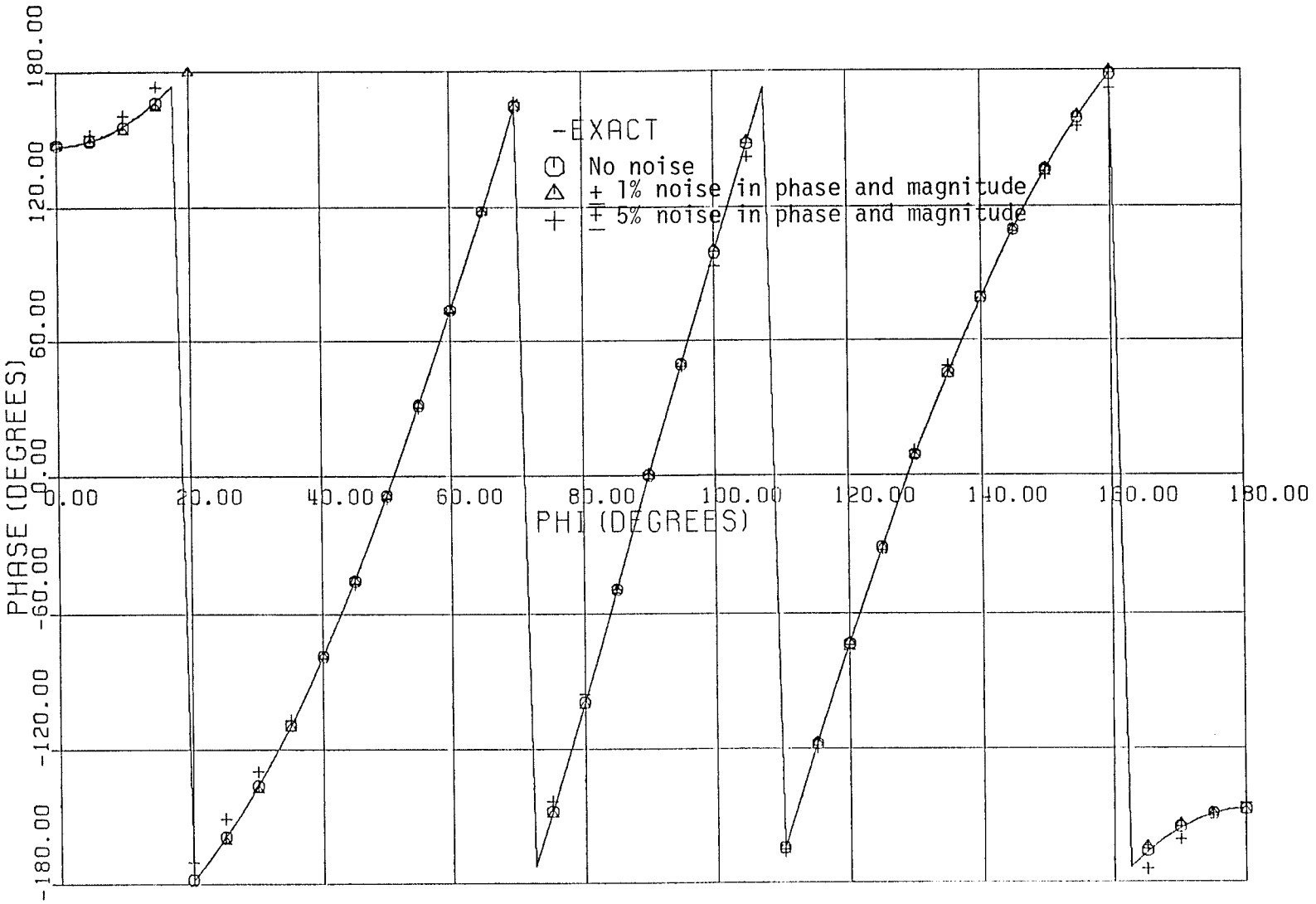

Fig. 3.13: Phase of the calculated incident field with ± 1% and ± 5% random noises in the phase and the magnitude of the total field.

incident field. To formulate the problem, cylindrical wave functions were used to represent the incident, the scattered and the total fields. Boundary conditions were applied to obtain a matrix relationship between the coefficients of the unknown incident field and those of the known total field. This formulation has been used to study the effects of the number of cylindrical wave functions, angular range of measurement points and inaccuracies in the measurement data, on the accuracy of the incident field reconstruction. For simplicity a plane wave was used as an incident field and the measurement data were generated numerically.

To study the effect of truncation error in the results, dielectric cylinders of $\varepsilon_r = 2.0$ and radii $k_0 a = 1.0, 2.0, 3.0, 4.0$ and 5.0 were selected. Measurement data were generated on cylinders of radii $k_0 A = 4.0, 5.0, 6.0$ and 10.0 and the incident field was reconstructed on a cylinder of radius $k_0 \rho_1 = 10.0$. Comparing the reconstructed data with the exact one, it was found that to retain the maximum error at less than 0.5%, the number of cylindrical functions N in the series must satisfy the relationships $N \geq 3\, k_0 a$ and $N \geq 1.5\, k_0 A$.

The effect of angular range of the measurement points on the accuracy of the results was also studied. It was found that limiting the measurement point to a range less than $0 \leq \phi \leq 180°$ reduces the accuracy of the reconstructed field.

However, the decrease in the accuracy was negligibly small, as long as, the measurement range was retained between 45° and 135°. Further reduction of the measurement range deteriorated the accuracy at an accelerated rate.

Finally, the measurement inaccuracies were simulated by modifying the exact data by a small percentage in a random manner. It was found that inaccurate data in only magnitude, or, phase of the measured field affects its respective reconstructed data of the incident field by a larger percentage. An error in the magnitude of the measured field, introduces larger error in the amplitude of the reconstructed field than in its phase. Furthermore, an error in the phase caused more severe effect on the results than an error in the amplitude. The most interesting information was found in introducing erorrs in both amplitude and the phase of the measurement data. The investigation showed that introducing errors in both amplitude and the phase has much less effect on the accuracy of the reconstructed field than introducing these errors in only the phase.

CHAPTER IV

THREE-DIMENSIONAL INVERSE SOURCE PROBLEM: THEORY

4.1 INTRODUCTION

In this chapter, the theoretical analysis of the three-dimensional inverse source problem is discussed. In this analysis, the spherical wave expansion which forms a basis for solving Maxwell's equations will be utilized. The basic properties of spherical waves have been described by reference [36]. The problem is similar to that discussed in the last chapter. Namely, a radiator with unknown radiation characteristics is in the presence of a dielectric scatterer and it is desired to reconstruct its radiation fields from a set of measurement data. However, the scatterer in this case is a dielectric sphere. The problem has practical significance, since, spherical dielectrics are occasionally used to shape the radiation patterns of the waveguides, horns and other radiating systems [48]. Also, the introduction of the scatterer in the vicinity of a radiator can improve the intensity of the wide angle field distributions and facilitate the accurate measurement of the near-field.

Since in this chapter a spherical scatterer is considered, a spherical near-field far-field transformation method will be used. Furthermore, to avoid large scanning systems,

required for large antennas, a stepwise approach as described in section 2.6, in which the near-field is measured over a small spherical surface in the vicinity of the scatterer is selected. The required information on the field and over a surface enclosing the antenna is then obtained by repeating the measurement at several locations around the antenna. This stepwise approach not only reduces the required scanning surface, but also reduces the expansion of antenna field over a large surface to several expansions over small surfaces. Note that when the dielectric constant of the scatterer becomes unity the problem reduces to the near-field measurement of an isolated antenna. In the following sections, the details of the method are described and a mathematical formulation is presented.

4.2 METHOD OF MEASUREMENT

Fig. 4.1 shows the geometry of the problem. A scattering sphere of radius a is located in the vicinity of an antenna with unknown radiation characteristics. When a spherical surface S enclosing both the sphere and the antenna is small in size the measurement can be carried out over this sphere to obtain the total field. In addition, the field outside S can be described by spherical wave functions with unknown coefficients. These unknown coefficients can then be obtained by matching the measured and the spherical wave expansion fields over the spherical surface S.

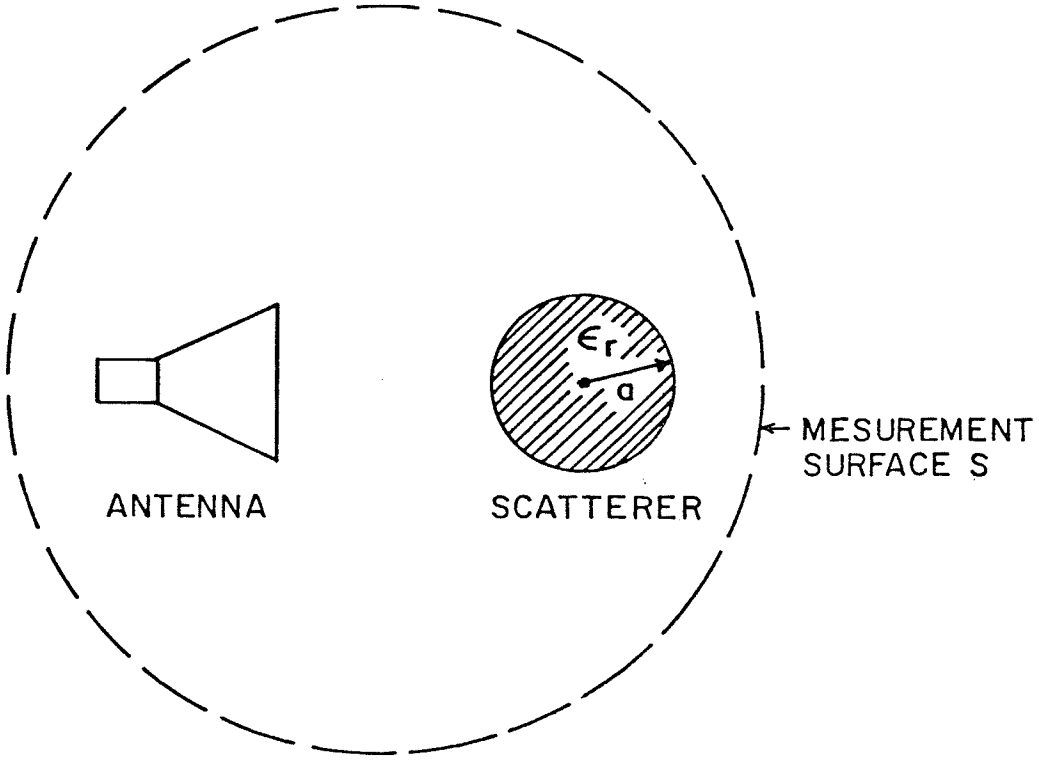

Fig. 4.1: Schematic diagram showing the antenna, the scattering sphere and the measurement surface S.

On the other hand, when the antenna, or its separation distance from the scattering sphere is large, the spherical surface enclosing them also becomes large. The measurement of the field over such a large surface requires large scanning systems, which in practice is undesirable. To utilize a small scanning system the proposed measurement steps of Fig. 4.2 can be used. In this system, the measurements are carried out over smaller surfaces defined as S_1, S_2, S_3, ... These results are then used to compute the field over the surface S, which encloses the antenna and the scatterer. The required field outside S can then be obtained by the above spherical wave expansion approach.

To obtain the field over the surface S, the following steps can be used:

1. Within the expansion sphere S_1', which includes both the measurement sphere S_1 and the scatterer, the fields inside the scattering sphere and between its surface and S_1' are described by spherical wave functions with unknown coefficients. These unknown coefficients are obtained by matching the calculated and the measured fields over S_1.

2. Within S_2', S_3' ... fields are also described by spherical wave functions about the origin of each surface and

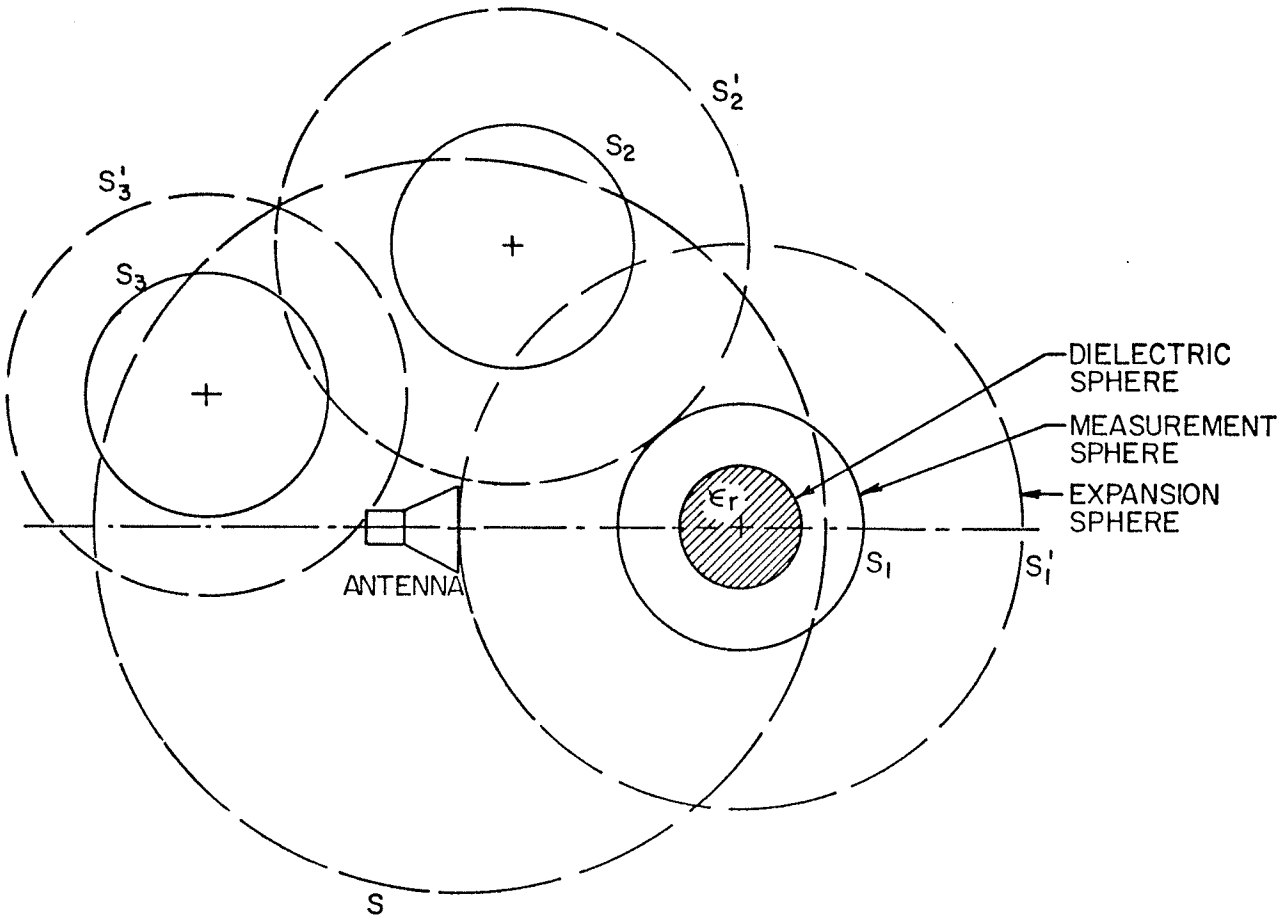

Fig. 4.2: Schematic diagram of the antenna, the scatterer and different measurement and expansion spheres.

their unknown coefficients are found after the matching of their respective fields.

Following these steps the total fields are known within the expansion spheres S_1', S_2', S_3', ... and can be used to calculate the required field components over the surface S. Note that, the expressions for the field inside S_2', S_3', ... can be obtained from the expressions of the field inside S_1', by replacing its dielectric constant with unity. The problem therefore reduces to the evaluation of the unknown field coefficients for field inside S_1' and calculation of the required field components over S which fall within S_1'. In the following sections the expansion functions will be discussed and the formulations will be utilized to compute the fields of the test antenna.

4.3 METHOD OF ANALYSIS

4.3.1 Expansion of the Electromagnetic Fields Within S_1'

Considering the geometry of Fig. 4.3, let the origin of the coordinate system be at the center of the dielectric sphere at a distance $r(=b > a)$ from the test antenna. A sphere V_1, concentric with the dielectric sphere and its surface S_1' tangent to the test antenna is defined. Let the region between the spherical surface S_1' and the surface of the dielectric sphere be named region (1). Also, let the region inside the

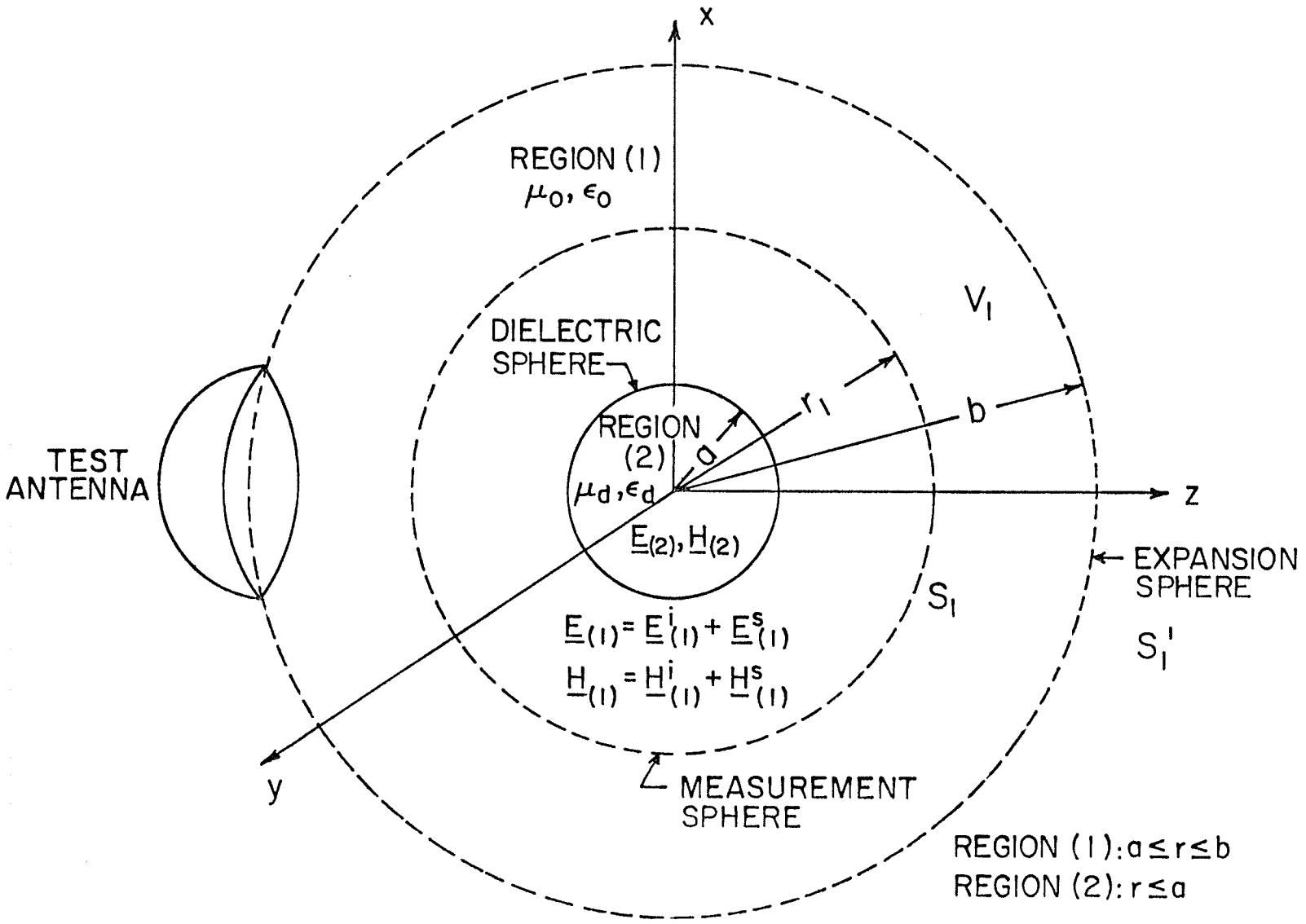

Fig. 4.3: Schematic diagram of the test antenna, dielectric sphere, and the coordinate system.

dieletric sphere ($r \leq a$) be called region (2). To solve the problem, the incident electromagnetic field in region (1) can be expanded in terms of appropriate spherical wave functions. The latter expansion is weighted by its unknown coefficients within two infinite series in m and n, where m and n are the eigen values of the ϕ and θ coordinates in the spherical coordinates. The truncation of the infinite series in n to N terms is necessary to calculate the unknown coefficients. The infinite series in m is terminated at n since the associated Legendre polynomials $P_n^m(\cos\theta)$ are equal to zero for m larger than n. The scattered electromagnetic field in region (1) will also be expanded in terms of spherical wave functions. Similarly, in region (2), the total electromagnetic field will be expanded with its weighted coefficients. The boundary conditions of this problem is the continuity of the total electromagnetic fields on the surface of the dielectric sphere (r=a). By applying these boundary conditions, a relationship between the scattered and the total electromagnetic field coefficients in terms of the incident field coefficients can be obtained. In this manner, the total electromagnetic field in region (1) can be expressed in terms of the unknown incident field coefficients. Also, $K=2N(N+2)$ simultaneous equations for K unknown coefficients can be obtained by matching the tangential electric and magnetic fields. These matching points will be located on the surface of the measure-

ment sphere of radius $r=A(a \leq A \leq b)$. By solving the system of K linear algebraic equations with K-unknowns, the unknown coefficients of the incident field can be calculated. Substituting the calculated coefficients in the incident electromagnetic field expansions, the incident field will be known.

Define the incident and the scattered electromagnetic fields in region (1), as $\underline{E}^{i}_{(1)}$, $\underline{H}^{i}_{(1)}$, and $\underline{E}^{s}_{(1)}$, $\underline{H}^{s}_{(1)}$, respectively. Then the total fields in this region are:

$$\underline{E}_{(1)} = \underline{E}^{i}_{(1)} + \underline{E}^{s}_{(1)} \tag{4.1}$$

$$\underline{H}_{(1)} = \underline{H}^{i}_{(1)} + \underline{H}^{s}_{(1)} \quad . \tag{4.2}$$

The incident and the scattered fields in region (1) can be written in terms of the spherical wave functions [33], [34] and [37]. They can be written in the form (the time dependence $\exp(j\omega t)$ is implicitly assumed):

$$\underline{E}^{i}_{(1)} = - \sum_{n=1}^{N} \sum_{\substack{m=0 \\ e,o}}^{n} \left(a_{mn}^{e}{}_{o} \, \underline{m}^{(1)}_{mn}{}^{e}_{o} + b_{mn}^{e}{}_{o} \, \underline{n}^{(1)}_{mn}{}^{e}_{o} \right) \tag{4.3}$$

$$\underline{H}^{i}_{(1)} = \frac{k_o}{j\omega\mu_o} \sum_{n=1}^{N} \sum_{\substack{m=0 \\ e,o}}^{n} \left(a_{mn}^{e}{}_{o} \, \underline{n}^{(1)}_{mn}{}^{e}_{o} + b_{mn}^{e}{}_{o} \, \underline{m}^{(1)}_{mn}{}^{e}_{o} \right) \tag{4.4}$$

$$\underline{E}^{s}(1) = - \sum_{n=1}^{N} \sum_{\substack{m=0 \\ e,o}}^{n} \left(c_{\substack{e \\ o}}{}_{mn} \underline{m}^{(4)}_{\substack{e \\ o}}{}_{mn} + d_{\substack{e \\ o}}{}_{mn} \underline{n}^{(4)}_{\substack{e \\ o}}{}_{mn} \right) \tag{4.5}$$

and

$$\underline{H}^{s}(1) = \frac{k_o}{j\omega\mu_o} \sum_{n=1}^{N} \sum_{\substack{m=0 \\ e,o}}^{n} \left(c_{\substack{e \\ o}}{}_{mn} \underline{n}^{(4)}_{\substack{e \\ o}}{}_{mn} + d_{\substack{e \\ o}}{}_{mn} \underline{m}^{(4)}_{\substack{e \\ o}}{}_{mn} \right) \tag{4.6}$$

where:

$\underline{m}^{(i)}_{\substack{e \\ o}}{}_{mn}$ and $\underline{n}^{(i)}_{\substack{e \\ o}}{}_{mn}$ are the spherical vector wave functions and are solutions to Maxwell's equations given in the spherical coordinate system given by:

$$\underline{m}^{(i)}_{\substack{e \\ o}}{}_{mn} = \mp \frac{mP_n^m(\cos\theta)}{\sin\theta} z_n^{(i)}(kr) \begin{matrix} \sin \\ \cos \end{matrix} m\phi \hat{i}_\theta - z_n^{(i)}(kr) \frac{\partial P_n^m(\cos\theta)}{\partial\theta} \begin{matrix} \cos \\ \sin \end{matrix} m\phi \hat{i}_\phi \tag{4.7}$$

$$\underline{n}^{(i)}_{\substack{e \\ o}}{}_{mn} = \frac{n(n+1)}{kr} z_n^{(i)}(kr) P_n^m(\cos\theta) \begin{matrix} \cos \\ \sin \end{matrix} m\phi \hat{i}_r + \frac{1}{kr} \frac{\partial}{\partial r} [r z_n^{(i)}(kr)] \frac{\partial P_n^m(\cos\theta)}{\partial\theta} \begin{matrix} \cos \\ \sin \end{matrix} m\phi \hat{i}_\theta \mp \frac{mP_n^m(\cos\theta)}{\sin\theta} \frac{1}{kr} \frac{\partial}{\partial r} [r z_n^{(i)}(kr)] \begin{matrix} \sin \\ \cos \end{matrix} m\phi \hat{i}_\phi \tag{4.8}$$

$\hat{i}_r$, $\hat{i}_\theta$ and $\hat{i}_\phi$ are the unit vectors in r, θ and ϕ directions,

$k = \omega\sqrt{\mu\varepsilon} = 2\pi/\lambda$ is the propagation constant ($k = k_o = \omega\sqrt{\mu_o\varepsilon_o}$ in region (1)), λ is the wavelength and

$a_{\substack{e \\ mn \\ o}}$ and $b_{\substack{e \\ mn \\ o}}$ are the unknown spherical wave coefficients of the incident field in region (1).

$c_{\substack{e \\ mn \\ o}}$ and $d_{\substack{e \\ mn \\ o}}$ are the unknown spherical wave coefficients of the scattered field in region (1).

e,o subscripts denote even and odd azimuthal (ϕ-coordinate) dependence, respectively.

n represents polar (θ-coordinate) wave order.

m represents azimuthal (ϕ-coordinate) wave order.

(i) subscript represents type of the radial propagation function.

$P_n^m(\cos\theta)$ is the associated Legendre function.

$z_n^{(i)}(kr)$ is the spherical Bessel function.

($z_n^{(1)}(kr) = j_n(kr)$, $z_n^{(2)}(kr) = y_n(kr)$, $z_n^{(3)}(kr) = h_n^{(1)}(kr)$ and $z_n^{(4)}(kr) = h_n^{(2)}(kr)$)

we select $z_n^{(1)}(kr) = j_n(kr)$ for the incident field to assure the field is finite at the origin (r=0). Also $z_n^{(4)}(kr) = h_n^{(2)}(kr)$ is chosen for the radial function of the scattered

field to satisfy the radiation condition on a sphere at infinity.

Let the total electromagnetic fields in region (2) be $\underline{E}_{(2)}$ and $\underline{H}_{(2)}$. We may expand these fields in terms of spherical wave functions in the form:

$$\underline{E}_{(2)} = -\sum_{n=1}^{N}\sum_{\substack{m=0\\e,o}}^{n}\left(e_{emn}\,\underline{m}_{d_{emn}}^{(1)} + f_{emn}\,\underline{n}_{d_{emn}}^{(1)}\right) \tag{4.9}$$

$$\underline{H}_{(2)} = \frac{k_d}{j\omega\mu_d}\sum_{n=1}^{N}\sum_{\substack{m=0\\e,o}}^{n}\left(e_{emn}\,\underline{n}_{d_{emn}}^{(1)} + f_{emn}\,\underline{m}_{d_{emn}}^{(1)}\right) \tag{4.10}$$

where, in region (2):

$k = k_d = \omega\sqrt{\mu_d\varepsilon_d} = 2\pi/\lambda_d$ and $\underline{m}_d^{(1)}$ and $\underline{n}_d^{(1)}$ are the appropriate spherical wave functions for this case and are given by Equations (4.7) and (4.8), respectively and upon replacing k by k_d.

4.3.2 The Boundary Conditions

The boundary conditions for this problem require that the tangential components of the total electric and magnetic fields be continuous on the surface of the dielectric sphere

(r=a) and can be expressed in mathematical form as:

$$\left.\begin{aligned} \hat{n} \times \underline{E}_{(1)} &= \hat{n} \times \underline{E}_{(2)} \\ \hat{n} \times \underline{H}_{(1)} &= \hat{n} \times \underline{H}_{(2)} \end{aligned}\right\} \quad \text{on } r=a \tag{4.11}$$

where $\hat{n}$ is the unit normal vector to the boundary of the sphere r=a in an outward direction.

From Equations (4.1) to (4.11), a relationship between the scattered field coefficients c_{mn}, d_{mn} in region (1) and the total field coefficients e_{mn}, f_{mn} in region (2) in terms of the unknown incident field coefficients a_{mn}, b_{mn} in region (1) can be determined. This relationship can be obtained by applying Equation (4.11) and using the known orthogonality relationships of the associated Legendre and trigonometric functions with respect to θ and ϕ. After tedious mathematical manipulation, one then obtains:

$$\begin{pmatrix} c^{e}_{mn} \\ d^{e}_{mn} \\ e^{e}_{mn} \\ f^{e}_{mn} \end{pmatrix}_{o} = \begin{pmatrix} C_n & & & \\ & D_n & 0 & \\ & & E_n & \\ & 0 & & F_n \end{pmatrix} \begin{pmatrix} a^{e}_{mn} \\ b^{e}_{mn} \\ a^{e}_{mn} \\ b^{e}_{mn} \end{pmatrix}_{o} \tag{4.12}$$

$m=0,1,2,\ldots,n$
$n=1,2,\ldots,N$

where:

$$C_n = \frac{-\sqrt{\frac{\varepsilon_r}{\mu_r}}\,\hat{J}_n(k_o a)\,\hat{J}_n'(k_d a) + \hat{J}_n(k_d a)\,\hat{J}_n'(k_o a)}{\sqrt{\frac{\varepsilon_r}{\mu_r}}\,\hat{H}_n^{(2)}(k_o a)\,\hat{J}_n'(k_d a) - \hat{H}_n^{(2)'}(k_o a)\,\hat{J}_n(k_d a)}$$

$$D_n = \frac{-\sqrt{\frac{\varepsilon_r}{\mu_r}}\,\hat{J}_n(k_d a)\,\hat{J}_n'(k_o a) + \hat{J}_n(k_o a)\,\hat{J}_n'(k_d a)}{\sqrt{\frac{\varepsilon_r}{\mu_r}}\,\hat{J}_n(k_d a)\,\hat{H}_n^{(2)'}(k_o a) - \hat{H}_n^{(2)}(k_o a)\,\hat{J}_n'(k_d a)}$$

$$E_n = \frac{j\sqrt{\varepsilon_r \mu_r}}{\sqrt{\frac{\varepsilon_r}{\mu_r}}\,\hat{J}_n'(k_d a)\,\hat{H}_n^{(2)}(k_o a) - \hat{J}_n(k_d a)\,\hat{H}_n^{(2)'}(k_o a)} \qquad (4.13)$$

$$F_n = \frac{-j\sqrt{\varepsilon_r \mu_r}}{\sqrt{\frac{\varepsilon_r}{\mu_r}}\,\hat{J}_n(k_d a)\,\hat{H}_n^{(2)'}(k_o a) - \hat{J}_n'(k_d a)\,\hat{H}_n^{(2)}(k_0 a)}$$

and

$$\hat{Z}_n(kr) = kr\, z_n(kr) = \sqrt{\frac{\pi kr}{2}}\, Z_{n+\frac{1}{2}}(kr)$$

is the Riccati type spherical Bessel function [21].

Now, by substituting the results of Equation (4.12) into Equation (4.1), one can obtain the tangential components of the total electric field in region (1) ($a \leq r \leq b$) in the form:

$$E_\theta(r,\theta,\phi) = - E_o \sum_{n=1}^{N} \sum_{\substack{m=0 \\ e,o}}^{n} \{ \mp a_{mn}^{e}_{o} [\hat{J}_n(k_o r) + C_n \hat{H}_n^{(2)}(k_o r)]$$

$$\frac{mP_n^m(\cos\theta)}{\sin\theta} \cdot \begin{matrix}\sin \\ \cos\end{matrix}(m\phi) + b_{mn}^{e}_{o} [\hat{J}'_n(k_o r) + D_n \hat{H}_n^{(2)'}(k_o r)]$$

$$\frac{\partial P_n^m(\cos\theta)}{\partial\theta} \begin{matrix}\cos \\ \sin\end{matrix}(m\phi)\} \qquad (4.14)$$

and

$$E_\phi(r,\theta,\phi) = E_o \sum_{n=1}^{N} \sum_{\substack{m=0 \\ e,o}}^{n} \{a_{mn}^{e}_{o} [\hat{J}_n(k_o r) + C_n \hat{H}_n^{(2)}(k_o r)]$$

$$\frac{\partial P_n^m(\cos\theta)}{\partial\theta} \begin{matrix}\cos \\ \sin\end{matrix}(m\phi)$$

$$\pm b_{mn}^{e}_{o} [\hat{J}'_n(k_o r) + D_n \hat{H}_n^{(2)'}(k_o r)] \frac{mP_n^m(\cos\theta)}{\sin\theta} \begin{matrix}\sin \\ \cos\end{matrix}(m\phi)\} \qquad (4.15)$$

where $E_o = \frac{1}{k_o r}$.

4.3.3 Calculation of the Incident Field Coefficients $a_{\substack{e\\o}mn}$ and $b_{\substack{e\\o}mn}$

To calculate the incident field coefficients $a_{\substack{e\\o}mn}$ and $b_{\substack{e\\o}mn}$, one can use Equations (4.14) and (4.15) and the orthogonality of the trigonometric functions with respect to ϕ in region (1). On the surface of the measurement sphere of radius r=A ($a \leq A \leq b$), the Riccati-spherical Bessel functions and their derivatives are constant. The orthogonality relationship with respect to ϕ will separate the coefficients of different m. This can be achieved by rotating the test antenna and using the measurement data to carry out the orthogonality integrals with an on-line computer. Alternatively, it may be achieved by measuring data over circles of constant θ and evaluating the orthogonality integrals numerically by utilizing the measurement data. In this manner the relationships between coefficients can be reduced to a set of relationships for fixed m indices. For each fixed m, the coefficients a_{emn} and b_{omn} (n=m, m+1,..., N+m-1) can then be determined by solving 2N linear algebraic equations.

To be specific, on the surface of the measurement sphere r=A ($a \leq A \leq b$), the field components using Equations (4.14) and (4.15) may be written in the form:

$$E_\theta(A,\theta,\phi) = -\sum_{n=1}^{N} \{B_{eon} \frac{\partial P_n}{\partial \theta} + \sum_{\substack{m=1 \\ e,o}}^{n} [\mp A_{\substack{e \\ mn \\ o}} \frac{mP_n^m}{\sin\theta} \sin_{\cos} m\phi$$

$$+ B_{\substack{e \\ mn \\ o}} \frac{\partial P_n^m}{\partial \theta} \cos_{\sin} m\phi]\} \qquad (4.16)$$

and

$$E_\phi(A,\theta,\phi) = \sum_{n=1}^{N} \{A_{eon} \frac{\partial P_n}{\partial \theta} + \sum_{\substack{m=1 \\ e,o}}^{n} [A_{\substack{e \\ mn \\ o}} \frac{\partial P_n^m}{\partial \theta} \cos_{\sin} m\phi$$

$$\pm B_{\substack{e \\ mn \\ o}} \frac{mP_n^m}{\sin\theta} \sin_{\cos} m\phi]\} \qquad (4.17)$$

where

$$A_{\substack{e \\ mn \\ o}} = E_o \, a_{\substack{e \\ mn \\ o}} [\hat{J}_n(k_o A) + C_n \hat{H}_n^{(2)}(k_o A)] \, ,$$

$$B_{\substack{e \\ mn \\ o}} = E_o \, b_{\substack{e \\ mn \\ o}} [\hat{J}_n'(k_o A) + D_n \hat{H}_n^{(2)'}(k_o A)] \qquad (4.18)$$

and

$$A_{oOn} = 0, \; B_{oOn} = 0, \quad E_o = \frac{1}{k_o A} \quad .$$

Here $A_{\substack{e \\ mn \\ o}}$ and $B_{\substack{e \\ mn \\ o}}$ are constants on the measurement sphere surface r=A. Integrating Equations (4.16) and (4.17) and using the orthogonality relationship with

respect to ϕ at a fixed m, one can define the following functions

For m=0:

$$I_{o\theta}(\theta) = -\frac{1}{2\pi}\int_{o}^{2\pi} E_{\theta}(A,\theta,\phi)d\phi = \sum_{n=1}^{N} B_{eon}\frac{\partial P_n}{\partial\theta}$$

and

$$I_{o\phi}(\theta) = \frac{1}{2\pi}\int_{o}^{2\pi} E_{\phi}(A,\theta,\phi)d\phi = \sum_{n=1}^{N} A_{eon}\frac{\partial P_n}{\partial\theta} \qquad (4.19)$$

For $m\geq 1$:

$$\left.\begin{aligned} I_{m\theta}(\theta) &= \frac{1}{\pi}\int_{o}^{2\pi} E_{\theta}(A,\theta,\phi)\ \sin m\phi d\phi \\ &= \sum_{n=m}^{N+m-1}\left[A_{emn}\frac{mP_n^m}{\sin\theta} - B_{omn}\frac{\partial P_n^m}{\partial\theta}\right] \end{aligned}\right\} \qquad (4.20)$$

and

$$\left.\begin{aligned} I_{m\phi}(\theta) &= \frac{1}{\pi}\int_{o}^{2\pi} E_{\phi}(A,\theta,\phi)\ \cos m\phi d\phi \\ &= \sum_{n=m}^{N+m-1}\left[A_{emn}\frac{\partial P_n^m}{\partial\theta} - B_{omn}\frac{mP_n^m}{\sin\theta}\right] . \end{aligned}\right\}$$

In Equations (4.20), there are 2N unknowns. The integrals $I_{m\theta}(\theta_i)$ and $I_{m\phi}(\theta_i)$ can be evaluated by carrying out measurements at $\theta=\theta_i$, i=1,2,...,N and rotating the test antenna around the z-axis, 360 degrees at each measurement point of θ. One can then form a system of linear algebraic equations in 2N unknowns for each given value of $m \geq 1$, in the form:

$$[S] \begin{bmatrix} [A_{emn}] \\ -[B_{omn}] \end{bmatrix} = \begin{bmatrix} [I_{m\theta}(\theta)] \\ [I_{m\phi}(\theta)] \end{bmatrix} \tag{4.21}$$

where

$[I_{m\theta}(\theta)]$ and $[I_{m\phi}(\theta)]$ are known column vectors of N elements each whose transposes are equal to:

$$[I_{m\theta}(\theta)]^t = [I_{m\theta}(\theta_1),\ I_{m\theta}(\theta_2),\ \ldots,\ I_{m\theta}(\theta_N)]$$

and

$$[I_{m\phi}(\theta)]^t = [I_{m\phi}(\theta_1),\ I_{m\phi}(\theta_2),\ \ldots,\ I_{m\phi}(\theta_N)] .$$

The unknown coefficients a_{emn} and b_{omn} are included in the vectors $[A_{emn}]$ and $[B_{omn}]$ and their transposes are:

$$[A_{emn}]^t = [A_{em,m},\ A_{em,m+1},\ \ldots,\ A_{em,N+m-1}]$$

and

$$[B_{omn}]^t = [B_{om,m},\ B_{om,m+1},\ \ldots.,\ B_{om,N+m-1}] .$$

The matrix [S] is a 2Nx2N matrix, and can be written in the form:

$$[S] = \begin{bmatrix} [S_1] & [S_2] \\ [S_2] & [S_1] \end{bmatrix} \tag{4.22}$$

in which $[S_1]$ and $[S_2]$ are NxN matrices, and their elements are:

$$\left.\begin{aligned} s_{1ij} &= \left.\frac{mP_n^m(\cos\theta_i)}{\sin\theta_i}\right|_{n=j+m-1} = \frac{mP^m_{j+m-1}(\cos\theta_i)}{\sin\theta_i} \\ \text{and} \\ s_{2ij} &= \left.\frac{\partial P_n^m(\cos\theta)}{\partial\theta}\right|_{\substack{\theta=\theta_i \\ n=j+m-1}} = \left.\frac{\partial P^m_{j+m-1}(\cos\theta)}{\partial\theta}\right|_{\theta=\theta_i}. \end{aligned}\right\} \tag{4.23}$$

In a similar manner, a similar algebraic system of linear equations can be constructed as Equation (4.21) to calculate the other half of the coefficients:

$$[S]\begin{bmatrix} [A_{omn}] \\ [B_{emn}] \end{bmatrix} = \begin{bmatrix} [I'_{m\theta}(\theta)] \\ [I'_{m\phi}(\theta)] \end{bmatrix} \tag{4.24}$$

where

$$I'_{m\theta}(\theta) = -\frac{1}{\pi}\int_0^{2\pi} E_\theta(A,\theta,\phi)\,\cos m\phi\, d\phi \quad ,$$

$$I'_{m\phi}(\theta) = \frac{1}{\pi}\int_0^{2\pi} E_\phi(A,\theta,\phi)\,\sin m\phi\, d\phi$$

and [S] is the same matrix as given in Equations (4.22), and (4.23).

Solving Equations (4.21) and (4.24) which require only a single inversion of the matrix [S], the unknown coefficients $[A^{e}_{mn}]_o$ and $[B^{e}_{mn}]_o$ can be calculated. Their results can be used in Equation (4.18) to evaluate the coefficients of the incident field $[a^{e}_{mn}]_o$ and $[b^{e}_{mn}]_o$ for $m \geq 1$.

In the case of m=0, Equation (4.19) gives

$$\begin{bmatrix} [0] & [S_2(m=0)] \\ [S_2(m=0)] & [0] \end{bmatrix} \begin{bmatrix} [A_{eon}] \\ [B_{eon}] \end{bmatrix} = \begin{bmatrix} [I_{o\theta}(\theta)] \\ [I_{o\phi}(\theta)] \end{bmatrix} \qquad (4.25)$$

from which, the coefficients $[A_{eon}]$, $[B_{eon}]$ and hence $[a_{eon}]$, $[b_{eon}]$ can be calculated.

4.3.4 Optimum Distribution of Measurement Points

The inversion of the matrix [S] which appeared in Equations (4.21) and (4.24) for $m \geq 1$ has been studied previously in detail [43]. It was shown there that, the most stable inversion of the matrix [S] can be done, if the measurement points are located at the roots of the following optimization function:

$$O_N^m = \frac{1}{(1-y_r^2)^{\frac{m-1}{2}}} \; P_{N+m-1}^{m-1}(y_r) \tag{4.26}$$

where:

$$y_r = \frac{\cos\theta_r - \left(\frac{\cos\theta_a + \cos\theta_b}{2}\right)}{\left|\frac{\cos\theta_a - \cos\theta_b}{2}\right|} \; .$$

The angles θ_a and θ_b are the limiting computational aspect angles, and: $\theta_r (r=1,2,\ldots,N)$ are the location of the measurement points such that $\theta_a \leq \theta_1 < \theta_2 < \ldots < \theta_N \leq \theta_b$. Here N is the number of measurement points in the θ-direction, m is the azimuthal dependence, and $P_{N1}^M(y_r)$ is the associated Legendre polynomial of the first kind of order $M=m-1$ and degree $N1=N+m-1$. The roots of Equation (4.26) are symmetric around $y_r=0$.

The limiting computational aspect angles θ_a and θ_b can

be given a priori as a limiting case of the measurement locations sector of θ. In the case they are not known, they may be estimated from [43]:

$$\left|\frac{\cos\theta_a - \cos\theta_b}{2}\right| = \frac{\cos\theta_1 - \cos\theta_N}{2y_1} \quad \text{and}$$

$$\left|\frac{\cos\theta_a + \cos\theta_b}{2}\right| = \frac{\cos\theta_1 + \cos\theta_N}{2} \quad . \tag{4.27}$$

The only condition for calculating θ_a and θ_b using Equation (4.27) as mentioned in [43] is to maintain:

$$\left|\frac{\cos\theta_1 - \cos\theta_N}{2y_1}\right| \leq 1 \quad . \tag{4.28}$$

The reason for using the optimum distributions of the measurement aspect angle θ as in Equation (4.26) is that the determinant of the matrix S in Equation (4.22) will be maximum at these points, which assures the most stable inversion of the matrix S [43].

4.4 CALCULATION OF THE FAR-FIELD RADIATION PATTERN OF AN ANTENNA

The far-field radiation pattern of an antenna is one of its most important characteristics. The field pattern is actually a three-dimensional or space pattern, and its complete description requires field intensity measurements in all directions in space [44].

There are several problems in which an electromagnetic field is known on a surface, and it is desired to determine the field elsewhere. A common example is when the field is specified over an antenna aperture or other "near-field" surfaces, and it is desired to determine the far-field radiation patterns [33]. There are two techniques for accomplishing the transformation of field data from one surface to another [33]:

(1) Representing the field at an arbitrary point as an integral over the surface on which the fields are known (Huygens-Fresnel principle) [18]; and,

(2) Representing the field at an arbitrary point as a summation of free-space "modes" where the mode coefficients are determined by matching the fields on the surface on which the fields are known.

In the last case the modes may be any set of functions which

form a basis for wave solutions to Maxwell's equations. In this section, only the spherical wave functions will be used.

The problem now is, how to calculate the antenna far-field radiation pattern if the field is known on a closed surface S which encloses the antenna, as shown in Fig. 4.4. This problem is well known and is solved by many authors [18], [29], [33], [34], ... etc., and its solution will be summarized here for use in the next chapter.

4.4.1 The Huygens-Fresnel Principle

For aperture antennas, the Huygens-Fresnel principle was utilized to form an equivalent source from the aperture field distributions. Reference [18] has shown that, the complete electric field $\underline{E}$ and magnetic field $\underline{H}$ within a given volume can be expressed in terms of the current densities of the sources within the volume and the values of the field over the boundaries of the volume. If the volume of interest V_1 contains no sources and is bounded by a closed surface S and a sphere at infinity (the region outside the volume V in Fig. 4.4), the $\underline{E}$ and $\underline{H}$ fields at a point P within the volume V_1 are given by Equations (2.1) and (2.2). These equations require the tangential and the normal components of the electromagnetic field on the surface S.

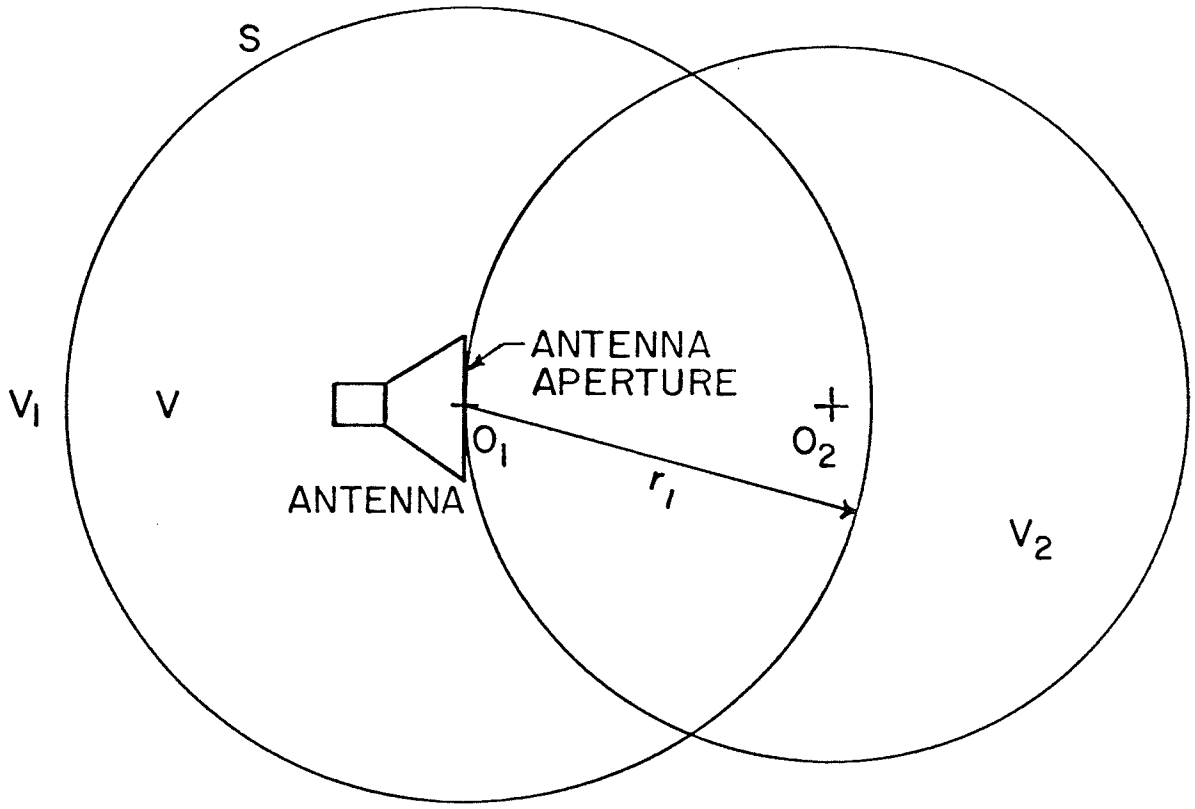

Fig. 4.4: A cross-section showing the test antenna, a closed surface S enclosing the antenna.

From a practical point of view, for the aperture-type antennas, e.g., reflectors, horns, etc., it is desirable to calculate the far-field radiation pattern only from the fields in front of the antenna aperture. This means that a knowledge of the electromagnetic near-field on part of the surface S in front of the antenna or in the aperture plane of the antenna is sufficient to calculate the approximate radiation pattern by using the Huygens-Fresnel principle. The theory of this chapter can be used to calculate the electromagnetic near-field required on the aperture of the antenna by calculating the electromagnetic field inside a region V_2 as shown in Fig. 4.4. Inside V_2, the electromagnetic field on any appropriate aperture plane in front of the antenna can be known, since it is inside this region. But if it is desired to calculate the radiation pattern in the whole space, then, the near-field on the whole surface S must be known. This is also feasible by using the stepwise technique described by section 4.2. That is, by measuring the field over a sphere enclosing V_2 and centered at O_2, the electromagnetic field of the antenna can be known completely inside the region V_2 surrounding O_2 and tangent to the antenna. Thus, the near-field on part of the surface S which lies inside the region V_2 can be determined. Repeating this process, i.e., measuring the field over several spheres around the antenna, the field expansions inside each sphere can be determined. From which,

the field over those portions of S which lies within each sphere can be determined. In this manner the field of the antenna everywhere, over the surface S, enclosing the antenna can be determined from which the far-field can be evaluated.

4.4.2 Calculation of the Far-Field Antenna Pattern Using Spherical Wave Functions

Here the electromagnetic field in the region V_1 (outside V) can be expanded in terms of the appropriate spherical wave functions as in section 4.3. In this case $\underline{m}^{(4)}$ and $\underline{n}^{(4)}$ can be chosen as the appropriate vector wave functions which contain the spherical Hankel function $h^{(2)}(k_o r)$ and its derivatives as a radial function, which satisfy the radiation condition at infinity. The unknown coefficients of the spherical wave functions expansions may be evaluated by matching the fields on the surface S, on which the fields are known. The matrix method of section 4.3 can be used to calculate these coefficients. On the other hand, the integration method which is used by [29] and [34] can also be used. In the latter method, the unknown coefficients of the incident electromagnetic fields in region V_1 for outgoing waves are given by the following formulas [34]:

$$a_{\substack{e \\ mn \\ o}} = \frac{1}{\gamma_{mn} V_n^{*}(k_o r_1)} \int_0^{2\pi} \int_0^{\pi} \underline{n}^{(3)}_{\substack{e \\ mn \\ o}} (r_1,\theta,\phi) \times \underline{E}(r_1,\theta,\phi) \cdot \hat{i}_r \sin\theta d\theta d\phi \quad . \tag{4.29}$$

and

$$b_{\substack{e\\mn\\o}} = \frac{-1}{\gamma_{mn} V_n(k_o r_1)} \int_0^{2\pi} \int_0^{\pi} \underline{m}^{(3)}_{\substack{e\\mn\\o}}(r_1,\theta,\phi) \times \underline{E}(r_1,\theta,\phi) \cdot \hat{i}_r \sin\theta d\theta d\phi \qquad (4.30)$$

where

$a_{\substack{e\\mn\\o}}$ and $b_{\substack{e\\mn\\o}}$ are the unknown coefficients of the spherical wave functions expansion of the electromagnetic field given by Equations (4.3) and (4.4) using the appropriate spherical wave functions $\underline{m}^{(4)}$ and $\underline{n}^{(4)}$.

$\underline{E}(r_1,\theta,\phi)$ is the electric near-field which is known on the surface S of the sphere V of radius $r=r_1$.

$\underline{m}^{(3)}(r_1,\theta,\phi)$ and $\underline{n}^{(3)}(r_1,\theta,\phi)$ are the spherical wave functions at $r=r_1$ given by Equations (4.7) and (4.8) using the radial function $z_n^{(i)}(k_o r_1) = h_n^{(1)}(k_o r_1)$, where $h_n^{(1)}(k_o r_1)$ is the spherical Hankel function of the first kind.

$$V_n(k_o r) = h_n^{(1)}(k_o r) \frac{1}{k_o r} \frac{\partial}{\partial r} [r h_n^{(2)}(k_o r)] \qquad (4.31)$$

$$V_n^*(k_o r) = \text{complex conjugate of } V_n(k_o r)$$
$$= h_n^{(2)}(k_o r) \frac{1}{k_o r} \frac{\partial}{\partial r} [r h_n^{(1)}(k_o r)] \qquad (4.32)$$

and

$$\gamma_{mn} = 2\pi\varepsilon_m \frac{n(n+1)}{2n+1} \frac{(n+m)!}{(n-m)!}, \quad \varepsilon_m = \begin{cases} 2 & \text{for } m=0 \\ 1 & \text{for } m\neq 0 \end{cases} . \tag{4.33}$$

Once the coefficients $a^{e}_{mn_o}$ and $b^{e}_{mn_o}$ are known, the electromagnetic field in the region V_1 can be calcalculated. The far-field radiation pattern of the antenna can then be evaluated by using the following asymptotic formulas of the spherical Hankel functions [45]:

$$\lim_{r\to\infty} h_n^{(2)}(k_o r) \simeq j^{n+1} \frac{e^{-jk_o r}}{k_o r} \tag{4.34}$$

and

$$\lim_{r\to\infty} \frac{1}{k_o r} \frac{\partial}{\partial r} [r h_n^{(2)}(k_o r)] \simeq j^n \frac{e^{-jk_o r}}{k_o r} . \tag{4.35}$$

Formulas similar to that of Equations (4.29) and (4.30) but using the magnetic field $\underline{H}$, instead of the electric field $\underline{E}$, can also be used provided that $\underline{H}$ is known. These formulas are given in reference [34].

4.5 DISCUSSIONS

In this chapter, the theory of the inverse source problem in the three-dimensional case was presented. The

problem consisted of using a dielectric scatterer (sphere) in front of the antenna whose radiation field is unknown. It was required to calculate the far radiation pattern of the isolated antenna, or, that of the antenna in the presence of the scatterer from measurements of the total field in the near-field region of the antenna. When the spherical surface S enclosing both sphere and the antenna, as shown in Fig. 4.1, is small in size the measurement can be carried out over this surface to obtain the total field. In addition, the field outside S can be described by spherical wave functions with unknown coefficients. These unknown coefficients can then be obtained by matching the measured and the spherical wave expansion fields over the spherical surface S. On the other hand, when the antenna, or its separation distance from the scattering sphere is large, the spherical surface enclosing them also becomes large. The measurement of the field over such a large surface requires large scanning systems, which in practice is undesirable. To utilize a small scanning system, the stepwise measurement technique was proposed and presented in section 4.2. This technique is also discussed elsewhere [46]. The method of analysis and solution of this problem was also presented. The calculation of the far-field radiation pattern using this technique was summarized.

It can be concluded that from a theoretical point of view, the technique of the field measurement using scattering data is feasible in the three-dimensional case as was in the two-dimensional problem of chapter three.

CHAPTER V

THREE-DIMENSIONAL INVERSE SOURCE PROBLEM, APPLICATIONS AND NUMERICAL INVESTIGATIONS

5.1 INTRODUCTION

In this chapter, the application of the field measurement using scattering data technique, which was discussed in chapter four will be investigated numerically. For the radiation source three different cases are considered; a plane wave, an electric dipole and a four-element electric dipole array. Considering any of these sources the field scattered by a specified dielectric sphere is obtained analytically and is used together with the incident field to generate numerically the measurement data over specified measurement spheres. These measurement data are then used to obtain the field expansion coefficients within each expansion sphere. The calculated expansion coefficients are then used to reconstruct the initial source field. For various geometrical and expansion sphere number and radius, the computational errors are computed and the accuracy of the reconstructed fields are then studied in detail. The numerical results of this chapter are obtained by using computer programs specifically prepared for this purpose [41].

5.2 PLANE WAVE CASE

An incident plane wave propagating in the positive z-direction and polarized in the x-direction is selected here to examine the theory of the field measurement using scattering data technique of chapter four. The electric and the magnetic fields of the incident plane wave are:

$$\left.\begin{aligned} \underline{E}^i &= \hat{i}_x \, E_o \, e^{-jk_o z} \\ \text{and} \\ \underline{H}^i &= \hat{i}_y \, \frac{E_o}{\eta} \, e^{-jk_o z} \end{aligned}\right\} \qquad (5.1)$$

where $\hat{i}_x$ and $\hat{i}_y$ are the unit vectors in the x and y directions, k_o and η are the propagation constant and the intrinsic impedance of free space, respectively. The unit vectors $\hat{i}_x$ and $\hat{i}_y$ can be written in terms of unit vectors of spherical coordinate system $\hat{i}_r$, $\hat{i}_\theta$ and $\hat{i}_\phi$ as:

$$\left.\begin{aligned} \hat{i}_x &= \sin\theta\cos\phi\hat{i}_r + \cos\theta\cos\phi\hat{i}_\theta - \sin\phi\hat{i}_\phi \\ \text{and} \\ \hat{i}_y &= \sin\theta\sin\phi\hat{i}_r + \cos\theta\sin\phi\hat{i}_\theta + \cos\phi\hat{i}\phi \end{aligned}\right\} \quad . \qquad (5.2)$$

The incident electromagnetic fields can be expanded in terms of the spherical vector functions $\underline{m}$ and $\underline{n}$ given by Equations

(4.3) and (4.4). At r=0, the field is finite and we therefore select spherical Bessel functions of the first kind as the radial functions. Moreover, the dependence of Equation (5.2) on ϕ is limited to m=1. Hence considering the odd and even properties of Equations (4.7) and (4.8), we assume the expansion functions in the form:

$$\left.\begin{aligned} \underline{E}^i &= -\sum_{n=1}^{\infty} \left(a_n \underline{m}_{o1n}^{(1)} + b_n \underline{n}_{e1n}^{(1)}\right) \\ \text{and} \\ \underline{H}^i &= +\frac{k_o}{j\omega\mu_o} \sum_{n=1}^{\infty} \left(a_n \underline{n}_{o1n}^{(1)} + b_n \underline{m}_{e1n}^{(1)}\right) \end{aligned}\right\} \qquad (5.3)$$

where a_n and b_n are the unknown coefficients of the incident field yet to be determined. However, for a plane wave, these coefficients are given in [21] and [37] and are of the form:

$$\left.\begin{aligned} a_n &= \frac{j^{-n}(2n+1)}{n(n+1)} \\ \text{and} \\ b_n &= ja_n = \frac{j^{-n+1}(2n+1)}{n(n+1)} \end{aligned}\right\} \quad . \qquad (5.4)$$

In Equations (5.1), E_o is considered to be unity.

The problem under considertion is to select the expansion of Equations (5.3) with unknown coefficients

and determine them by using the theory of the previous chapter. The scatterer is a dielectric sphere of radius $k_0 a=1.0$, with a relative permittivity $\varepsilon_r=4.0$ and a relative permeability $\mu_r=1.0$. Because, this problem is a simple one, measurement data are generated only over a single measurement sphere, enclosing the dielectric one, and having a radius of $k_0 A=3.0$. The scattering of a plane wave by a dielectric sphere is well known. Thus, the measurement data over the measurement sphere can be obtained readily by adding the known incident field to the scattering one. These generated data are then used together with boundary conditions of Equations (4.11) and (4.13) to determine the expansion coefficients of the incident field. Finally, these expansion coefficients are used in Equations (5.3) to calculate the incident field.

Note that, since only m=1 modes are present, the required expansion coefficients can be obtained by using the measurement data in only $\phi=0$ and $\phi=\frac{\pi}{2}$ planes. Also, if N terms in the expansions are retained, only N matching points in the θ-direction will be necessary to determine the unknown coefficients. These N points are selected at optimum locations which are determined using Equation (4.26). For several different values of N, the reconstructed E_θ- and E_ϕ-components of the incident field are compared with the exact ones in Figs. 5.1 to 5.4. For this particular problem, the reconstructed

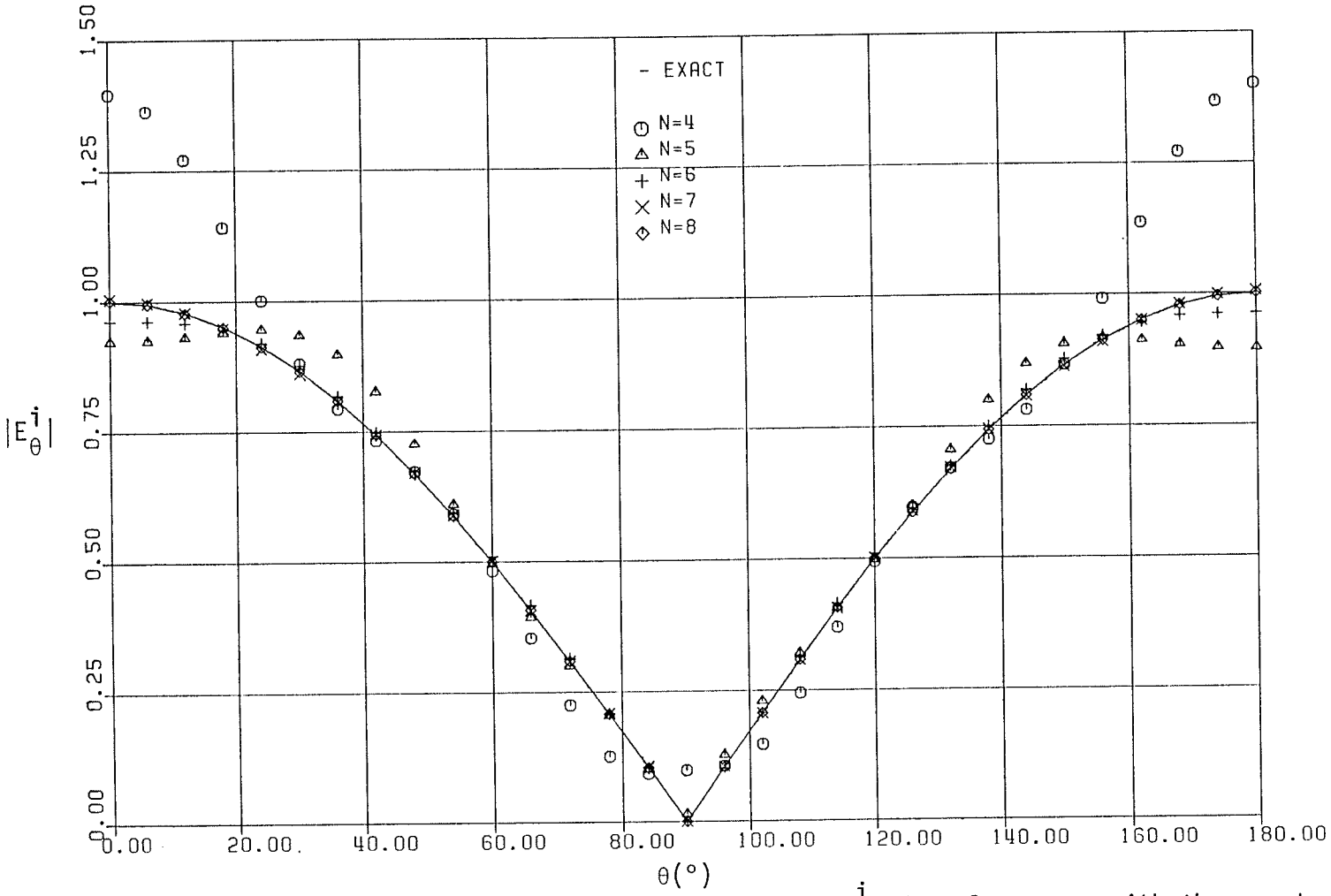

Fig. 5.1: Comparison of the reconstructed amplitude of E_θ^i of a plane wave with the exact one, $k_o r_1 = 3.0$.

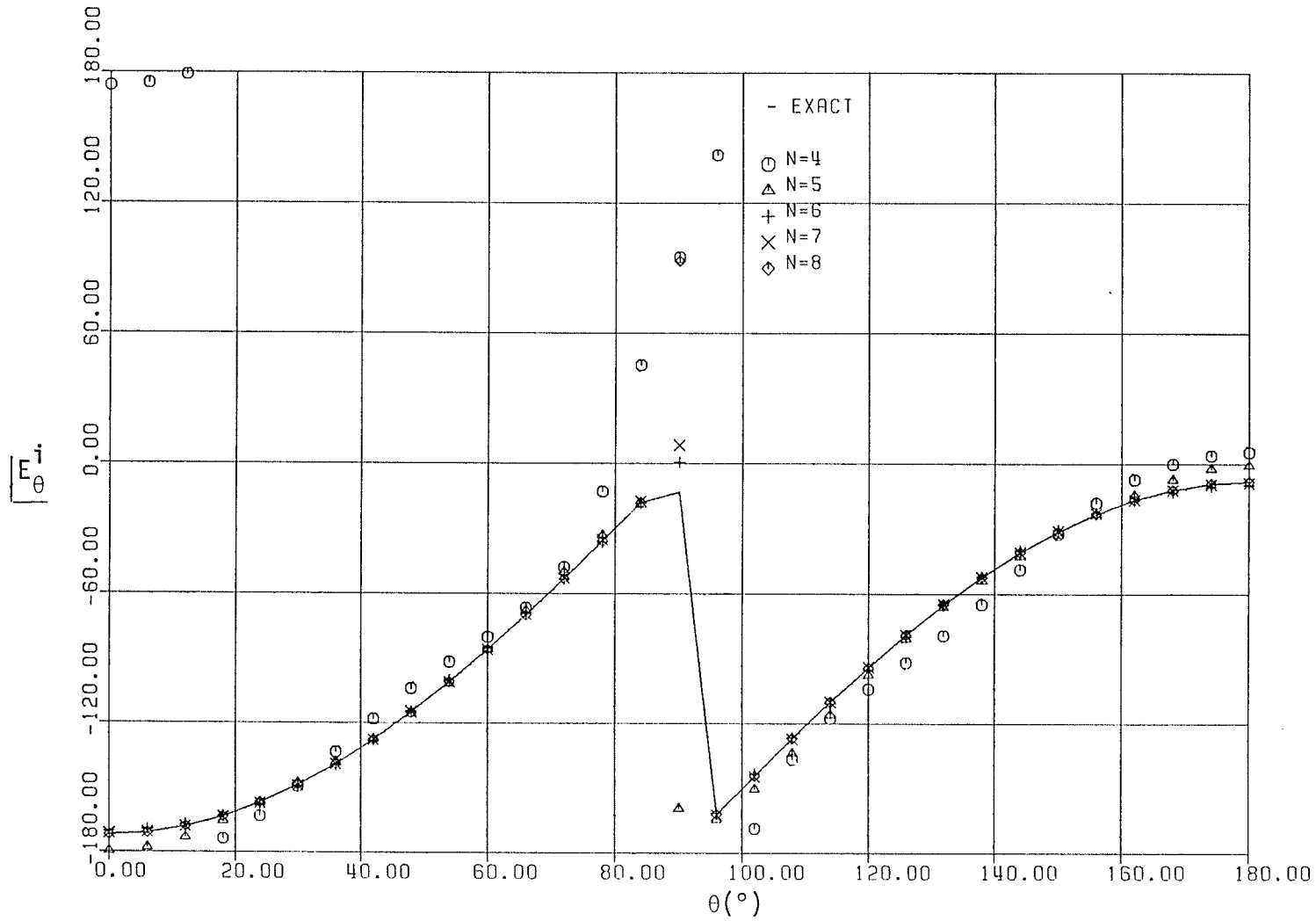

Fig. 5.2: Comparison of the reconstructed phase of E_θ^i of a plane wave with the exact one, $k_o r_1 = 3.0$.

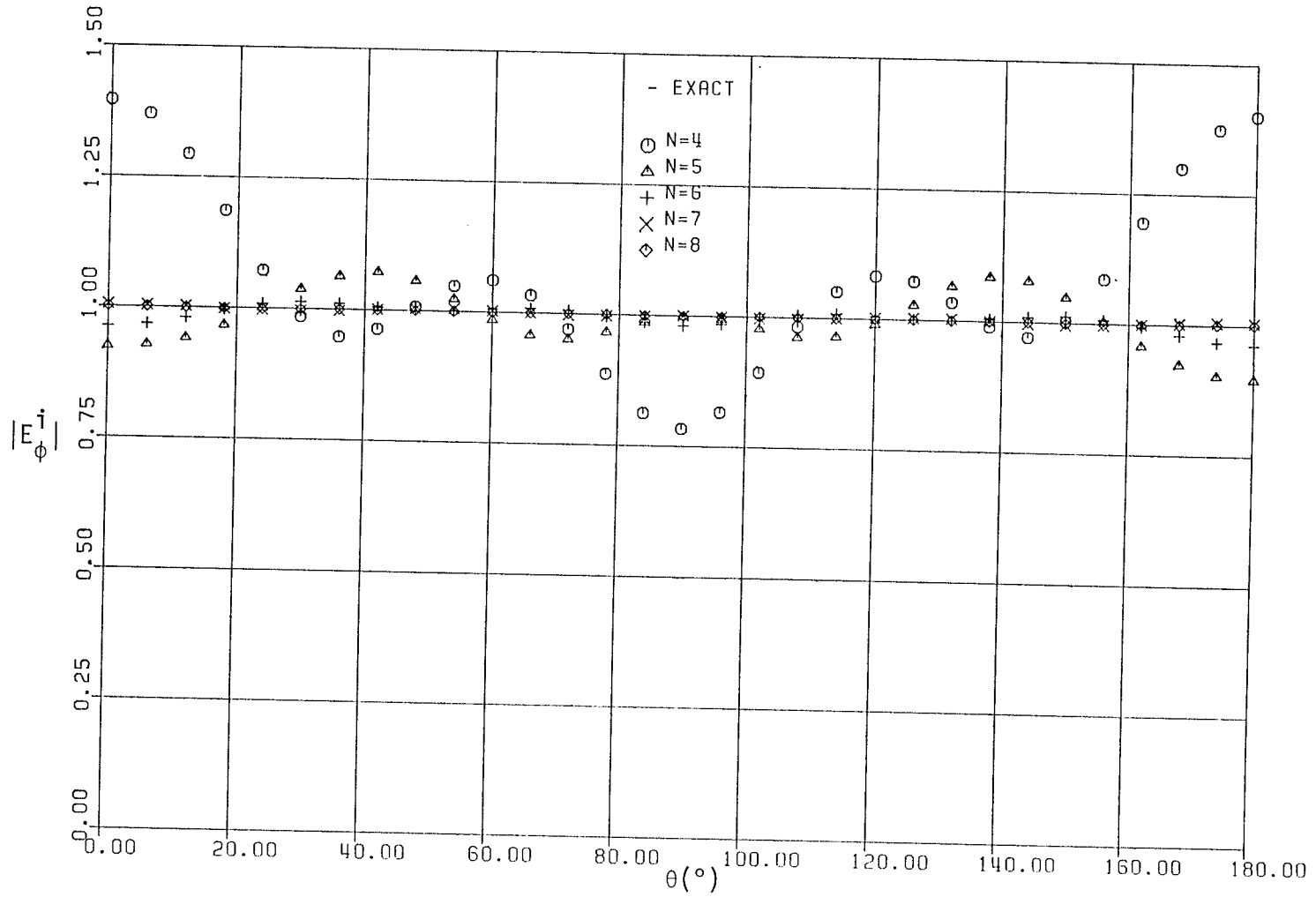

Fig. 5.3: Comparison of the reconstructed amplitude of E_ϕ^i of a plane wave with the exact one, $k_o r_1 = 3.0$.

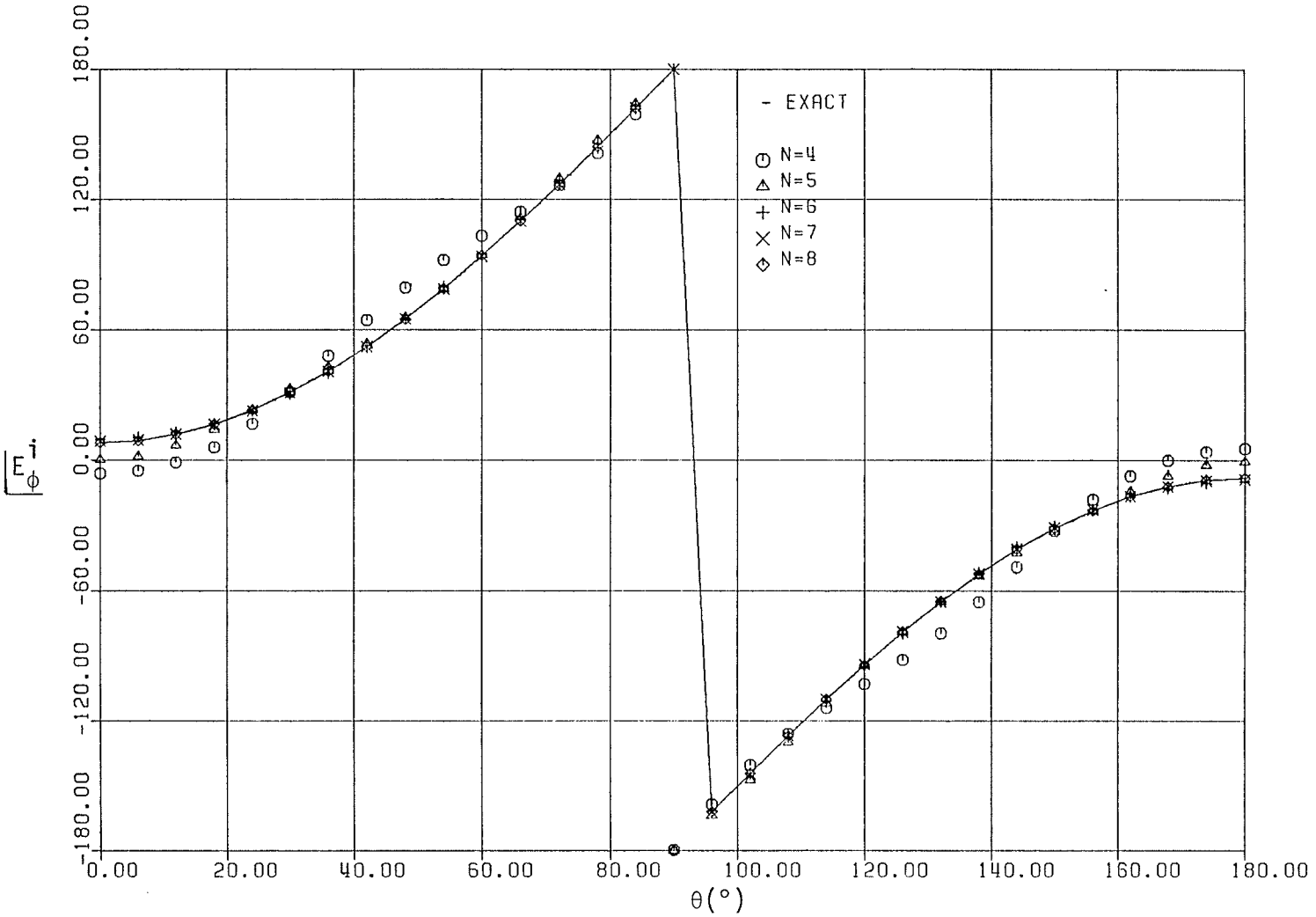

Fig. 5.4: Comparison of the reconstructed phase of E_ϕ^i of a plane wave with the exact one, $k_o r_1 = 3.0$.

fields for N>7 agree well with the exact ones, with an accuracy better than 0.01%.

5.3 ELECTRIC DIPOLE CASE

5.3.1 The Exact Solution

With reference to Fig. 5.5 consider an incident wave from an x-directed electric dipole which lies on the z-axis at a distance z_o from the origin O (center of the dielectric sphere). The exact field of this source is known and is given in [21]. The incident electric and magnetic fields $\underline{E}$ and $\underline{H}$ in terms of the magnetic vector potential $\underline{A}$ are in the form [21]:

$$\underline{E} = - j\omega\mu_o\underline{A} + \frac{1}{j\omega\varepsilon_o} \nabla (\nabla\cdot\underline{A}) \tag{5.5}$$

and

$$\underline{H} = \nabla x\underline{A} \tag{5.6}$$

where ω is the angular frequency rad./sec, μ_o is the free space permeability, and ε_o is the free space permittivity. For a current element $I\underline{\ell}$, the vector potential $\underline{A}$ is given by [21]:

$$\underline{A} = \frac{I\underline{\ell}\ e^{-jk_o|\underline{r}-\underline{r}'|}}{4\pi|\underline{r}-\underline{r}'|} \tag{5.7}$$

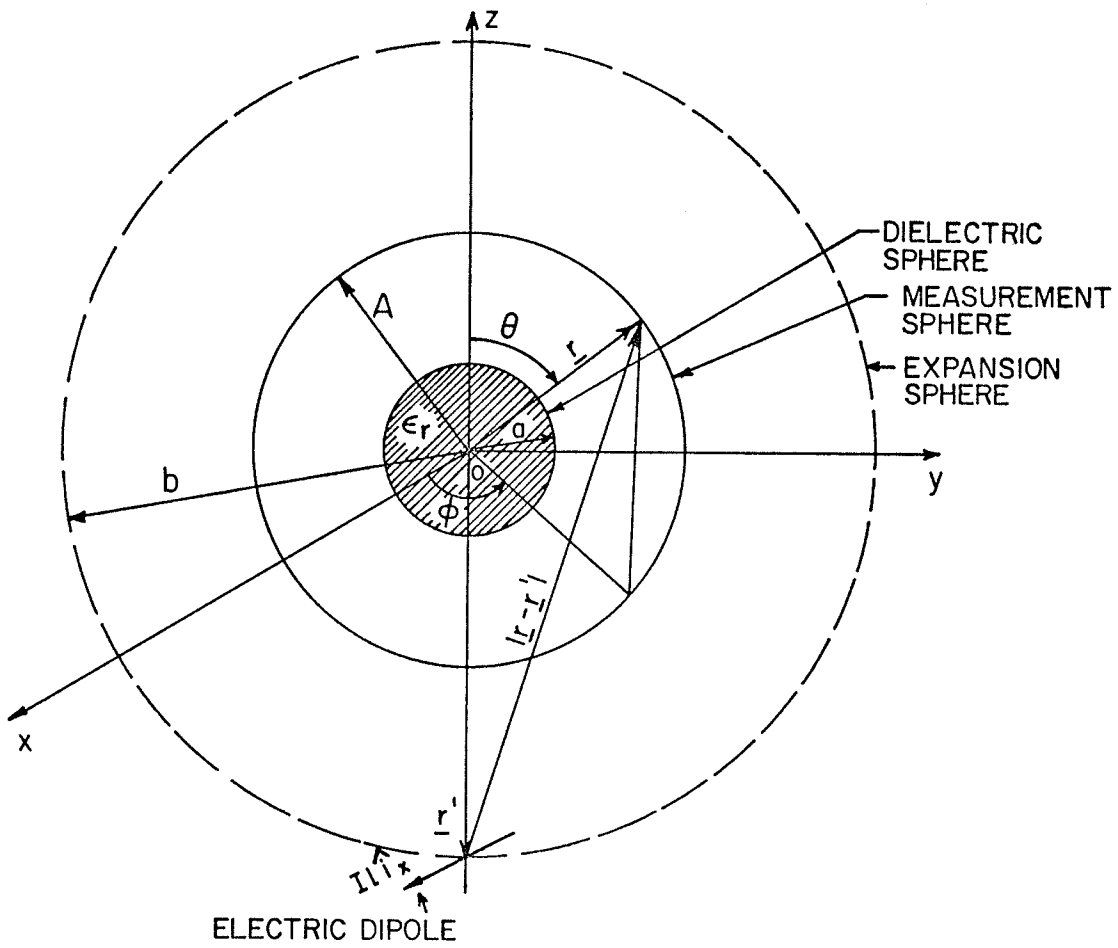

Fig. 5.5: Geometry of measurement and expansion spheres for an x-directed electric dipole, near a dielectric sphere.

where $\underline{A}$ is evaluated at the field point $\underline{r}=(x,y,z)$ and $I\underline{\ell}$ is situated at the source point $\underline{r}'=(x',y',z')$ with k_c being the free-space propagation constant. The distance between the field and the source points is given by:

$$|\underline{r}-\underline{r}'| = \sqrt{(x-x')^2 + (y-y')^2 + (z-z')^2} \quad . \tag{5.8}$$

For an x-directed dipole located on the z-axis at a distance z_o from the origin (Fig. 5.5), the vector potential simplifies to:

$$\underline{A} = \hat{i}_x A_x$$

and

$$|\underline{r}-\underline{r}'| = \sqrt{x^2 + y^2 + (z-z_c)^2} \quad . \tag{5.9}$$

Hence, the exact electromagnetic field of this electric dipole can be obtained from Equations (5.5) and (5.6) and using Equations (5.7) and (5.9).

5.3.2 Spherical Modal Expansion of the Electric Dipole Fields

The spherical modal expansion of the fields of an electric dipole located at $\underline{r}=\underline{r}_o$, are given by Equations (4.3), (4.4), (4.7) and (4.8) using the appropriate radial function $z_n^{(i)}(k_o r) = j_n(k_o r)$ for $r<r_o$ and $z_n^{(i)}(k_o r) = h_n^{(2)}(k_o r)$ for $r>r_o$. The uknown coefficients in this expansion $a_{\substack{e\\mn\\o}}$ and $b_{\substack{e\\mn\\o}}$

are available in the literature [34] and [47] for an arbitrary location and orientation of the electric dipole and are of the form:

$$a_{\substack{e\\mn\\o}} = \begin{cases} \dfrac{k_o^2 \eta I \underline{\ell}}{\gamma_{mn}} \cdot \underline{m}^{(1)}_{\substack{e\\mn\\o}}(\underline{r}_o) & \text{for } r>r_o \qquad (5.10a) \\ \dfrac{k_o^2 \eta I \underline{\ell}}{\gamma_{mn}} \cdot \underline{m}^{(4)}_{\substack{e\\mn\\o}}(\underline{r}_o) & \text{for } r<r_o \qquad (5.10b) \end{cases}$$

and

$$b_{\substack{e\\mn\\o}} = \begin{cases} \dfrac{k_o^2 \eta I \underline{\ell}}{\gamma_{mn}} \cdot \underline{n}^{(1)}_{\substack{e\\mn\\o}}(\underline{r}_o) & \text{for } r>r_o \qquad (5.11a) \\ \dfrac{k_o^2 \eta I \underline{\ell}}{\gamma_{mn}} \cdot \underline{n}^{(4)}_{\substack{e\\mn\\o}}(\underline{r}_o) & \text{for } r<r_o \qquad (5.11b) \end{cases}$$

where: $\underline{m}^{(i)}(\underline{r}_o)$ and $\underline{n}^{(i)}(\underline{r}_o)$ are the spherical vector wave functions given by Equations (4.7) and (4.8), respectively at $\underline{r}=\underline{r}_o$, η is the intrinsic impedance of free space, k_o is the free space propagation constant, $\underline{r}_o$ is the location of the dipole from the origin 0, $I\underline{\ell}$ is the moment of the dipole and γ_{mn} is given by Equation (4.33). The coefficients given

in Equations (5.10) and (5.11) are different from those of references [34] and [47] by a constant factor $j\omega$.

Since the dipole is located on the z-axis as shown in Fig. 5.5, the expansions of Equations (4.2) and (4.3) will be restricted only to m=1 terms. This is due to the fact that, for $\theta_o=\pi$, $\phi_o=0$ and from [21], [34] and [47] we have:

$$\left.\frac{mP_n^m(\cos\theta_o)}{\sin\theta_o}\right|_{\theta_o=\pi} = \begin{cases} (-1)^n \dfrac{n(n+1)}{2} & m=1 \\ 0 & m\neq 1 \end{cases} \tag{5.12a}$$

and

$$\left.\frac{\partial P_n^m(\cos\theta_o)}{\partial\theta_o}\right|_{\theta_o=\pi} = \begin{cases} (-1)^{n+1} \dfrac{n(n+1)}{2} & m=1 \\ 0 & m\neq 1 \end{cases} \tag{5.12b}$$

Since, at least one of these functions appear in each spherical functions $\underline{m}^{(i)}$ and $\underline{n}^{(i)}$, they become zero when m is not equal to unity. Thus, for the dipole source of Fig. 5.5 the exact coefficients become:

$$a_{emn} = b_{omn} = 0$$

and

$$a_{omn} = \begin{cases} -\dfrac{k_o^2 \eta I \ell}{\gamma_{1n}} (-1)^n \dfrac{n(n+1)}{2} h_n^{(2)}(k_o r_o) & \text{for } m=1 \\ 0 & \text{for } m\neq 1 \end{cases} \tag{5.13a}$$

and

$$b_{emn} = \begin{cases} -\dfrac{k_o^2 \eta I \ell}{\gamma_{1n}} (-1)^{n+1} \dfrac{n(n+1)}{2} \dfrac{1}{k_o r} \dfrac{\partial}{\partial r} [r h_n^{(2)}(k_o r)] \Big|_{r=r_o} & \text{for } m=1 \\ 0 & \text{for } m \neq 1 \end{cases} \quad (5.13b)$$

where γ_{1n} is given by Equation (4.33) for m=1. Utilizing these results, the spherical wave expansion of an x-directed electric dipole located on the negative half of the z-axis can be written in the form:

$$\underline{E}^i = - \sum_{n=1}^{\infty} (a_{o1n} \underline{m}_{o1n}^{(1)} + b_{e1n} \underline{n}_{e1n}^{(1)}) \quad (5.14)$$

and

$$\underline{H}^i = \frac{k_o}{j\omega\mu_o} \sum_{n=1}^{\infty} (a_{o1n} \underline{n}_{o1n}^{(1)} + b_{e1n} \underline{m}_{e1n}^{(1)}) \quad (5.15)$$

where $\underline{m}$ and $\underline{n}$ are the spherical wave functions and are given by Equations (4.7) and (4.8), respectively. For expansion to be valid for $r<r_o$, the radial functions are selected as $z_n^{(i)}(k_o r)=j_n(k_o r)$ and a_{o1n} and b_{e1n} are given by Equations (5.13).

5.3.3 Numerical Investigation

The problem here is similar to that of the plane wave case. The exact field of the dipole together with exact

scattered field of the dielectric sphere are used to generate the measurement data. The required expansion coefficients are calculated and are used to reconstruct the field of the electric dipole.

The reconstructed data are used to study the convergence of the spherical expansion series, to investigate the dependence of the expansion series on the location of the dipole and to compare the accuracy of the reconstructed field with and without optimal distribution of the measurement points.

5.3.3.1 Convergence of the spherical wave expansions of an electric dipole

In this case, the convergence of the spherical wave expansions of an x-directed electric dipole located on the z-axis is investigated. The field measurement using scattering technique of chapter four is utilized and the matrix method is used to calculate the unknown coefficients of the incident electromagnetic fields of Equations (5.14) and (5.15). The geometrical and physical parameters are selected as those of the plane wave case discussed in section (5.2). That is radii of the dielectric and the measurement spheres are a and A such that $k_0 a=1.0$ and $k_0 A=3.0$. Also, the dipole is located on the z-axis at a point $r_0=(0,0,z_0)$ with $k_0 z_0=10.0$. The centers of the scatterer (dielectric sphere) and the measurement sphere

are located at the origin 0 as shown in Fig. 5.5. Also, its relative permittivity ε_r and permeability μ_r are chosen to be 4.0 and 1.0, respectively. The tangential components of the incident electric fields E_θ^i and E_ϕ^i are calculated using the spherical wave expansion at $\phi=0$ and $\phi=\frac{\pi}{2}$ planes. These calculated tangential components are compared in Figs. 5.6 to 5.9 with that obtained from the exact solution of Equations (5.5) and (5.7). The comparison is made on a sphere of radius $k_0 r_1=3.0$ and for different number of terms in the expansion series. Figs. (5.6) and (5.7) compare the calculated amplitude and phase of E_θ^i with the exact ones in the plane $\phi=0$. Corresponding comparison for E_ϕ^i in the $\phi=\frac{\pi}{2}$ plane is shown in Figs. 5.8 and 5.9 for the calculated amplitude and phase of this component. These comparisons show that the calculated E_θ^i and E_ϕ^i converge rapidly and for number of terms $N\geq 7$, the accuracy is better than 0.01%. In computation of all these results the optimum distribution of the measurement points in the θ-direction was utilized.

5.3.3.2 Effect of the dipole location on the truncation error

Three cases are considered in this section, in which dipole distances from the origin are $k_0 z_0=5.0$, 10.0 and 20.0. The mean percentage errors in $\phi=0$ plane of the magnitude and the phase of E_θ^i as defined in Equation (3.37) are shown in

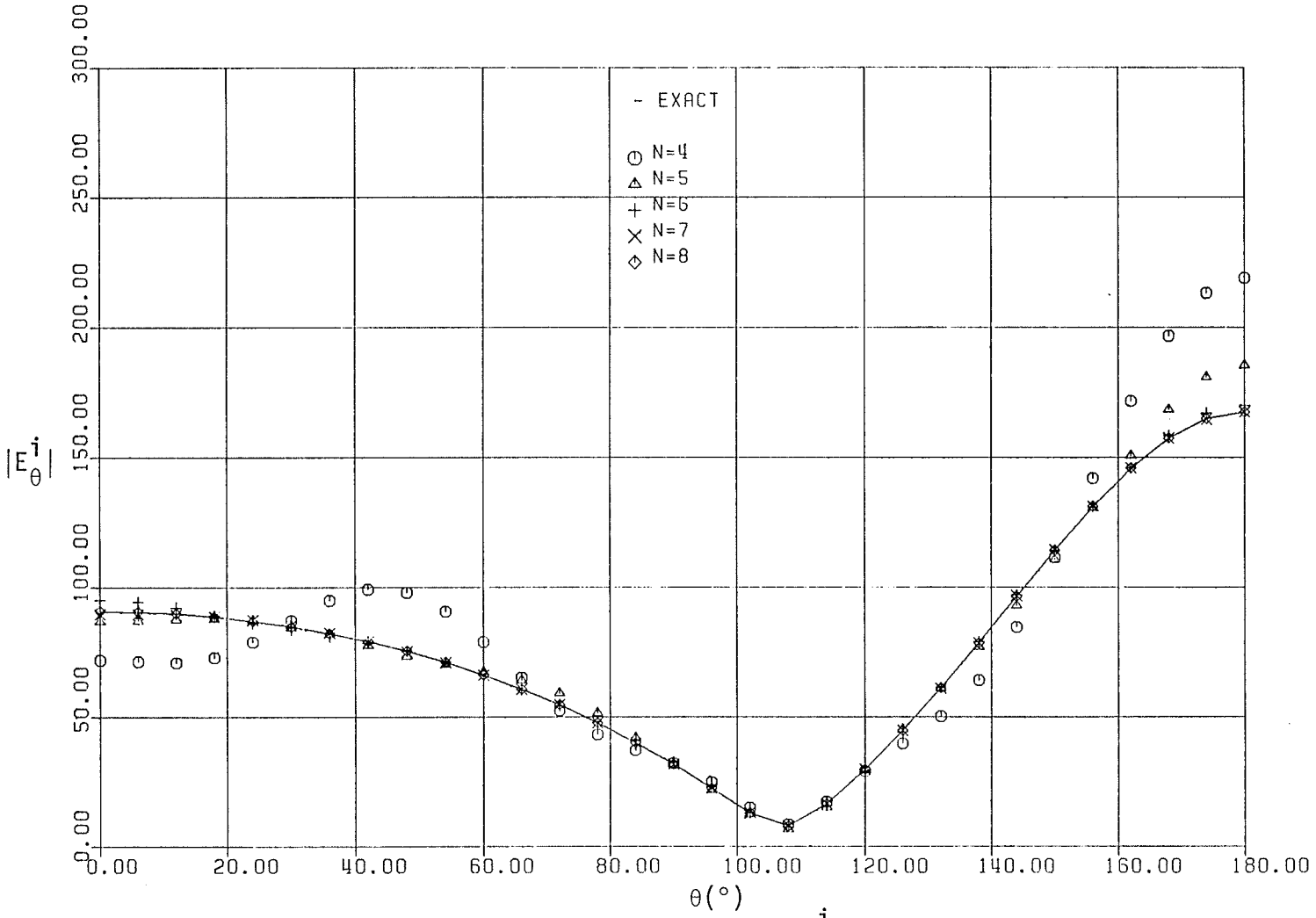

Fig. 5.6: Comparison of the reconstructed amplitude of E_θ^i with the exact one, ϕ=0, dipole source.

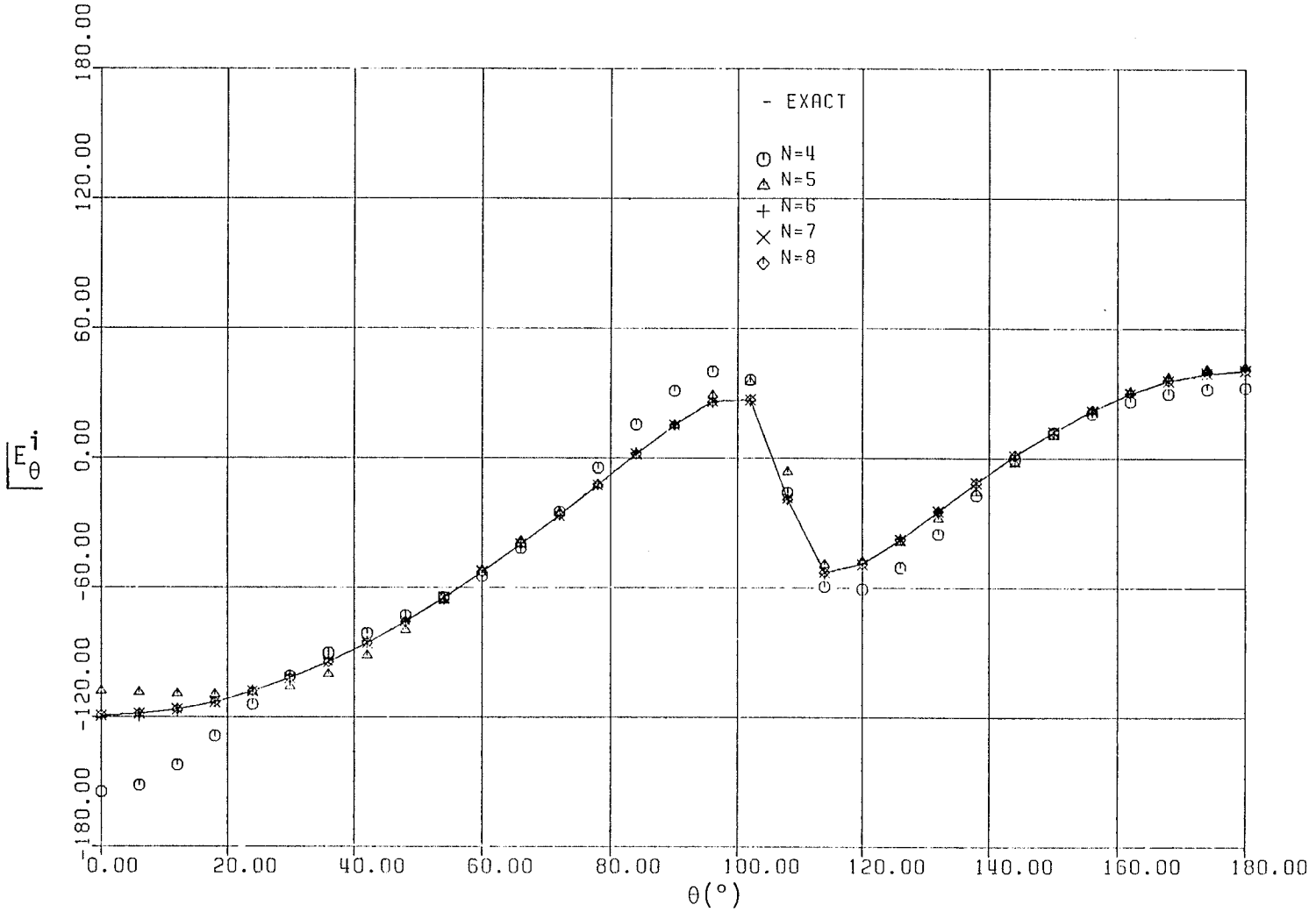

Fig. 5.7: Comparison of the reconstructed phase of E_θ^i with the exact one, ϕ=0, dipole source.

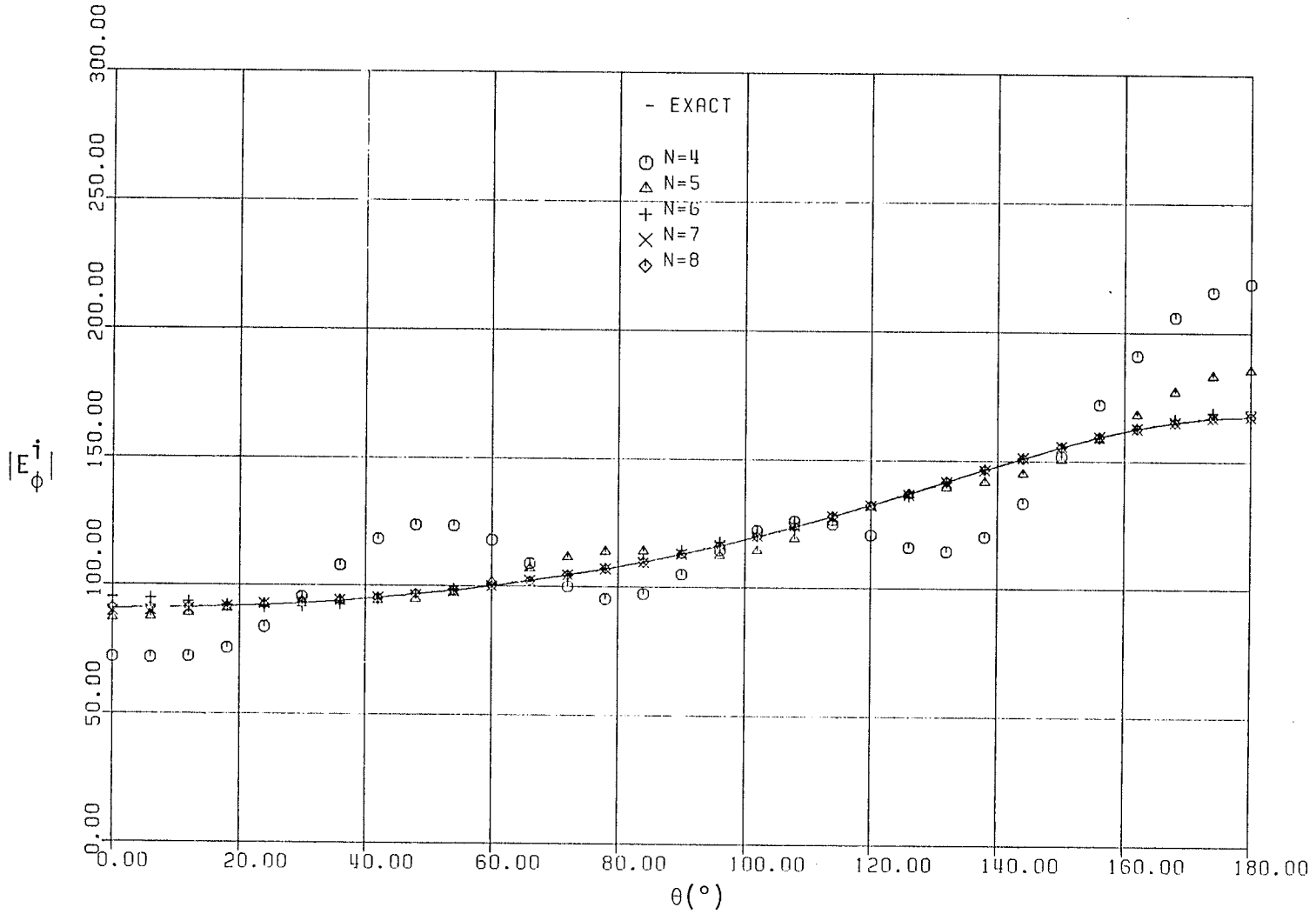

Fig. 5.8: Comparison of the reconstructed amplitude of E_ϕ^i with the exact one, $\phi = \frac{\pi}{2}$, dipole source.

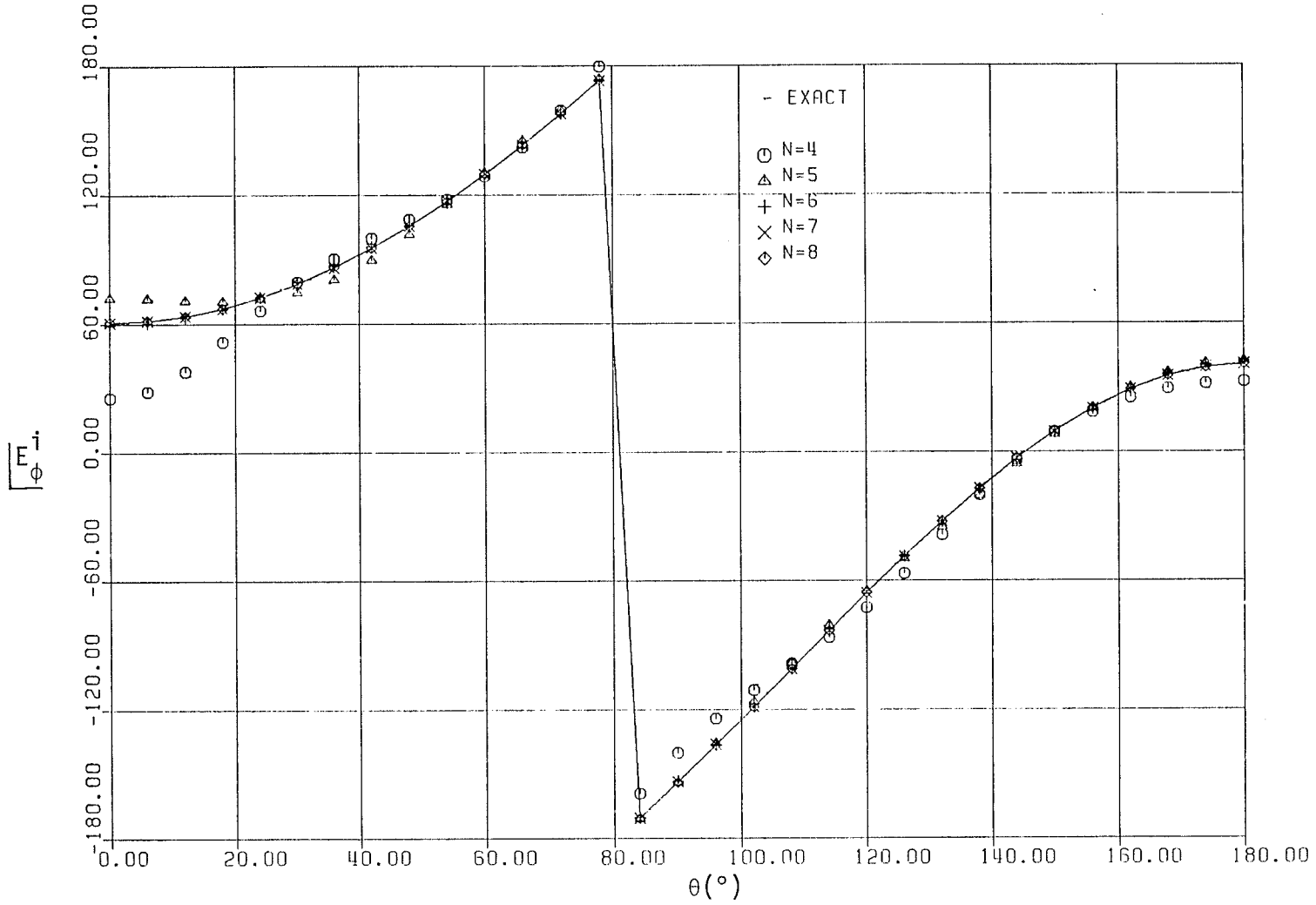

Fig. 5.9: Comparison of the reconstructed phase of E_ϕ^i with the exact one, $\phi = \frac{\pi}{2}$, dipole source.

Figs. 5.10 and 5.11. Also, the mean percentage error of the magnitude and the phase of E^i_ϕ at $\phi = \frac{\pi}{2}$ plane are shown in Figs. 5.12 and 5.13, respectively. It is noticed from Figs. 5.10 to 5.13 that for the same accuracy, when the dipole is located at $k_o z_o = 20.0$ and 10.0, both series of Equations (5.14) and (5.15) converge much faster than the case of $k_o z_o = 5.0$.* As an example, in Fig. 5.10, the mean percentage error is less than 0.36% for $k_o z_o = 10.0$ and 20.0, when 7 terms in the series are used. While it is more than 8.6% for $k_o z_o = 5.0$ and using the same number of spherical harmonics. Similarly, for N=8, it is evident from the same figure that, the error is less than 0.05% for $k_o z_o = 10.0$ and 20.0 but becomes more than 5.4% for $k_o z_o = 5.0$. The above results are for the magnitude of the tangential components E^i_θ of the calculated incident electric field at $k_o r_1 = 3.0$. Similar results obtained for the error in the phase of E^i_θ are shown in Fig. 5.11 and the error in the magnitude and the phase of E^i_ϕ-component are shown in Figs. 5.12 and 5.13, respectively.

These results are significant from the measurement point of view. They indicated that, if the measurements are carried out over a measurement sphere at a larger distance from the source, the convergence of the series is faster and smaller number of coefficients need to be computed. This, of course, means that smaller number of measurements need to be carried.

*This can be shown analytically by evaluating the ratio of two consecutive terms in the series of equations (5.14) and (5.15), (the convergence ratio test). For higher order terms, this ratio is proportional to $k_o r / k_o z_o$ $(r<z_o)$, which decreases as z_o increases, i.e., the convergence of the series improves as z_o increases.

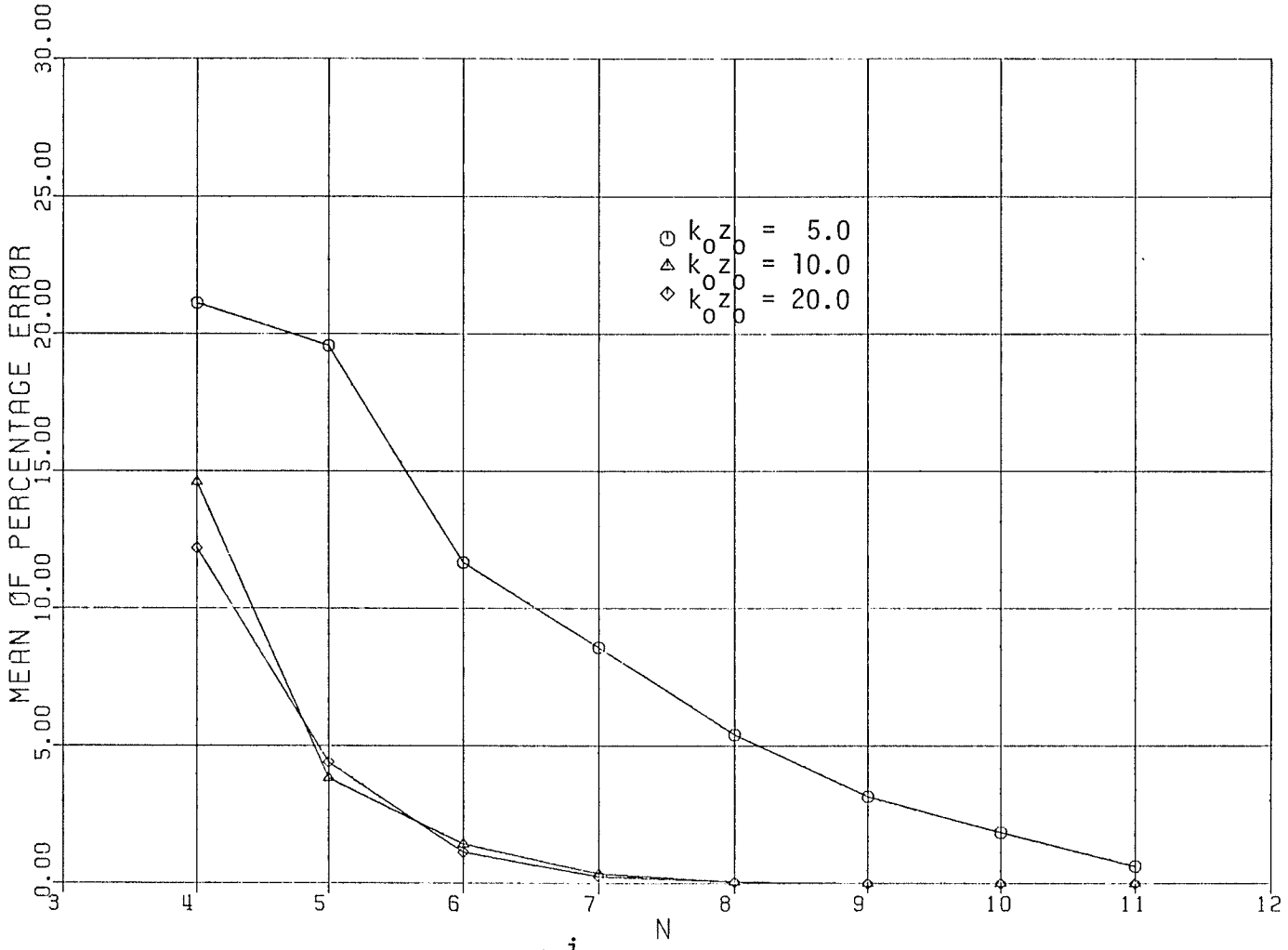

Fig. 5.10: Mean percentage error of $|E_\theta^i|$ against the truncation order N at different locations of the dipole source.

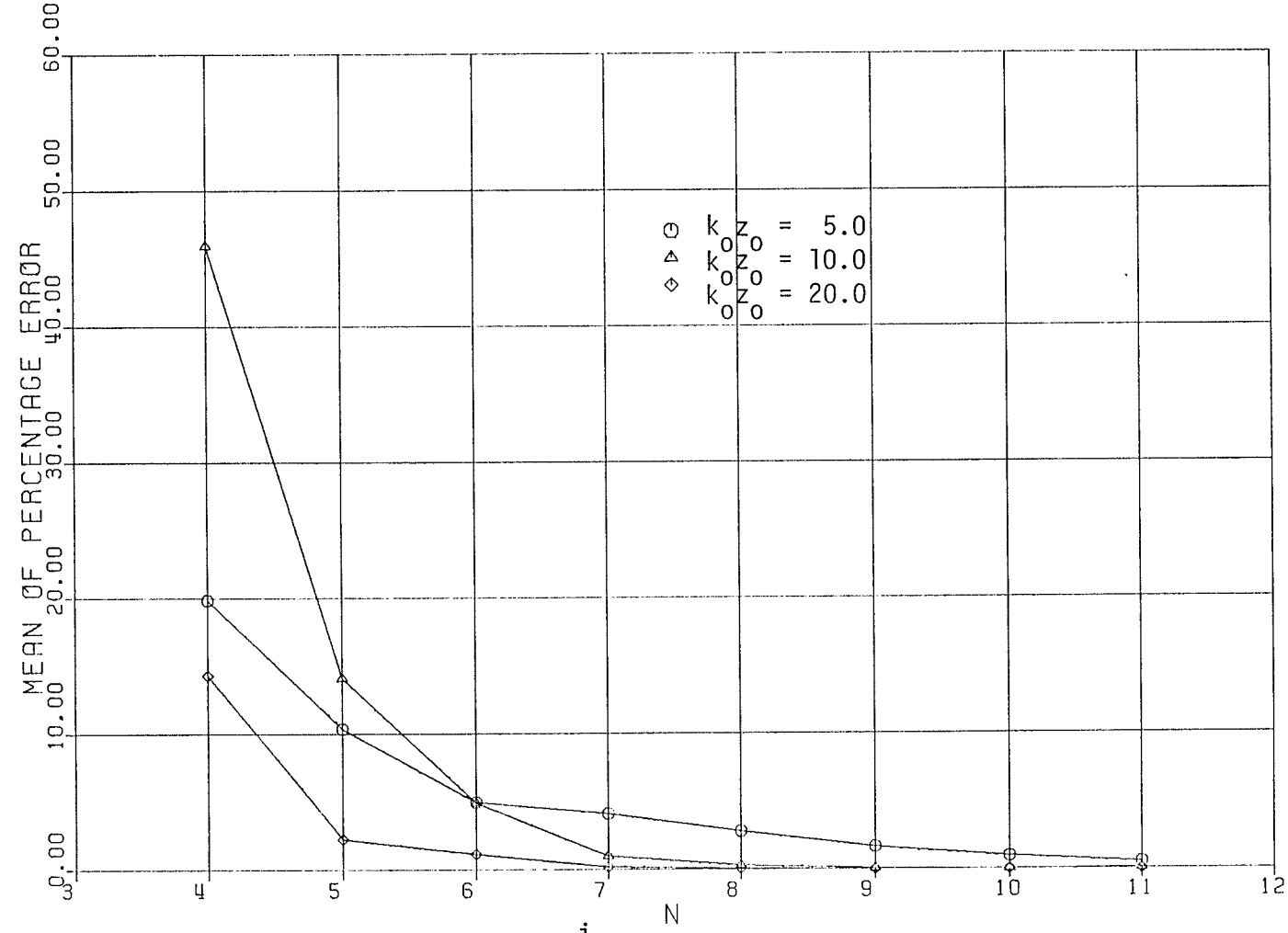

Fig. 5.11: Mean percentage error of $|E_\theta^i|$ against the truncation order N at different locations of the dipole source.

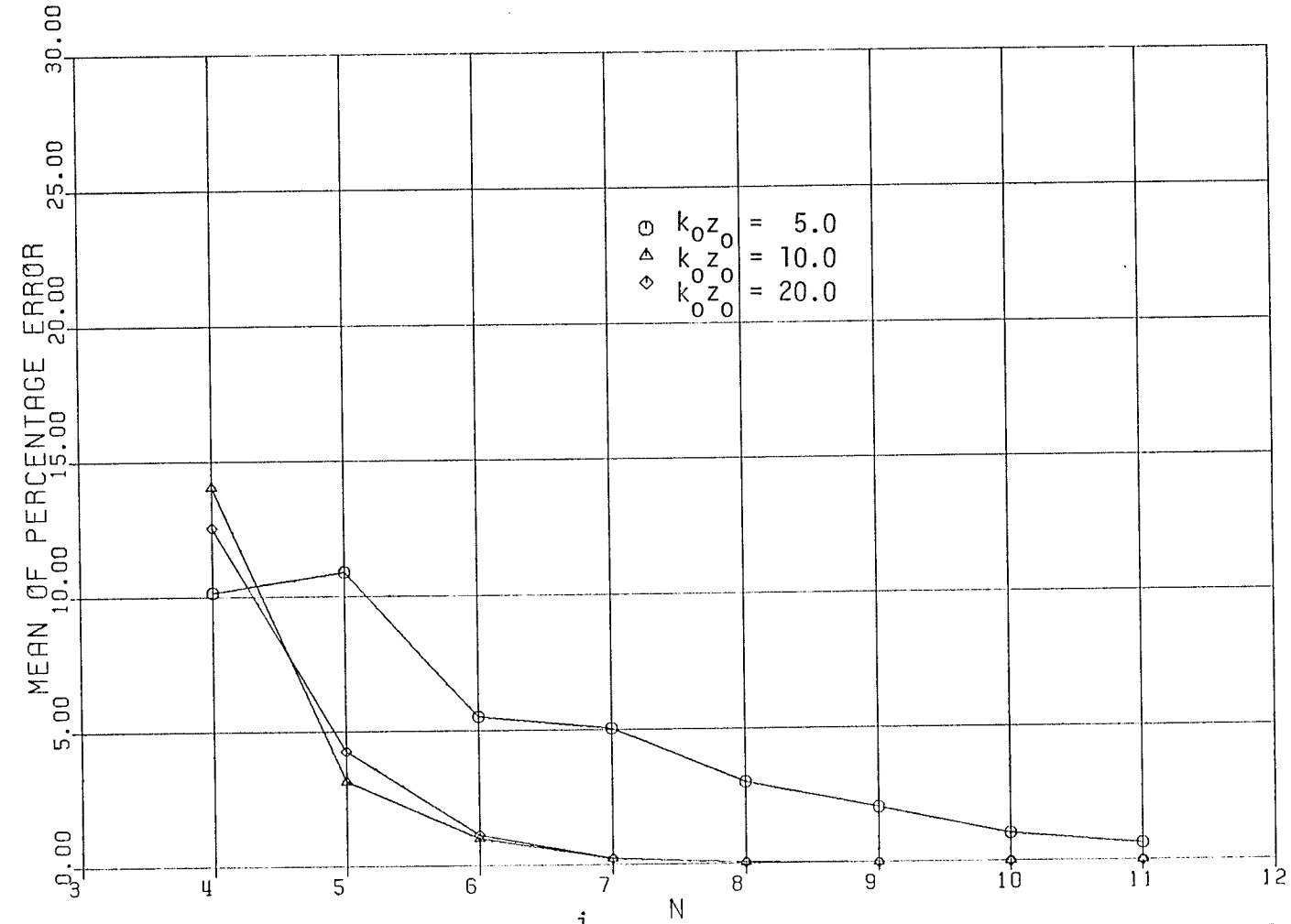

Fig. 5.12: Mean percentage error of $|E_\phi^i|$ against the truncation order N at different locations of the dipole source.

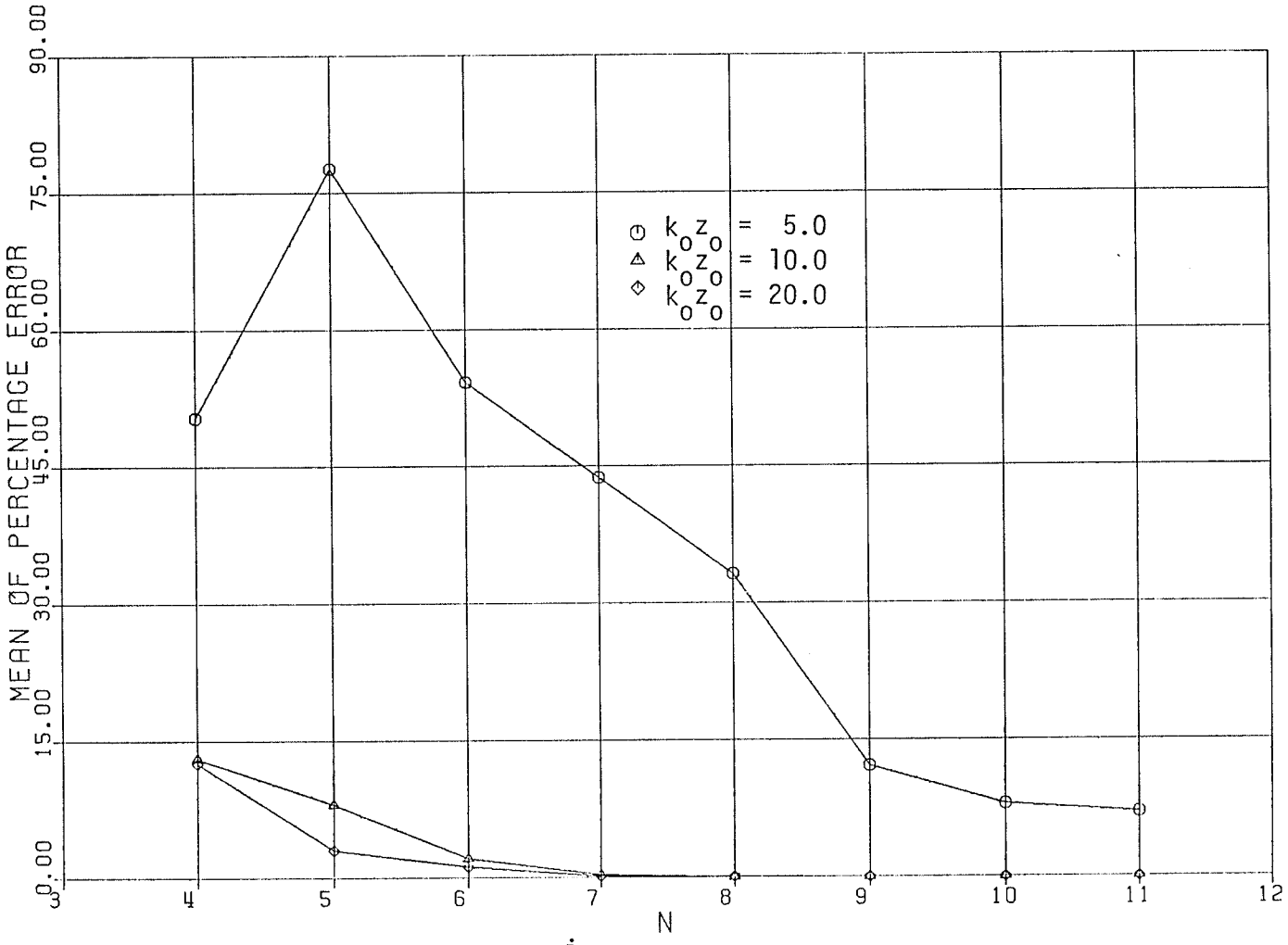

Fig. 5.13: Mean percentage error of $\left|E_\phi^i\right|$ against the truncation order N at different locations of the dipole source.

out. In other words, to obtain the given degree of accuracy, in the calculated electromagnetic field using scattering data technique, it is better to scan the receiving probes far from the test antenna.

5.3.3.3 The effect of using non-optimal distributions of the receiving probes on the calculated field of the electric dipole source

a) Selection of the non-optimal measurement points

The optimization function which determines the best locations of the receiving probes with respect to θ is given by Equation (4.26). The reason for using this optimization function is that, it provides measurement points which maximize the determinant of the matrix S in Equation (4.22). This assured the most stable inversion of the matrix S [43]. The question which arises here is that, what will happen if the receiving probes are positioned at locations other than the optimum ones given by the roots of the optimization function of Equation (4.26). Can one still obtain a reasonable result also in such cases? In section 5.3.3.1, for an electric dipole, a numerical investigation was carried out at the optimum locations of the receiving probe. In this section, the same case is considered but using non-optimum distribution of the receiving probe. In this case, the truncation order N for calculating the incident electric field using the spherical

wave expansion of Equation (5.14) is taken to be between 4 to 8. Also, the electric dipole source is assumed to be x-directed and located at a distance z_o, such that, $k_o z_o = 10.0$ on the negative part of the z-axis as shown in Fig. 5.5. Again, the azimuthal dependence ϕ here will be m=1 as mentioned before in section 5.3.2. The radii of the dielectric and measurement spheres are taken such that $k_o a = 1.0$ and $k_o A = 3.0$, respectively. Table 5.1 shows the optimum and the chosen non-optimum distribution of the θ-locations which are used in this numerical investigation. From numerical computation point of view, the non-optimum locations of the probe should be chosen such that none of these points should make the maxtrix S singular. This condition can be satisfied by avoiding the θ-locations which cause the singularity of the matrix S. These points are given by theorem (1) of reference [43] and are given by:

$$\left.\begin{array}{ll} \text{(i)} & \theta_i = 0,\ i = 1,2,\ \ldots,\ N \\ \text{or} & \\ \text{(ii)} & \theta_i = \theta_{i+1},\ i = 1,2,\ ---,\ (N-1) \\ \text{or} & \\ \text{(iii)} & \theta_i = \pi,\ i = 1,2,\ \ldots,\ N \end{array}\right\} \qquad (5.16)$$

In Table 5.1, measurement points are chosen such that the above three conditions are satisfied to prevent the singularity of the matrix S.

Table 5.1: The optimum and non-optimum distribution of the locations of the angular positions θ of the receiving probes for N=4 to 8, in degrees.

N=4		N=5		N=6		N=7		N=8	
Optimum	Non-Optimum	Optimum	Non-Optimum	Optimum	Non-Optimum	Optimum	Non-Optimum	Optimum	Non-Optimum
28.36	30.00	23.07	30.00	19.95	30.00	16.26	30.00	11.48	30.00
70.12	70.00	57.32	60.00	47.16	50.00	40.54	50.00	36.87	40.00
109.88	110.00	90.00	90.00	76.11	80.00	65.17	70.00	57.32	60.00
151.64	150.00	122.68	120.00	103.89	100.00	90.00	90.00	78.46	80.00
		156.93	150.00	132.84	130.00	114.83	110.00	101.54	100.00
				160.05	150.00	139.46	130.00	122.68	120.00
						163.74	150.00	143.13	140.00
								168.52	150.00

Figs. 5.14 and 5.15 show the magnitude and the phase of the calculated incident electric field component E_θ^i of the electric dipole, respectively. The exact magnitude and phase of the same component are also shown in these figures for comparison. The incident electric field is calculated using the spherical wave expansion of Equation (5.14) with N=4 to 8 and using the non-optimum distribution of the measurement points with respect to θ as given by Table 5.1. The magnitude and the phase of the incident electric field component E_ϕ^i of the same source are shown in Figs. 5.16 and 5.17, respectively along with the exact ones. Corresponding results, for the optimum distribution of the points were presented in section 5.3.3.1 and shown in Figs. 5.6 to 5.9. From Figs. 5.14 to 5.17, it is evident that, the calculated fields using spherical wave expansion and non-optimum distributions of the θ-locations still converge to the exact solution. However, a larger number of spherical harmonics are needed in this case than the optimum distribution case. This result is important from experimental point of view. Since in some cases, it may not be convenient to position the receiving probes at the optimum locations of the optimization function of Equation (4.26). These results indicate that with non-optimum measurement points, accurate results can still be obtained provided that the conditions of Equations (5.16) are satisfied. This is also important for cases where, for practical reasons, one utilizes several fixed

probes. The selection of non-optimum distribution of measurement points, however, reduces the accuracy of the results for a given number of spherical harmonics. This is the price which one will pay for the convenience of non-optimal distribution of the receiving points.

b) Error analysis for optimum and non-optimum distributions of θ-locations

The percentage errors in the magnitude of the tangential component E_θ^i of the electric dipole are shown in Figs. 5.18 and 5.19 for truncation orders N=7 and 8, respectively. Corresponding results were also obtained for the phase of E_θ^i, and for the magnitude and the phase of E_ϕ^i components but are not shown here. These figures compare the error distributions of optimum and non-optimum measurement points for the whole range of $0 \leq \theta \leq \pi$. In both cases, the mean value of the percentage errors using the optimum measuring points is always less than that of the non-optimum points. As an example, for N=7 case, the mean value of the percentage error is equal to 0.359% for the optimum case, but it increases to 0.653% for the non-optimum case. Similarly, for N=8 case, the mean value of the percentage errors are equal to 0.051% and 0.151% in the optimum and non-optimum cases, respectively. The mean value of the errors is decreased by a factor of 7.0 for the optimum case when the number of harmonics N is increased from

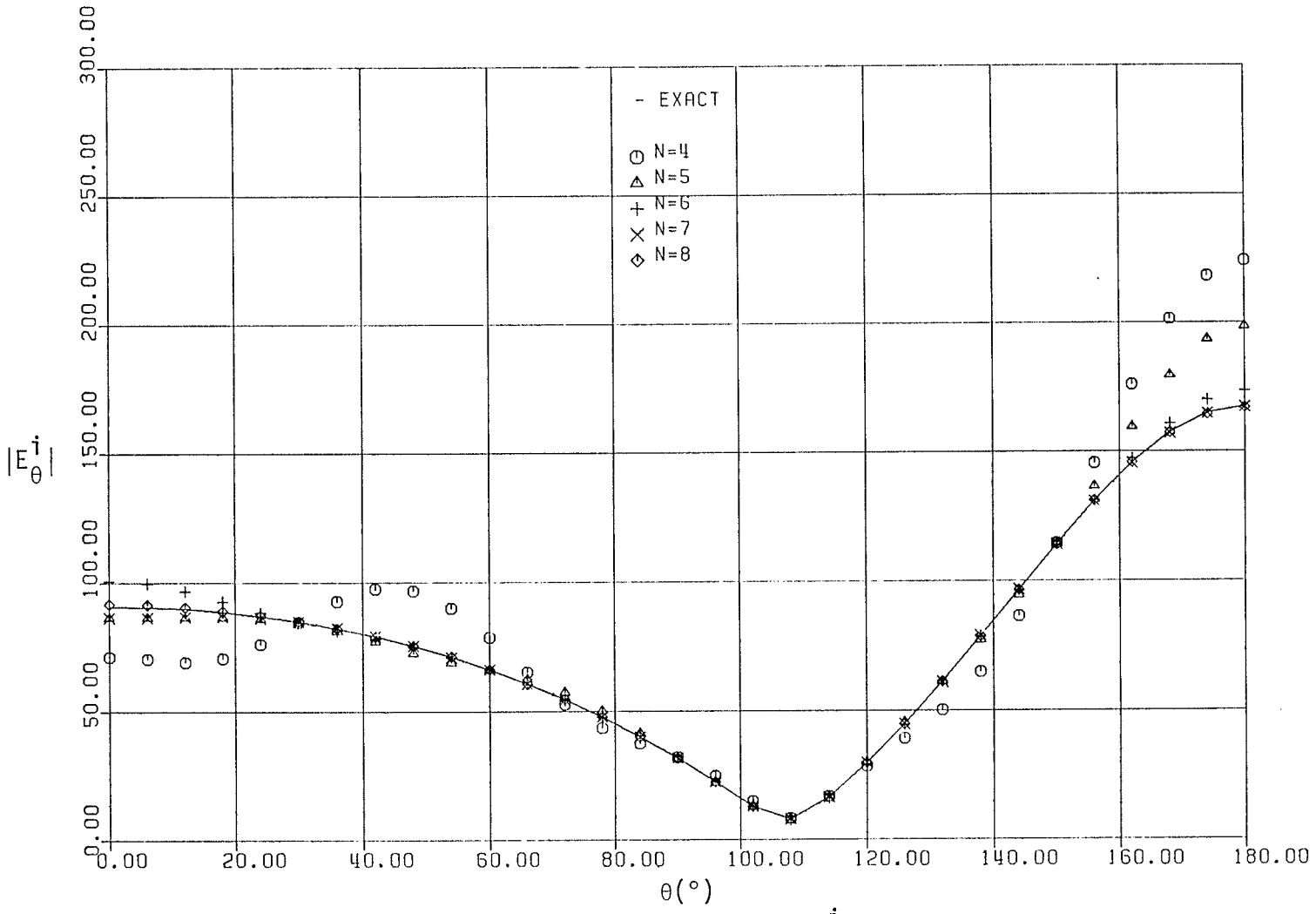

Fig. 5.14: Comparison of the reconstructed amplitude of E_θ^i with the exact one using non-optimum points, ϕ=0, dipole source.

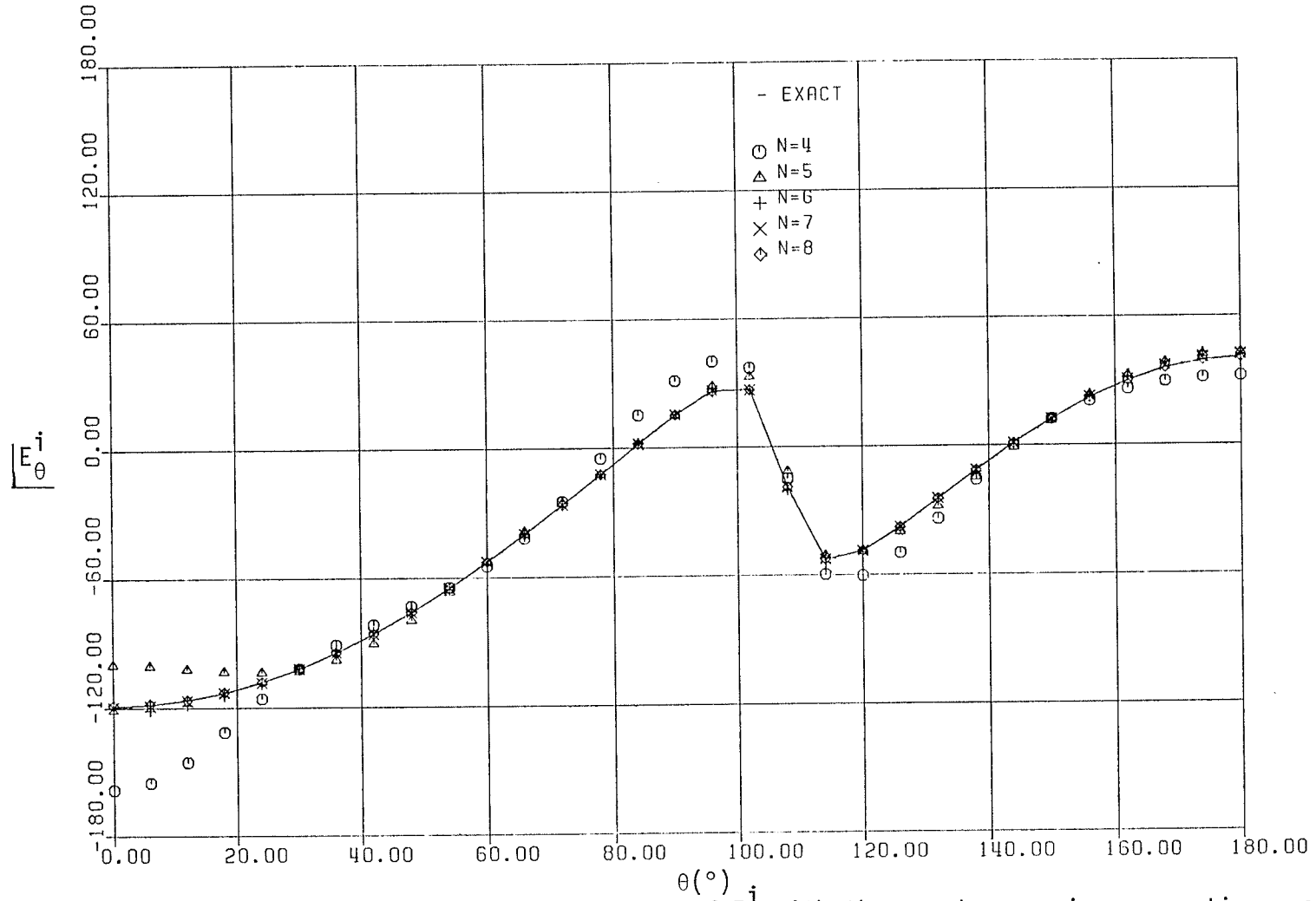

Fig. 5.15: Comparison of the reconstructed phase of E_θ^i with the exact one using non-optimum points, ϕ=0, dipole source.

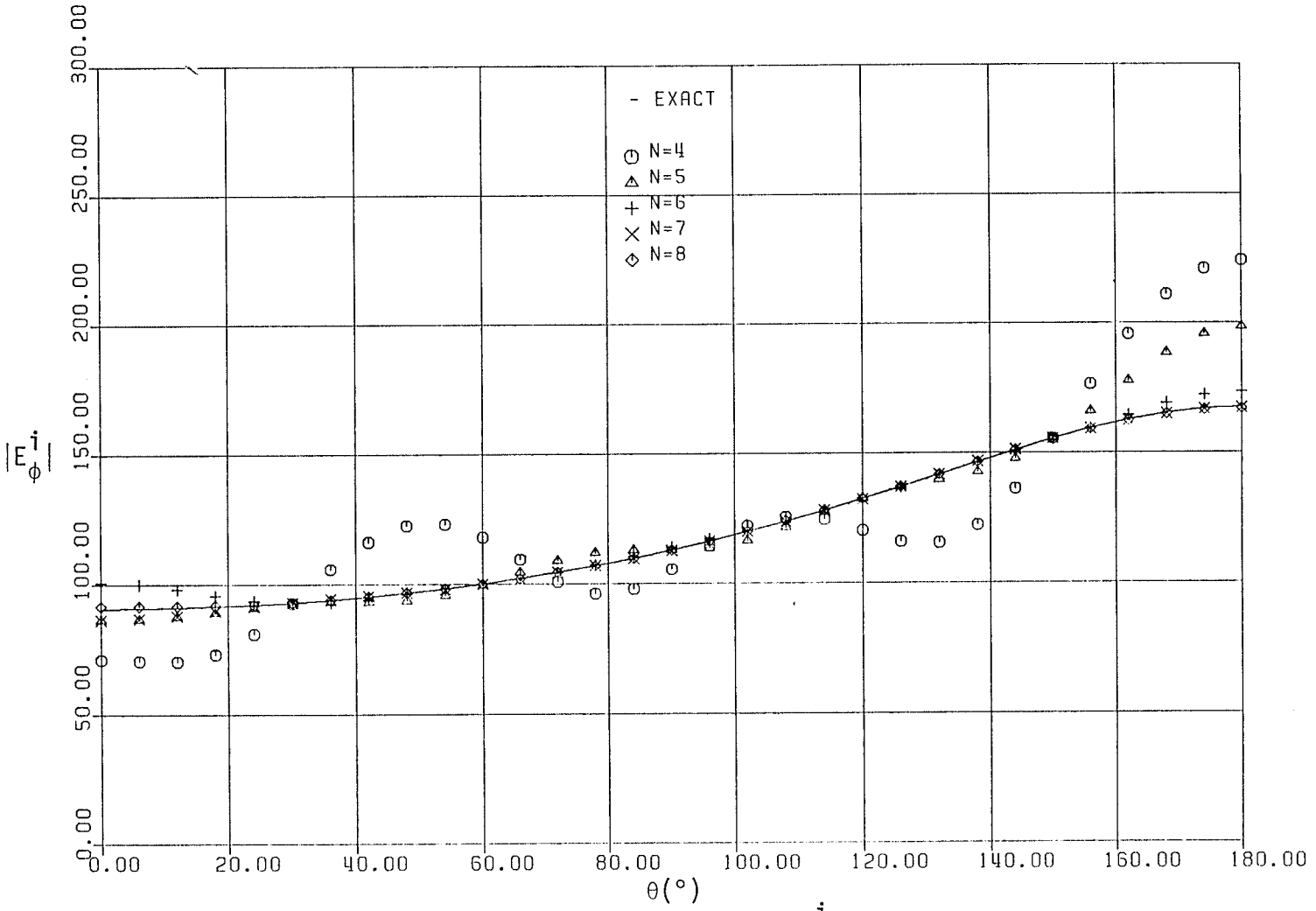

Fig. 5.16: Comparison of the reconstructed amplitude of E_ϕ^i with the exact one using non-optimum points, $\phi = \frac{\pi}{2}$, dipole source.

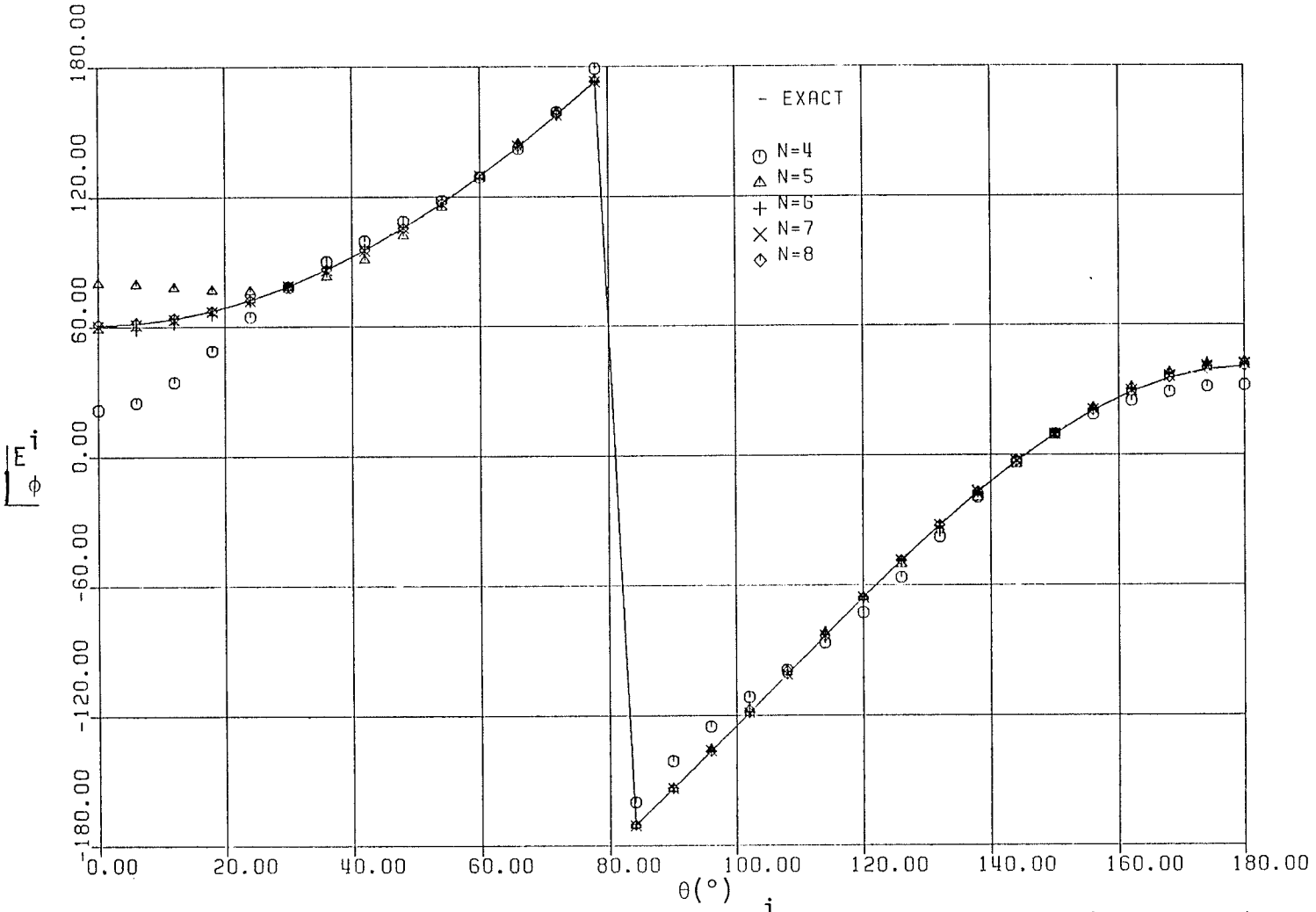

Fig. 5.17: Comparison of the reconstructed phase of E^i_ϕ with the exact one using non-optimum points, $\phi = \frac{\pi}{2}$, dipole source.

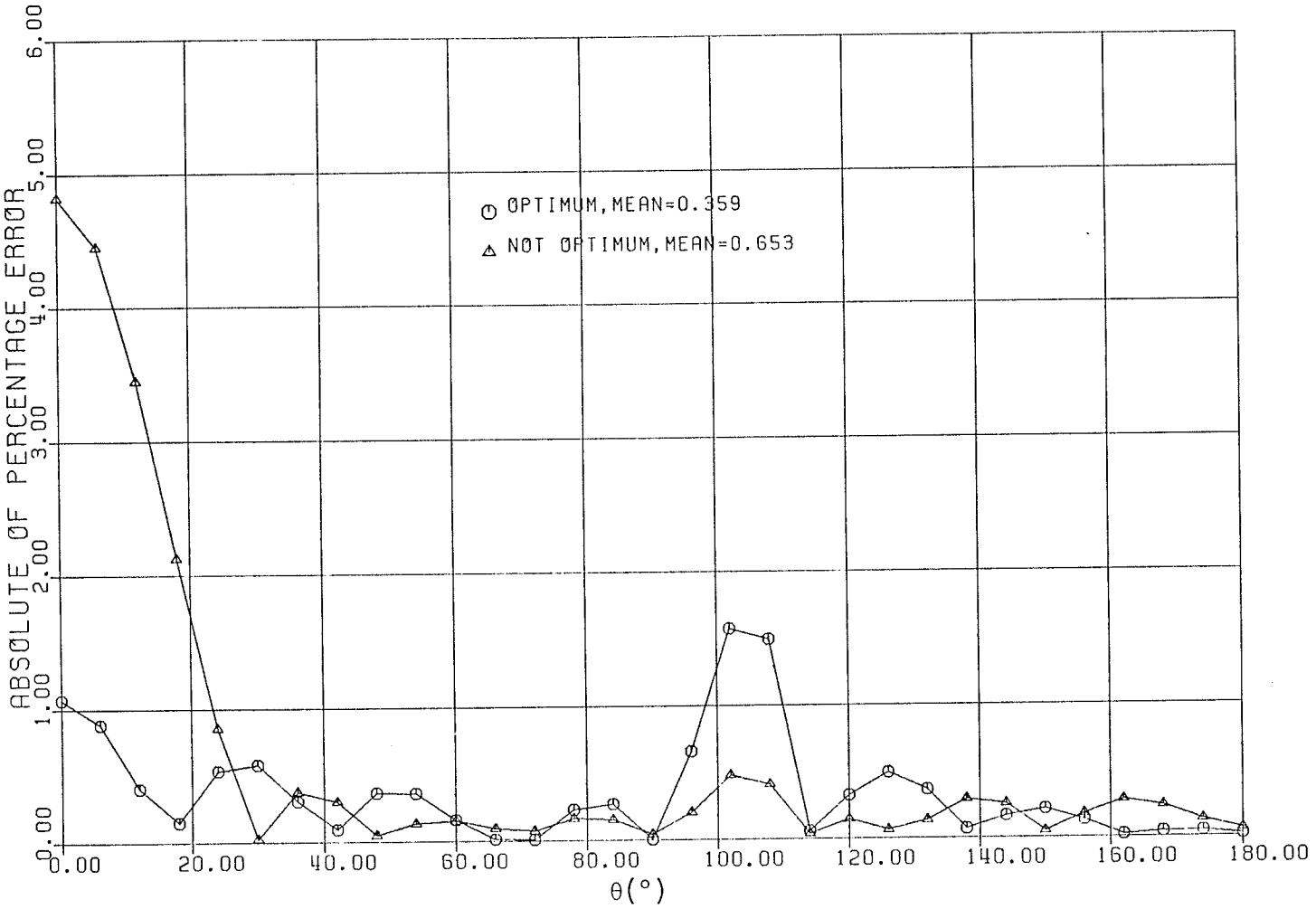

Fig. 5.18: Percentage error of $|E_\theta^i|$ for optimum and non-optimum distribution of the measuring probe, N=7.

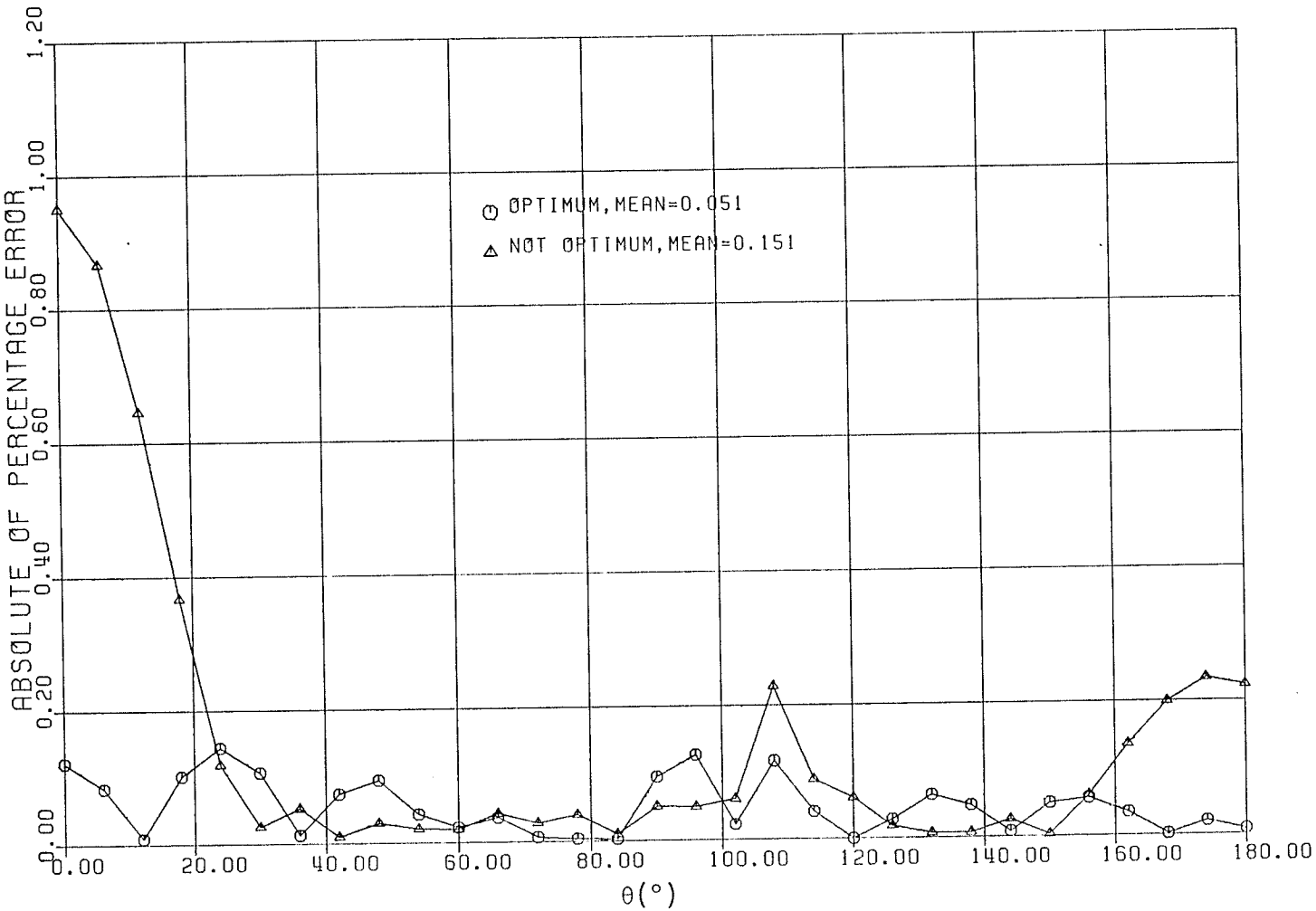

Fig. 5.19: Percentage error of $|E_\theta^i|$ for optimum and non-optimum distribution of the measuring probe, N=8.

7 to 8. While in the non-optimum case, it is decreased only by a factor of 4.32 for the same increase in N. From these results one can conclude that selecting non-optimum distribution of the measurement points such as in the case of several fixed probes, the accuracy of the reconstructed field is low. However, the accuracy can be improved by increasing the number of the measurement points. This is clearly shown in Figs. 5.18 and 5.19 for N=7 and 8, respectively.

5.4 ELECTRIC DIPOLE ARRAY

The stepwise measurement method described in chapter four is used here to examine the accuracy of the computed fields. For the test antenna, a four-element electric dipole array is selected. Dipoles are x-directed electric current elements and are separated by a distance of $\lambda/4$, where λ is the free space wavelength. The phase center of the array is located at the origin 0 and the electrical phase difference of two adjacent elements is assumed to be $\delta = -3\pi/4$ radians. The array is radiating in presence of a dielectric sphere of radius a, as shown in Fig. 5.20. The measurement data are generated analytically over the measurement spheres S_1, S_2, ..., S_N and the stepwise measurement approach as explained in section (4.2) [46], is used to reconstruct the antenna fields. In Fig. 5.20 only three measurement spheres S_1, S_2

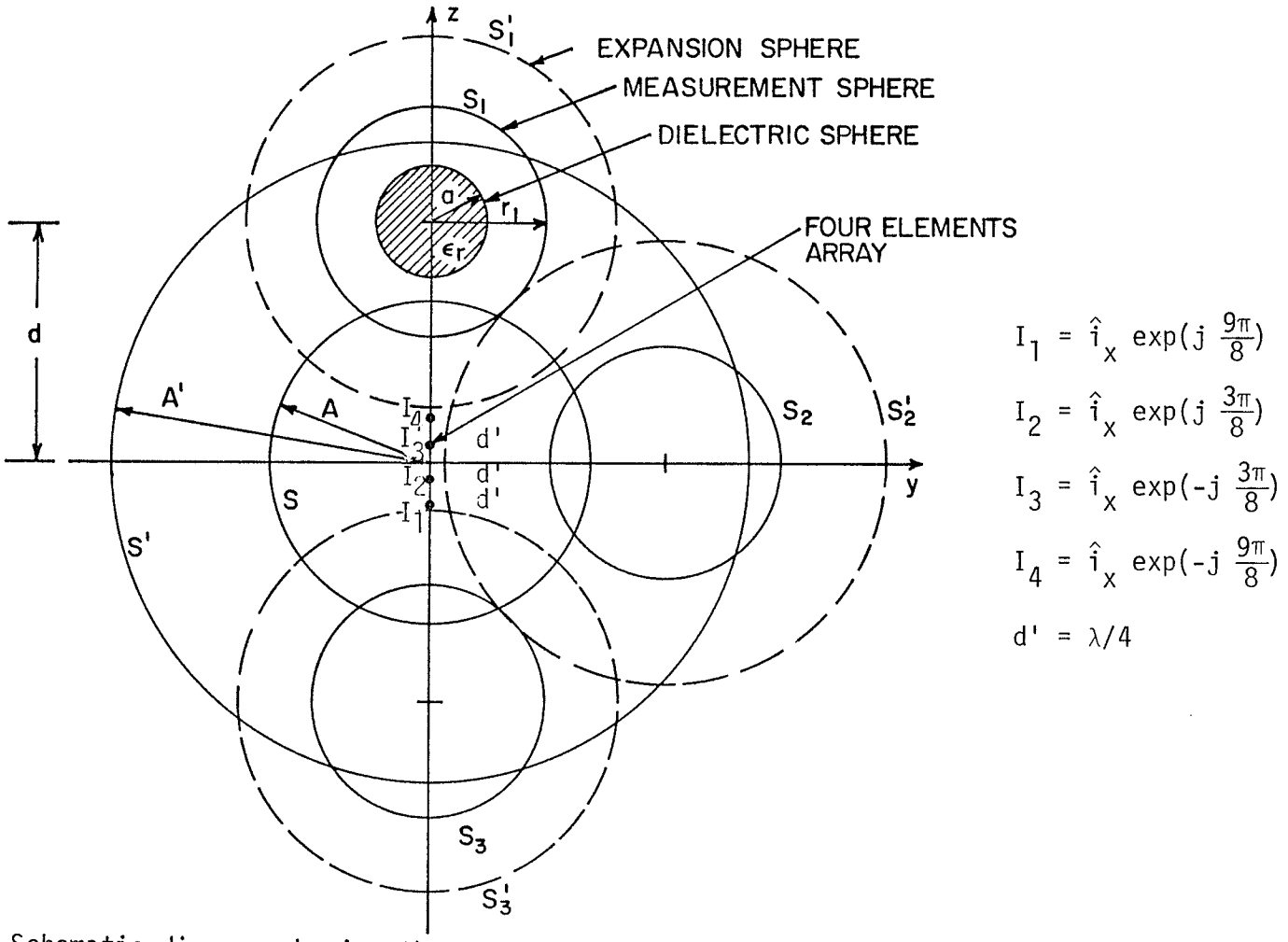

Fig. 5.20: Schematic diagram showing the test antenna, scatterer, measurement spheres S_1, S_2, S_3, expansion spheres S_1', S_2', S_3', spherical surfaces S enclosing the isolated antenna and S' enclosing both antenna and the scatterer, $\phi = \frac{\pi}{2}$.

and S_3 are indicated. The corresponding expansion spheres are S_1', S_2' and S_3'. Within each expansion sphere which contains one of the measurement spheres, spherical wave expansion with unknown coefficients are defined and the unknown coefficients are determined by matrix inversions as described in chapter four. These wave expansions are then used to compute the field components over the spherical surface S, which encloses the antenna and thus gives the near-field of the test antenna. If the far-field of the isolated antenna is desired, the field distributions over S can be used to determine the expansion coefficients for the field external to S. However, if the far-field of the antenna in the presence of the dielectric sphere is desired, the field components over a spherical surface S', which encloses both the antenna and the dielectric sphere can be obtained similar to those over S. These field components can be used to determine the desired expansion coefficients for the field of the test antenna in the vicinity of the dielectric sphere. Since in this example we have considered a spherical scatterer, a spherical near-field far-field transformation method will be used. Furthermore, to avoid large scanning systems required for large antennas, the stepwise approach is selected, in which the near-fields are measured over a small spherical surface in the vicinity of the scatterer. The required information on the field and over a surface enclosing the

antenna is then obtained by repeating the measurement at several locations around the antenna. This stepwise approach not only reduces the required scanning surface, but also reduces the expansion of antenna field over a large surface to several expansions over small surfaces. Note that when the dielectric constant of the scatterer becomes unity the problem reduces to the near-field measurement of an isolated antenna. In the following sections both cases will be considered, i.e., the far-field radiation patterns of an isolated antenna as well as that of the antenna in presence of dielectric sphere will be calculated. In both cases the following data are assumed for the numerical investigation:

radius of the dielectric sphere $k_0 a = 1.0$,
dielectric constant of the dielectric sphere $\varepsilon_r = 4.0$,
the separation between the center of the dielectric sphere and the origin 0 $k_0 d = 8.25$,
the radius of the measurement sphere $k_0 r_1 = 3.0$,
the radius of the spherical surface S which encloses only the antenna $k_0 A = 5.0$, and
the radius of the spherical surface S' which encloses both, the antenna and the scatterer $k_0 A' = 10.0$.

The reconstruction of the isolated antenna field and the field of the antenna in the presence of a dielectric

sphere will also be discussed. The results for the amplitude and the phase of E_θ are presented in detail. The results for E_ϕ are similar and therefore only a sample calculation is included.

5.4.1 Calculation of the Far-Field Radiation Pattern of the Isolated Antenna

In this section the far-field radiation pattern of the isolated antenna is calculated from the near-field measurement data and the calculated field over the surface S, Fig. 5.20. Note that, this spherical surface S with radius $k_0A=5.0$ encloses only the isolated antenna. The interaction between the antenna and the scatterer is neglected. In this example, the measurement data is generated analytically over the measurement spheres. Because the azimuthal dependence of the array field is known ($\cos\phi$ and $\sin\phi$ dependence only), measurements are carried out only in the $\phi=0$ plane for E_θ and in the $\phi=\frac{\pi}{2}$ plane for E_ϕ. To examine the usefulness of the stepwise measurement method, three different cases are studied [46]. Namely, three, four and five measurement spheres are utilized to obtain adequate information in the plane $\phi=0$ for E_θ and in the plane $\phi=\frac{\pi}{2}$ for E_ϕ to evaluate the expansion coefficients. These expansion coefficients are used to reconstruct the fields and the results are then used to find the resulting errors in the reconstructed fields.

5.4.1.1 Error analysis

Within each expansion sphere which contains one of the measurement spheres and is tangent to the antenna surface, field expansions are determined by using the measurement data. These field expansions are then used to calculate the field distributions over a spherical surface S enclosing the antenna. To examine the accuracy of the calculated fields, the exact field components over S are computed and the expected errors are calculated from:

$$e = |\{20 \log_{10}|(|E_{exact}| - |E_{calculated}|)|-20 \log_{10}| E_{exact}|\}|. \quad (5.17)$$

The measurement data are computed by solving the problem of scattering by a dielectric sphere. Expected errors for different numbers of the measurement spheres are also computed and the results for three and four measurement spheres are shown in Figs. 5.21 and 5.22, respectively for E_θ and E_ϕ components of the electric field. While Figs. 5.23 and 5.24 show the expected errors for four and five measurement spheres for the same components of the field. It is evident that the accuracy of the computation improves as the number of the measurement spheres increases. In a practical situation, the exact antenna field is unknown and the computation error must be defined as the difference of the fields for different number of measurement spheres. Note

that the exact near-field of the electric dipole array at any point on the spherical surface S is the summation of the fields from each element of the array. The exact field of each element is given by Equations (5.5), (5.6) and (5.7) taking into consideration that the phase difference between each two elements be $\delta = -3\pi/4$ radians.

The error distribution of E_θ-component at $\phi=0$ plane is shown in Fig. 5.21 using three and four measurement spheres in the range $0 \leq \theta \leq \pi$. The center of the i^{th} measurement sphere is located on the surface of a sphere with a radius $k_o d=8.25$. The measurement spheres are distributed on this surface, at the azimuthal plane $\phi=0$, according to the formula:

$$\theta_{ci} = \frac{\pi}{N_{ms}-1} (i-1) \text{ rad.} \qquad (5.18)$$

where N_{ms} is the number of the measurement spheres in each plane. Also, Fig. 5.22 shows the error distribution of E_ϕ-component at $\phi = \frac{\pi}{2}$ plane using three and four measurement spheres. It can be noticed, in the case of three measurement spheres that, the error is high in the regions between these spheres. As an example, the error is larger than 0.25 db in the regions $30° \leq \theta \leq 60°$ and $120° \leq \theta \leq 155°$ for E_θ-component as shown in Fig. 5.21. However, in the case of E_ϕ-component,

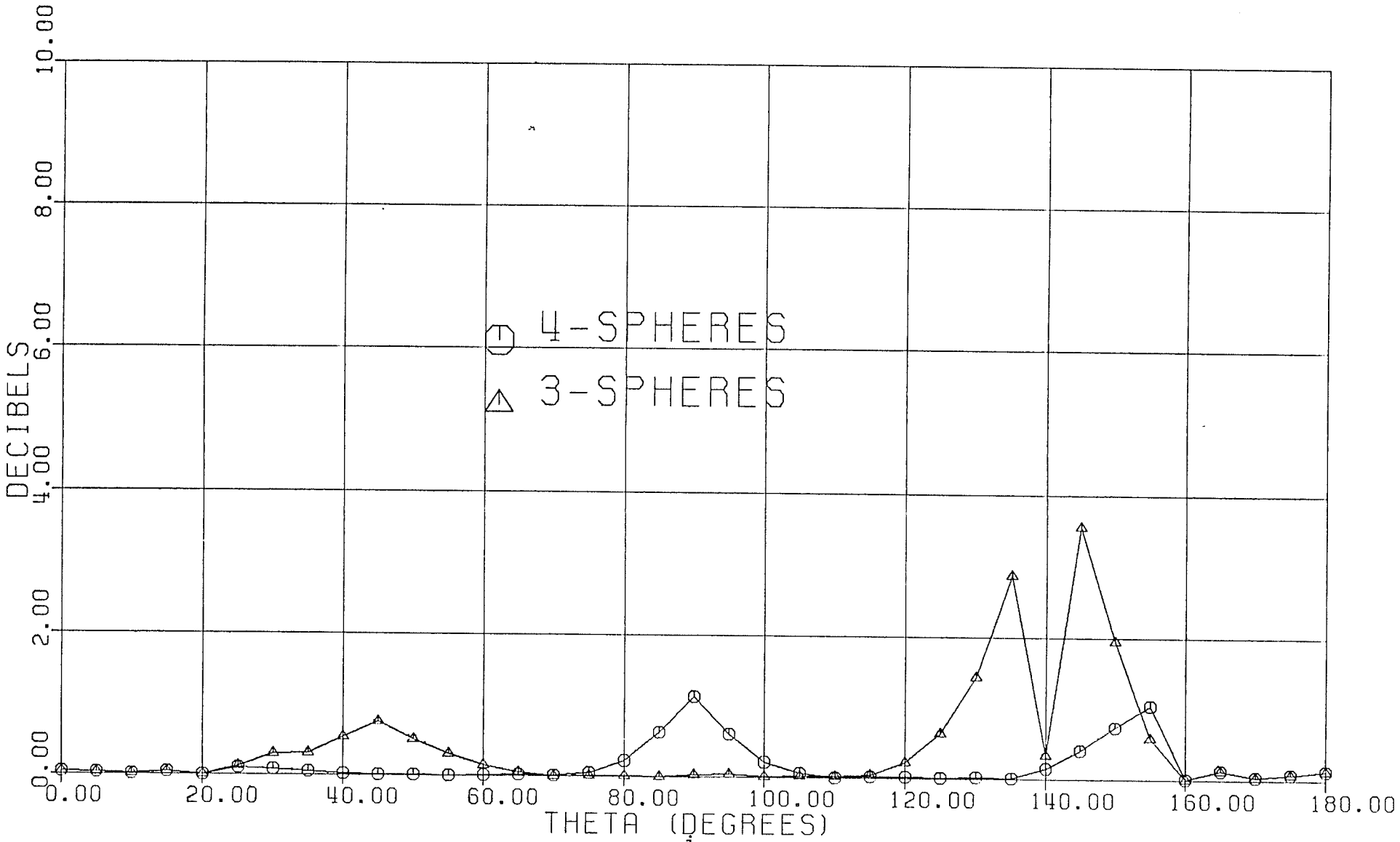

Fig. 5.21: The error in the calculated near-field of $|E_\theta^1|$ component using three and four measurement spheres, ϕ=0.

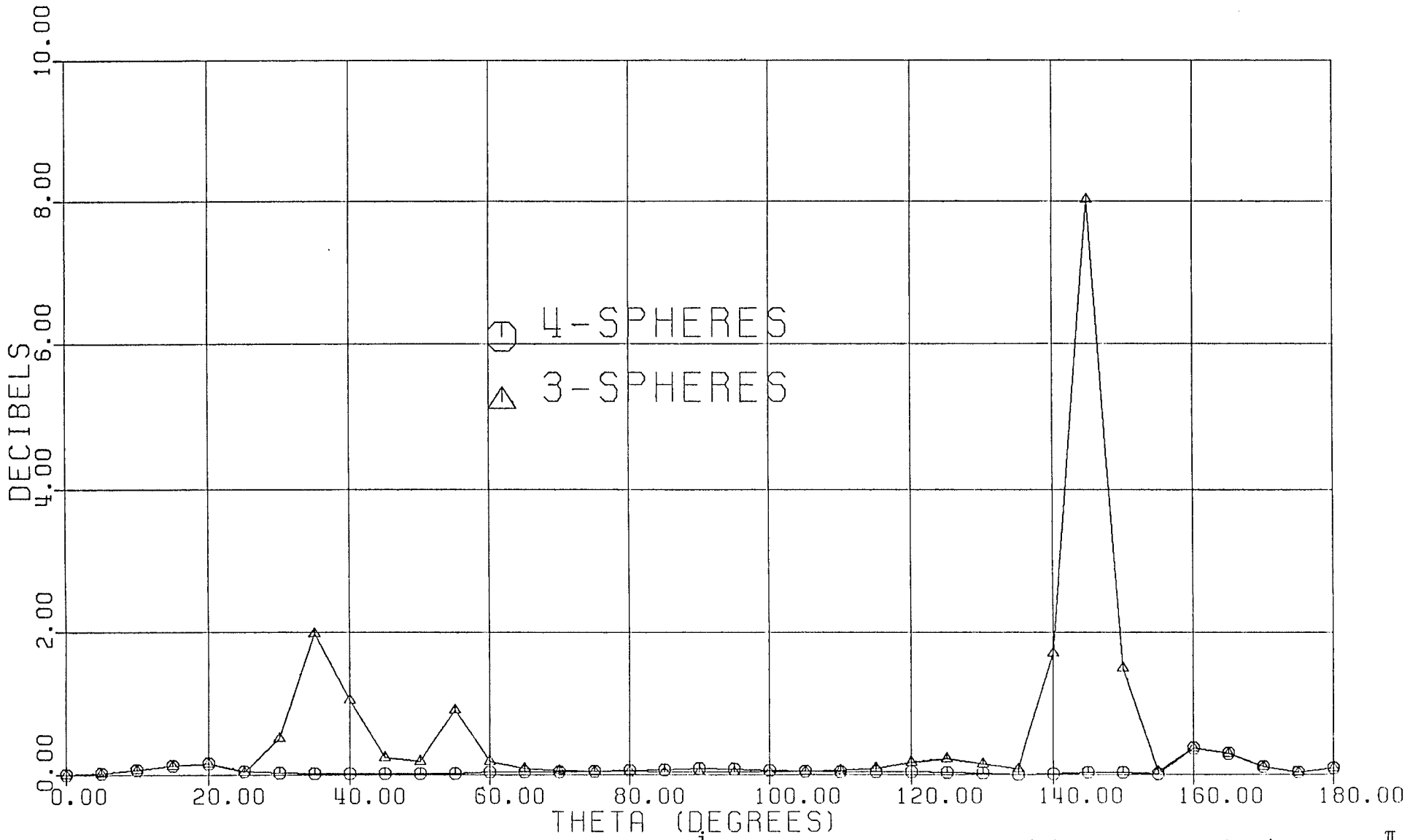

Fig. 5.22: The error in the calculated near-field of $|E^1_\phi|$ components using three and four measurement spheres, $\phi = \frac{\pi}{2}$.

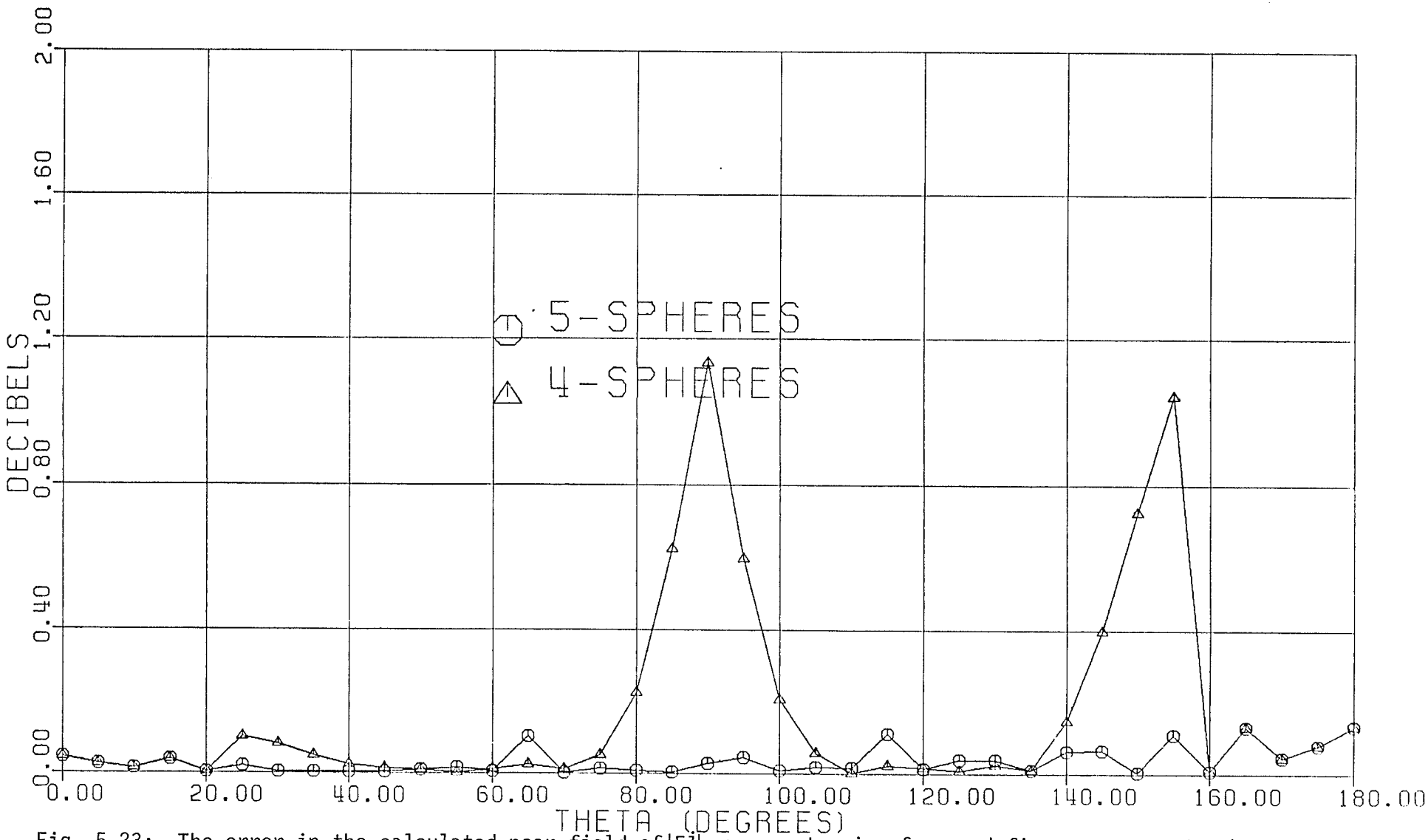

Fig. 5.23: The error in the calculated near-field of $|E_\theta|$ component using four and five measurement spheres, ϕ=0.

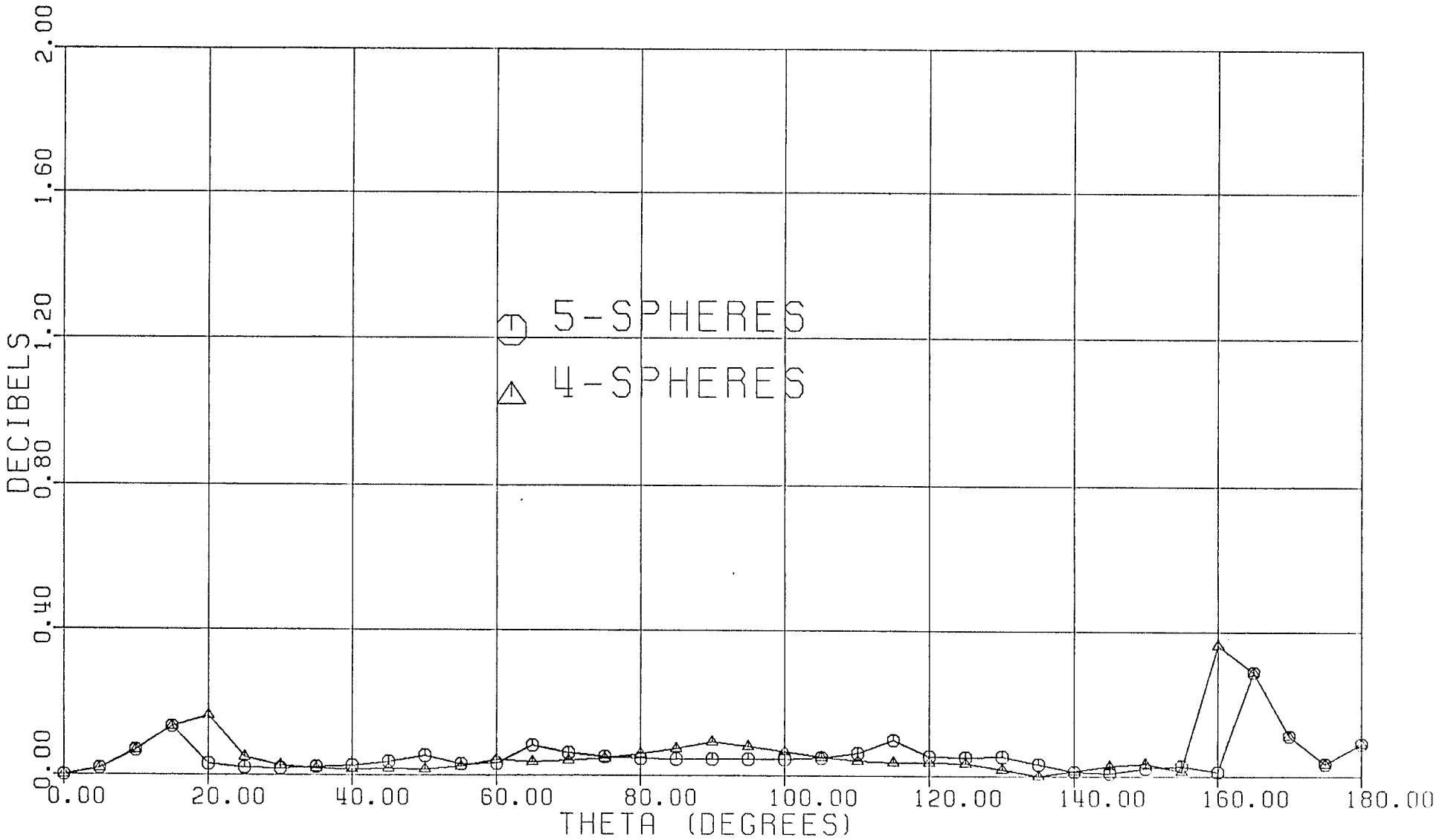

Fig. 5.24: The error in the calculated near-field of $|E^i_\phi|$ component using four and five measurement spheres, $\phi = \frac{\pi}{2}$.

these regions are $30° \leq \theta \leq 60°$ and $135° \leq \theta \leq 170°$ as shown in Fig. 5.22. The maximum error is 3.6 db for E_θ and 8.0 db for E_ϕ-components.

In the four measurement spheres case, the maximum error decreases to 1.0 db in E_θ and to 0.4 db in E_ϕ- components. Also the regions of inaccurate results are in the ranges of $80° \leq \theta \leq 100°$ and $140° \leq \theta \leq 155°$ for E_θ-component and $155° \leq \theta \leq 170°$ for the E_ϕ-component. The size of these regions decreases by about 50% if the number of measurement spheres increases from three to four. If more accurate results are required, it is recommended to use larger number of measurement spheres in each plane. This is evident from Figs. 5.23 and 5.24. These figures show that, the error decreases significantly in the case of five measurement spheres when compared to three and four spheres. As an example, in Fig. 5.23, the maximum error in E_θ-component in the five sphere case is less than 0.2 db, while it is more than 1.0 db in the four spheres case. Similar results are also evident from Fig. 5.24, where the error distributions in E_ϕ-component has decreased for five spheres case.

5.4.1.2 Numerical results for the radiation pattern of the isolated antenna

In this section, the calculated far-field radiation

patterns using the matrix and the integration methods are compared with the exact ones. Several cases are considered to examine the effect of inaccurate field on the surface S, which encloses the isolated antenna, on the far-field radiation pattern of that antenna. In this example, it is adequate to compute the tangential components E_θ and E_ϕ of the electric field on the surface S in only $\phi=0$ and $\phi=\frac{\pi}{2}$ planes. This is due to the fact that E_θ and E_ϕ components are known a priori to have $\cos\phi$ and $\sin\phi$ dependence, respectively.

In the first case, the near electric field is calculated on the surface S, with radius $k_0A=5.0$, by using three measurement spheres in each principal plane. This calculated field is used to calculate the radiation pattern of the isolated antenna by using the matrix and the integration methods described in section (4.4). Figs. 5.25 and 5.26 show the normalized magnitude and the phase of the far-field radiation pattern of the E_θ-component at $\phi=0$ plane, respectively. In both figures, 15 points are used from the calculated near-field on the surface S in the range of $0 \leq \theta \leq 180°$ to calculate the far-field radiation pattern of the antenna using both the matrix and the integration methods. The results have been compared with the exact ones in both of these figures. The result of the matrix method agrees well with the exact data in

the main lobe (Fig. 5.25). Their discripency is about 2.0 dbs in the back lobe, and about 3.0 dbs in the side lobes. The major disagreement is around the nulls. For the convenience of plotting in this figure and in all remaining figures, any magnitude less than -50.0 db is set at -50.0. On the same graph, in Fig. 5.25, the calculated far-field radiation pattern of the isolated antenna using the integration method is also shown. The error in the latter case is higher than the error in the results obtained by the matrix method using the same data. Fig. 5.26 shows the phase of E_θ-component at ϕ=0 plane. The maximum error in the calculated phase of the radiation pattern occurs in the region of side-lobes and around $60° \leq \theta \leq 120°$.

In the second case, an attempt is made to improve the accuracy of the far-field results by removing the inaccurate near-field data. In the regions between two measurement spheres $20° < \theta < 60°$ and $120° < \theta < 160°$, near-field data are inaccurate and they are excluded from the computation. As a result, only 11 data points on the surface S are utilized. Figs. 5.27 and 5.28 show the computed new amplitudes and phases. It is evident that the results of the integration method has deteriorated, but those of the matrix method are still reasonable. From these results, we conclude that the exclusion of the inaccurate data, does not

necessarily improve the accuracy of the field patterns.

In the third case, the near-electric field on the spherical surface S is generated by using four measurement spheres. In this case, the inaccurate data regions occur in the ranges of $80° < \theta < 100°$ and $140° < \theta < 160°$ as shown in Figs. 5.23 and 5.24. Figs. 5.29 and 5.30 show the far-field radiation pattern of the E_θ-component at $\phi=0$ plane using the data which is generated by four measurement spheres. In these figures, the calculated radiation patterns by the matrix method uses 14 points in the range of $0 \leq \theta \leq 180°$, excluding $\theta = 30°$, $90°$ and $150°$ points. The integration method in this case is using 19 equally spaced points with spacing $\Delta\theta=10°$. Figs. 5.29 and 5.30 show excellent agreement between the calculated and the exact radiation patterns in the main and the back lobe directions but some errors in the side lobe directions are noticeable. The maximum error occurs at the side lobes as shown in Fig. 5.29 and is about 1.0 db Also, the significant error in the phase of E_θ-component occurs in the range of $60° \leq \theta \leq 120°$ (Fig. 5.30).

In the fourth case, five measurement spheres are used to generate the near-electric field on the surface S which encloses the test antenna. The errrors in the magnitude of this generated data in comparison with the exact ones are

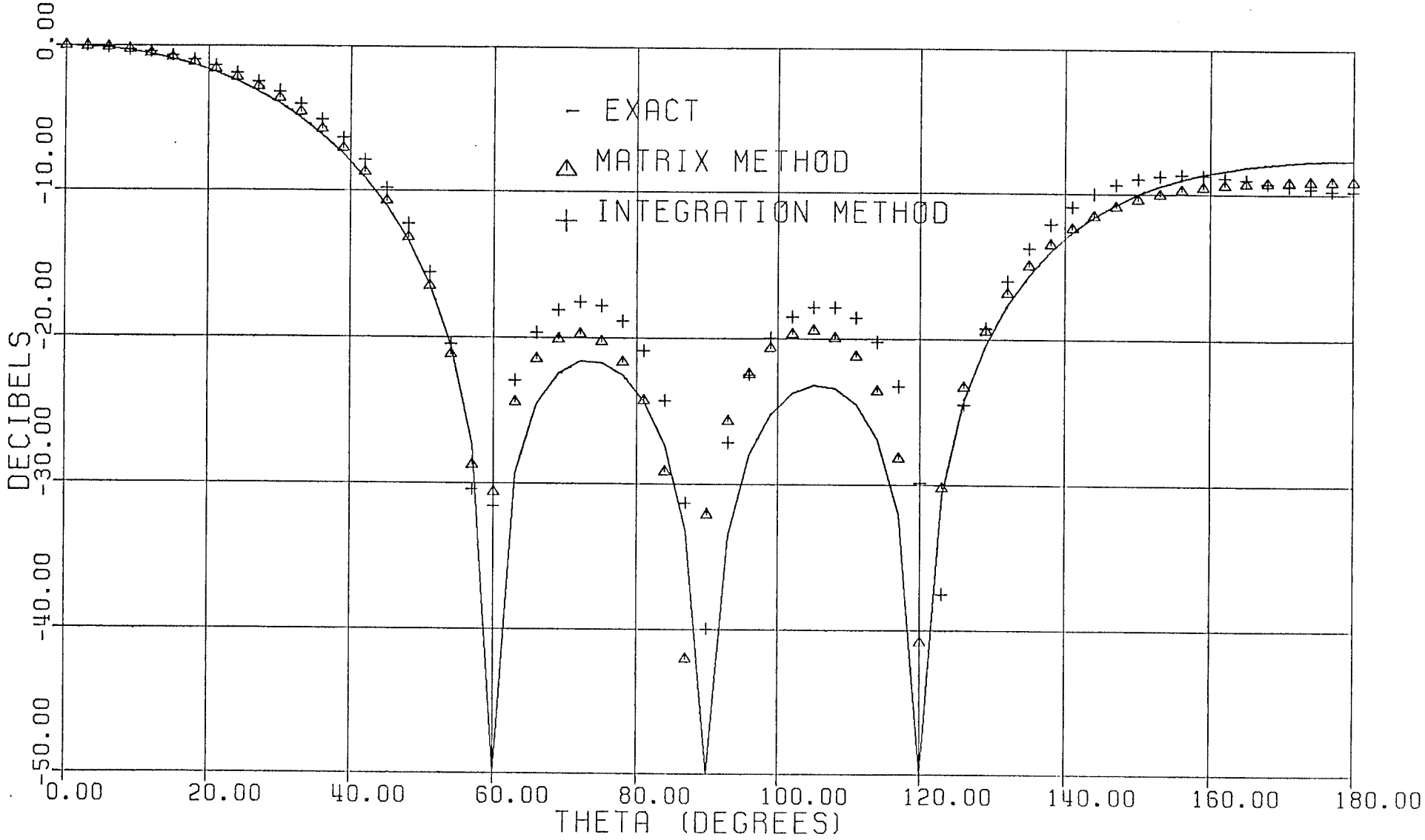

Fig. 5.25: Comparison of the calculated magnitude of E_θ^i with the exact one, four element dipole array, three measurement spheres, ϕ=0.

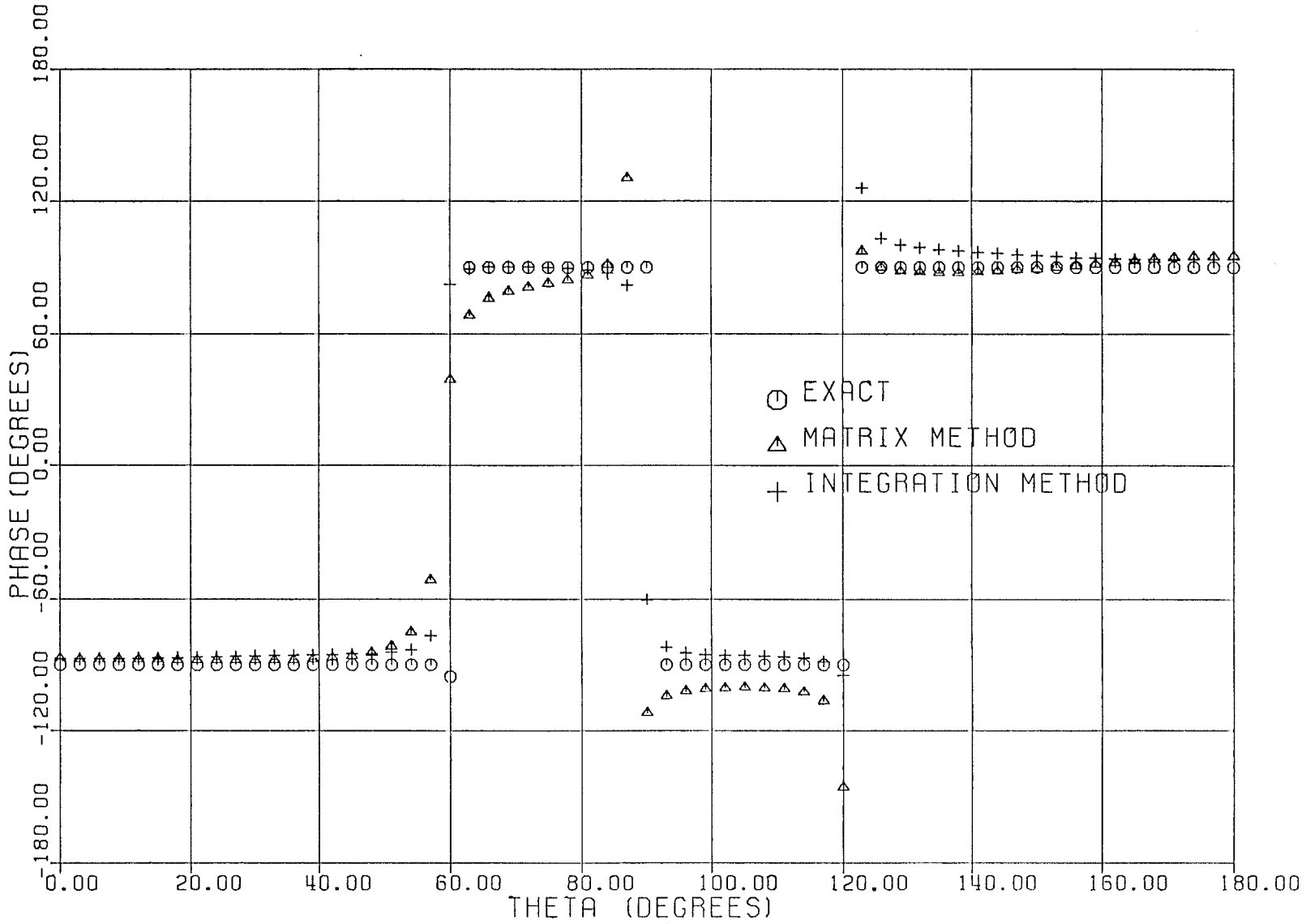

Fig. 5.26: Comparison of the calculated phase of E_θ^i with the exact one, four element dipole array, three measurement spheres, ϕ=0.

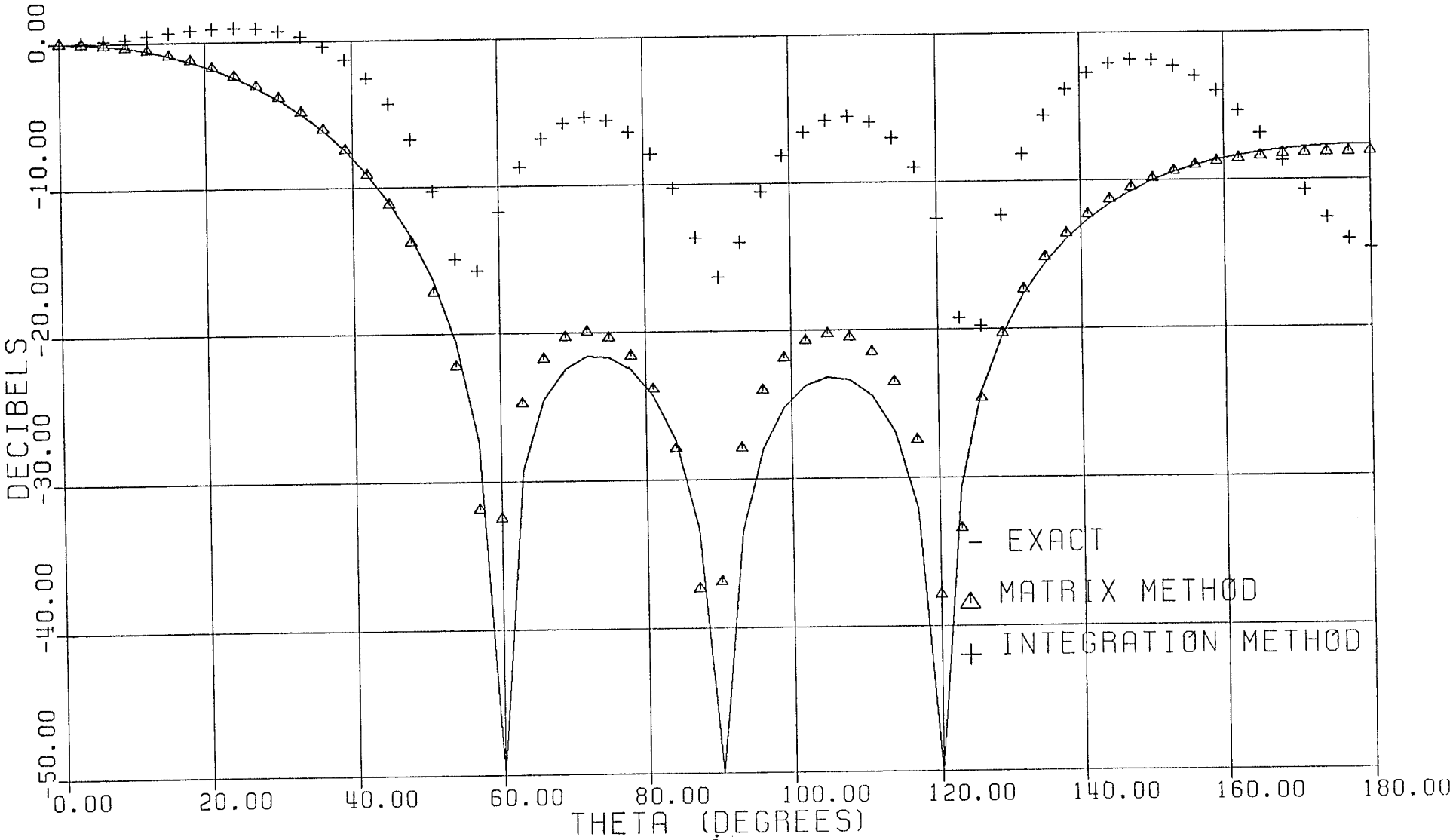

Fig. 5.27: Comparison of the calculated magnitude of E^i_θ with the exact one, four element dipole array, three measurement spheres excluding error regions, ϕ=0.

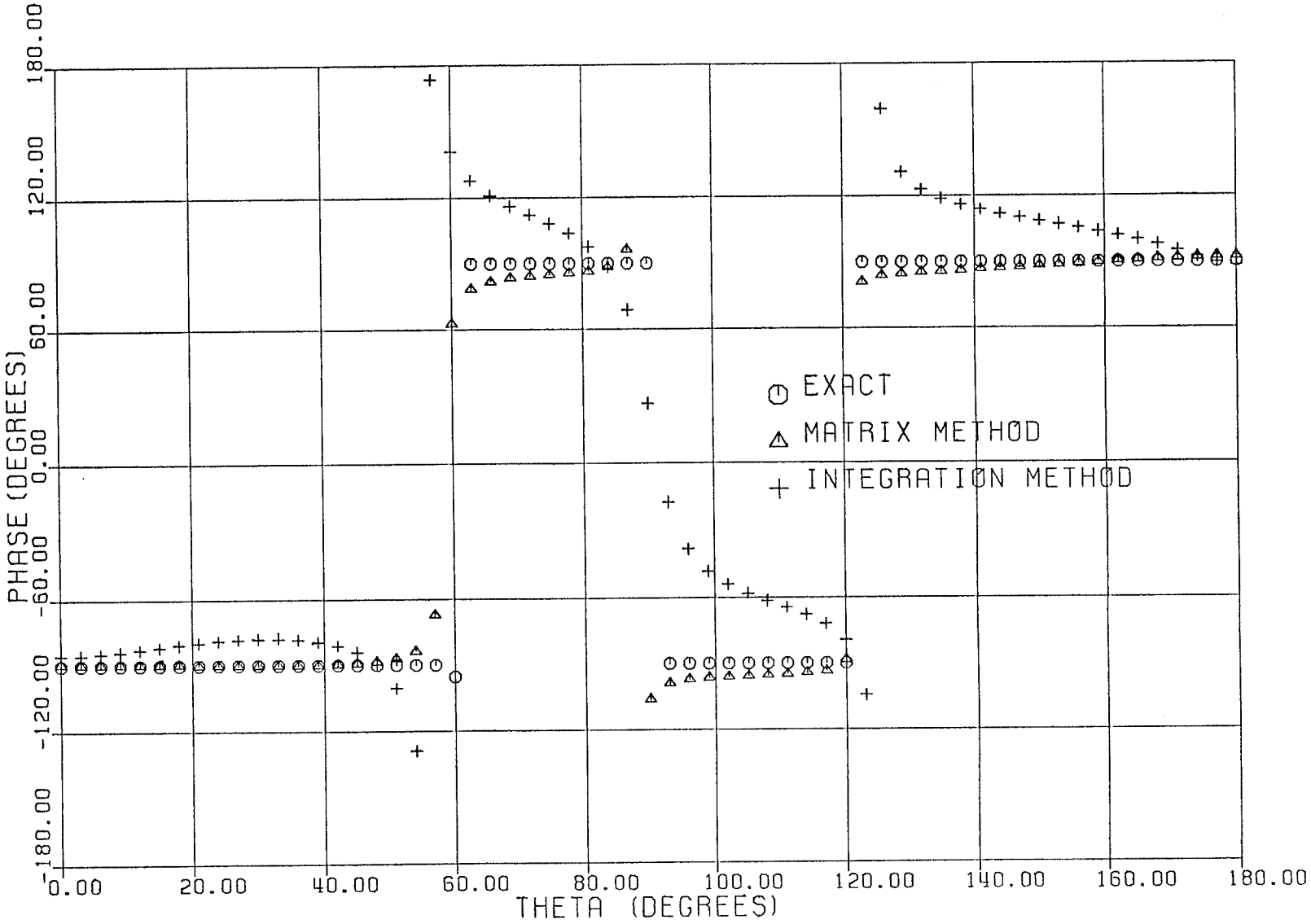

Fig. 5.28: Comparison of the calculated phase of E_θ^i with the exact one, four element dipole array, three measurement spheres excluding error regions, ϕ=0.

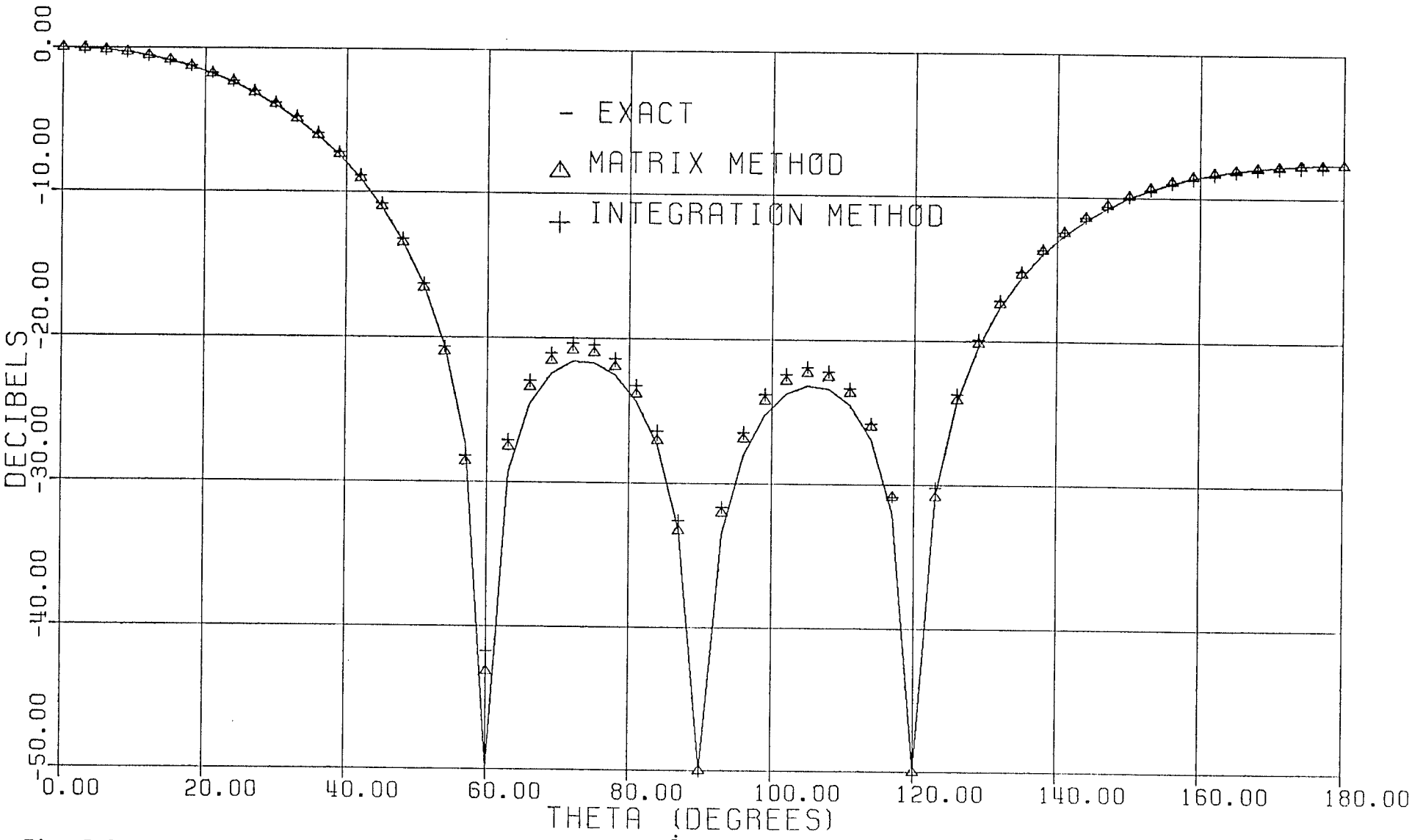

Fig. 5.29: Comparison of the calculated magnitude of E_θ^i with the exact one, four element dipole array, four measurement spheres, ϕ=0.

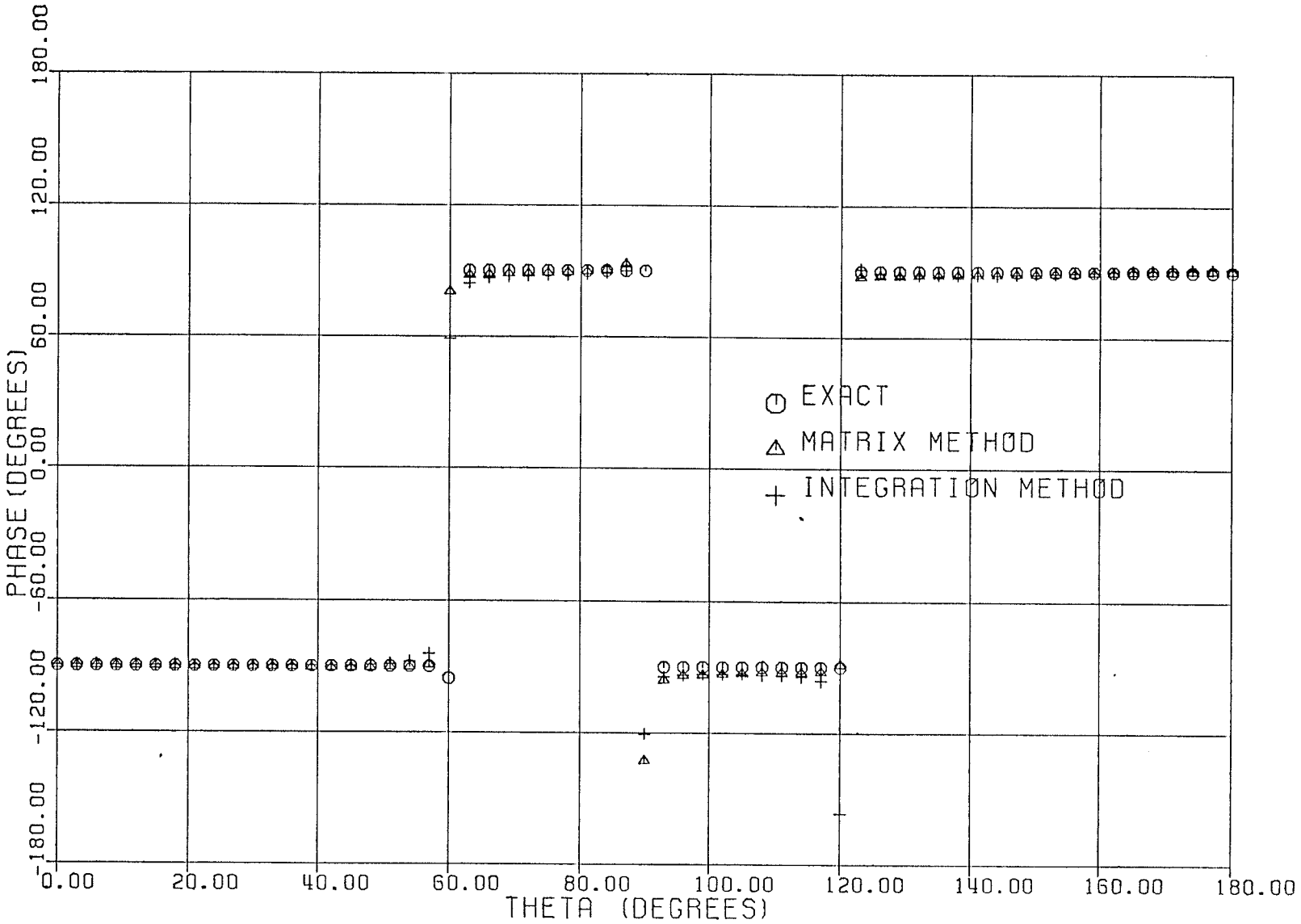

Fig. 5.30: Comparison of the calculated phase of E_θ^i with the exact one, four element dipole array, four measurement spheres, ϕ=0.

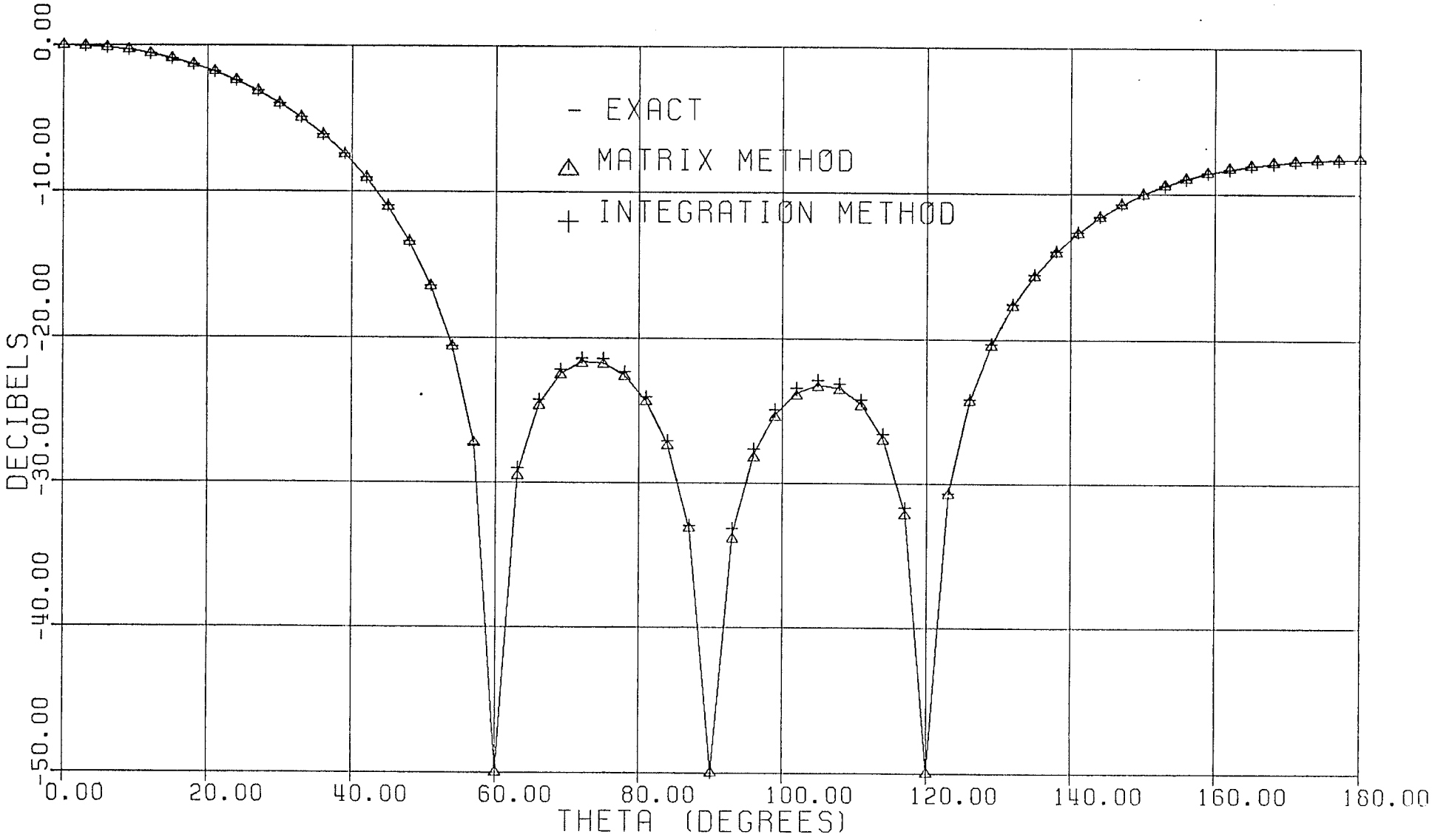

Fig. 5.31: Comparison of the calculated magnitude of E_θ^i with the exact one, four element dipole array, five measurement spheres, ϕ=0.

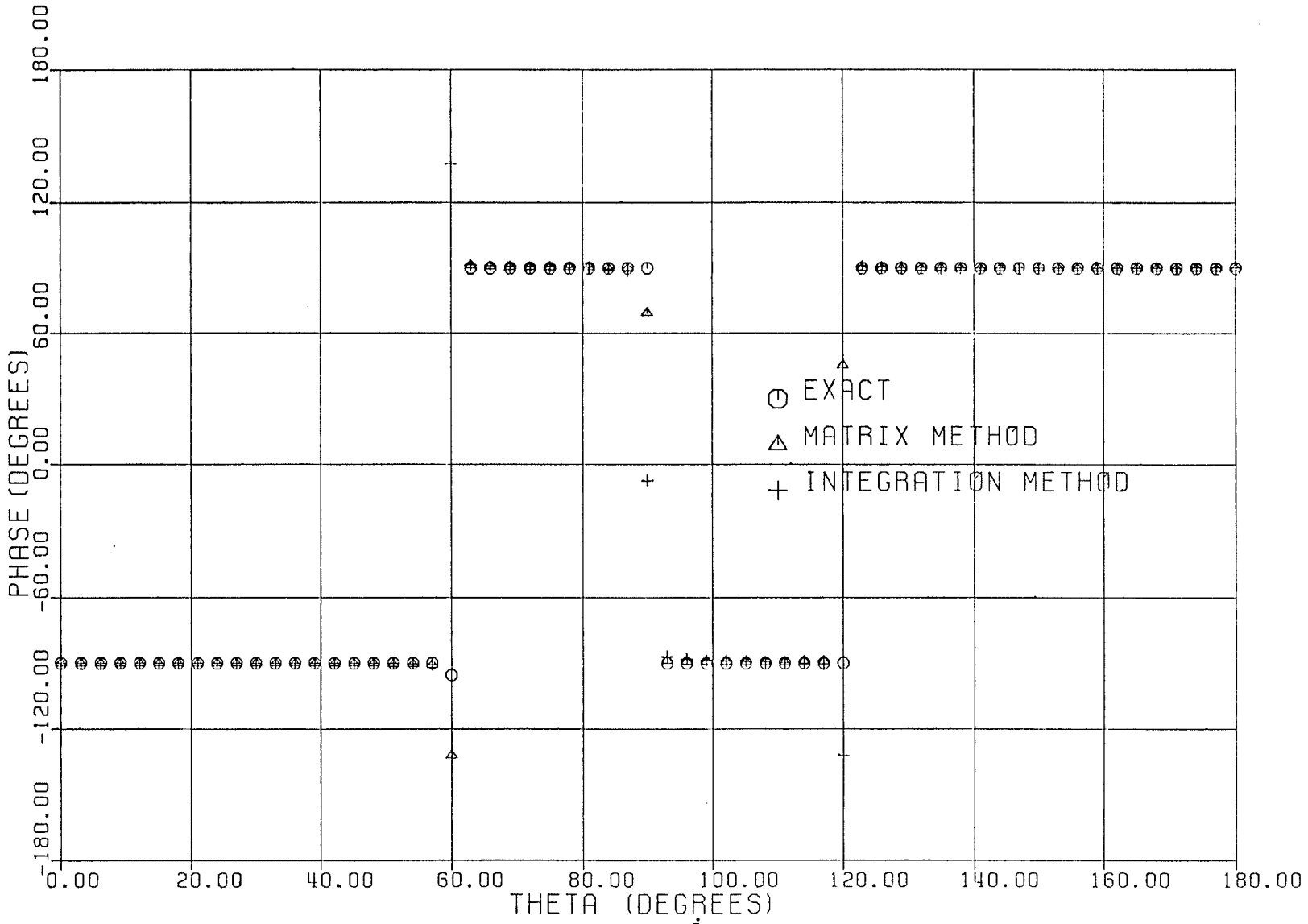

Fig. 5.32: Comparison of the calculated phase of E_θ^i with the exact one, four element dipole array, five measurement spheres, ϕ=0.

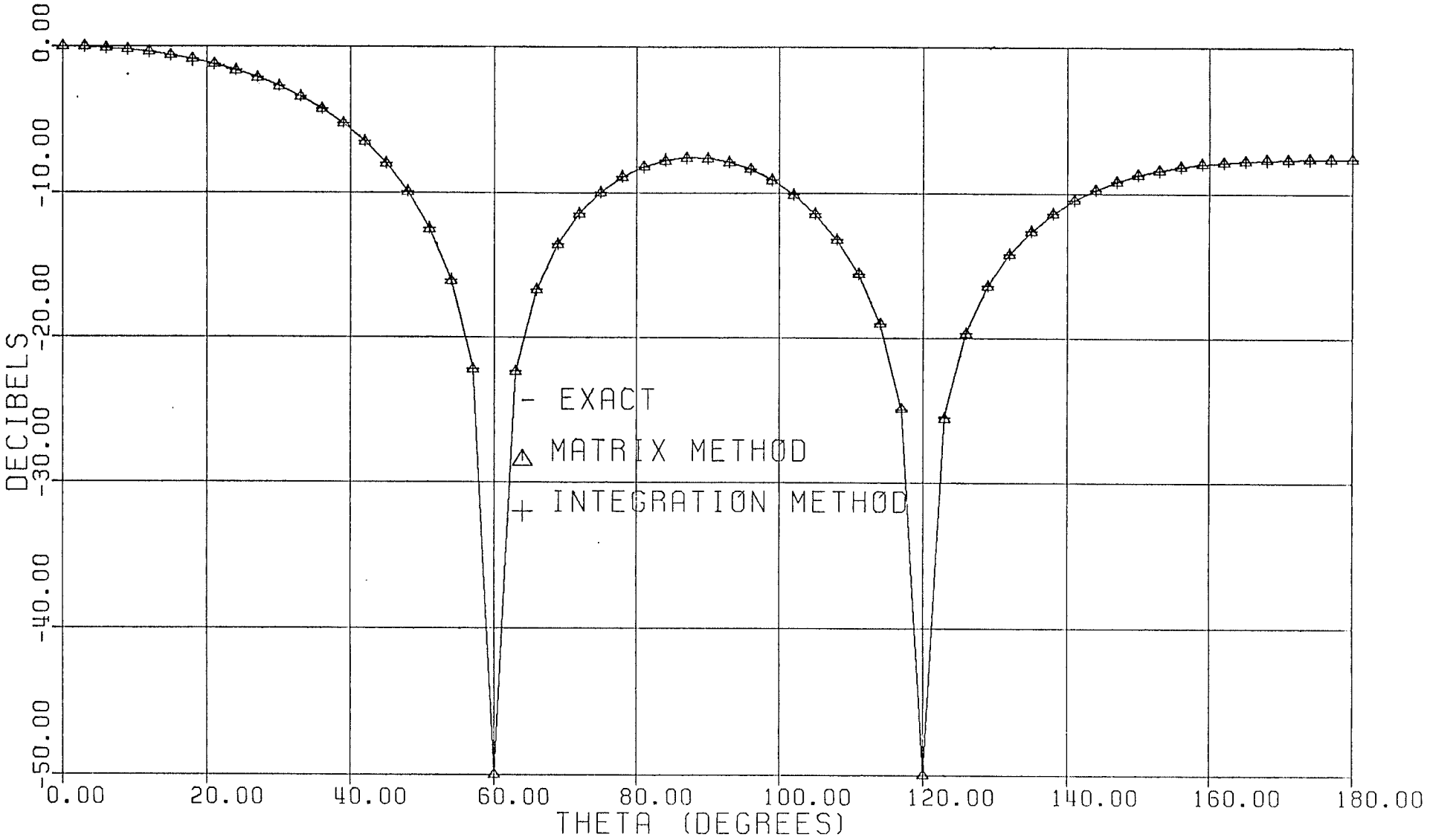

Fig. 5.33: Comparison of the calculated magnitude of E_{ϕ}^{i} with the exact one, four element dipole array, five measurement spheres, $\phi = \frac{\pi}{2}$.

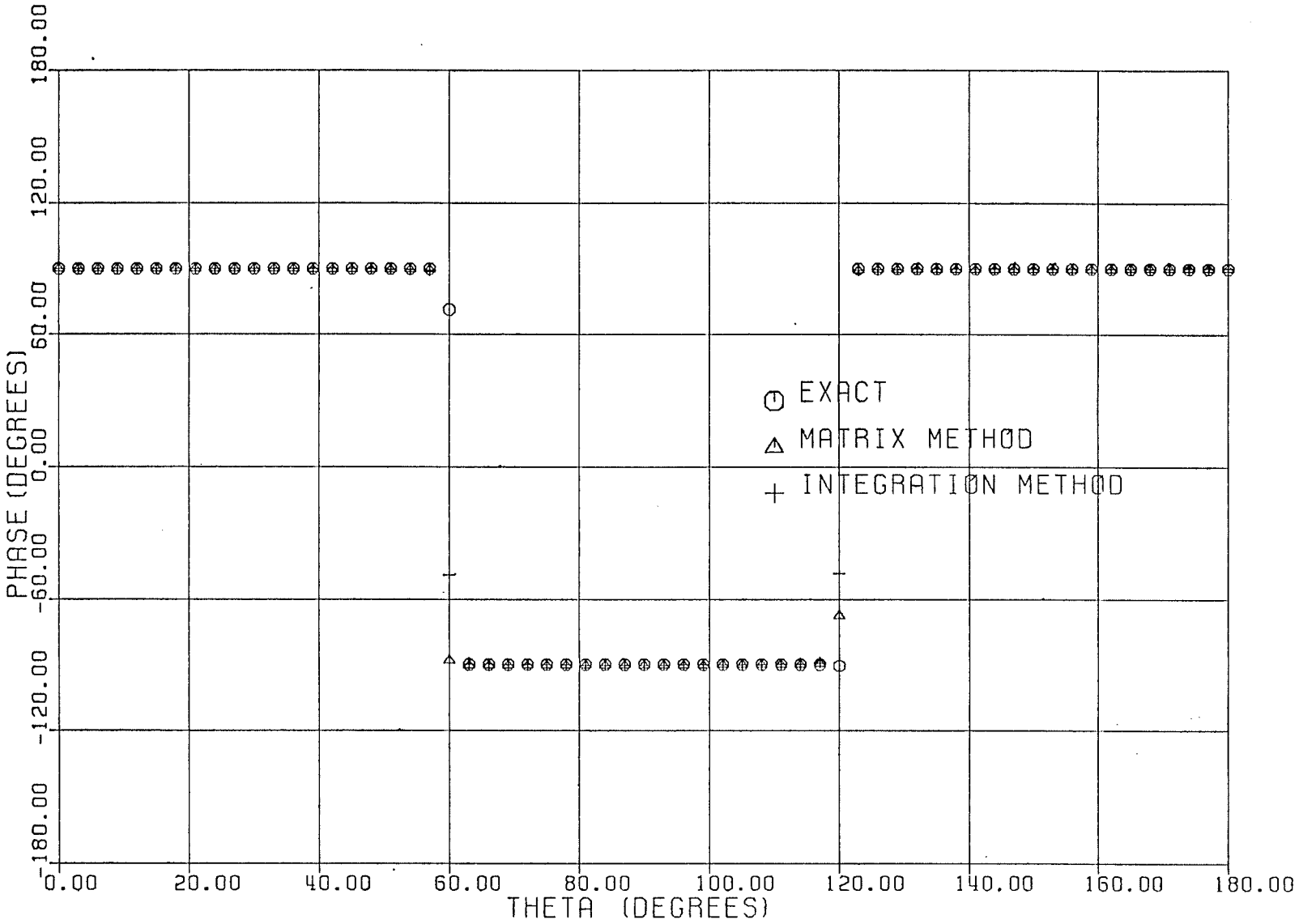

Fig. 5.34: Comparison of the calculated phase of E^i_ϕ with the exact one, four element dipole array, five measurement spheres, $\phi = \frac{\pi}{2}$.

shown in Figs. 5.23 and 5.24, respectively for the E_θ- and E_ϕ-components. These figures show significant improvement in the patterns over the previous cases. Figs. 5.31 and 5.32 show the magnitude and the phase of the far-field radiation pattern of E_θ-component at ϕ=0 plane. For this case, the magnitude and the phase of the other far-electric field component E_ϕ , at $\phi = \frac{\pi}{2}$ plane, are shown in Figs. 5.33 and 5.34. It is clear from these figures that, there is an excellent agreement between the calculated far-field and the exact ones in the main, back and side lobes of both E_θ- and E_ϕ-components.

5.4.2 Calculation of the Far-Field Radiation Pattern of the Test Antenna in the Presence of Spherical Scatterer

This case is very similar to the previous one for the field of the isolated antenna. The same example with the same parameters will be used. The only difference is to calculate the near-field on the surface S' which encloses both, the test antenna and the scatterer as shown in Fig. 5.20. The radius of the spherical surface S' is taken to be $k_o A' = 10.0$. Five measurement spheres are used to generate the total field on this surface and from which, the far-field radiation pattern for the combination of the antenna and the scatterer together will be calculated.

In this example, the dielectric sphere as well as the array elements is considered to be on the z-axis as shown in Fig. 5.20. The dielectric constant of this sphere is assumed to be ε_r=4.0.

Figs. 5.35 and 5.36 show the far-field radiation pattern of the magnitude and phase of E_θ-component of the antenna in the presence of the spherical scatterer using the matrix and the integration methods. In both figures the number of points used as input data on the spherical surface S' are 17 and 19 in the matrix and the integration methods, respectively. It is clear from both figures that, the matrix method has excellent agreement with the exact solution in both magnitude and phase. While the integration method gives good agreement in the main and the back lobes but gives large errors in the side lobes. By increasing the number of points in the integration method from 19 to 37, an excellent agreement is obtained. These results are shown in Figs. 5.37 and 5.38 for the magnitude and the phase of E_θ-component at ϕ=0 plane. Similar results are obtained for E_ϕ-component as shown in Figs. 5.39 and 5.40 for the magnitude and the phase of this component, respectively. The integration method generally requires more data points than the matrix method to give approximately the same results. In this example, the integration method required about 2.2 times as many data points as the

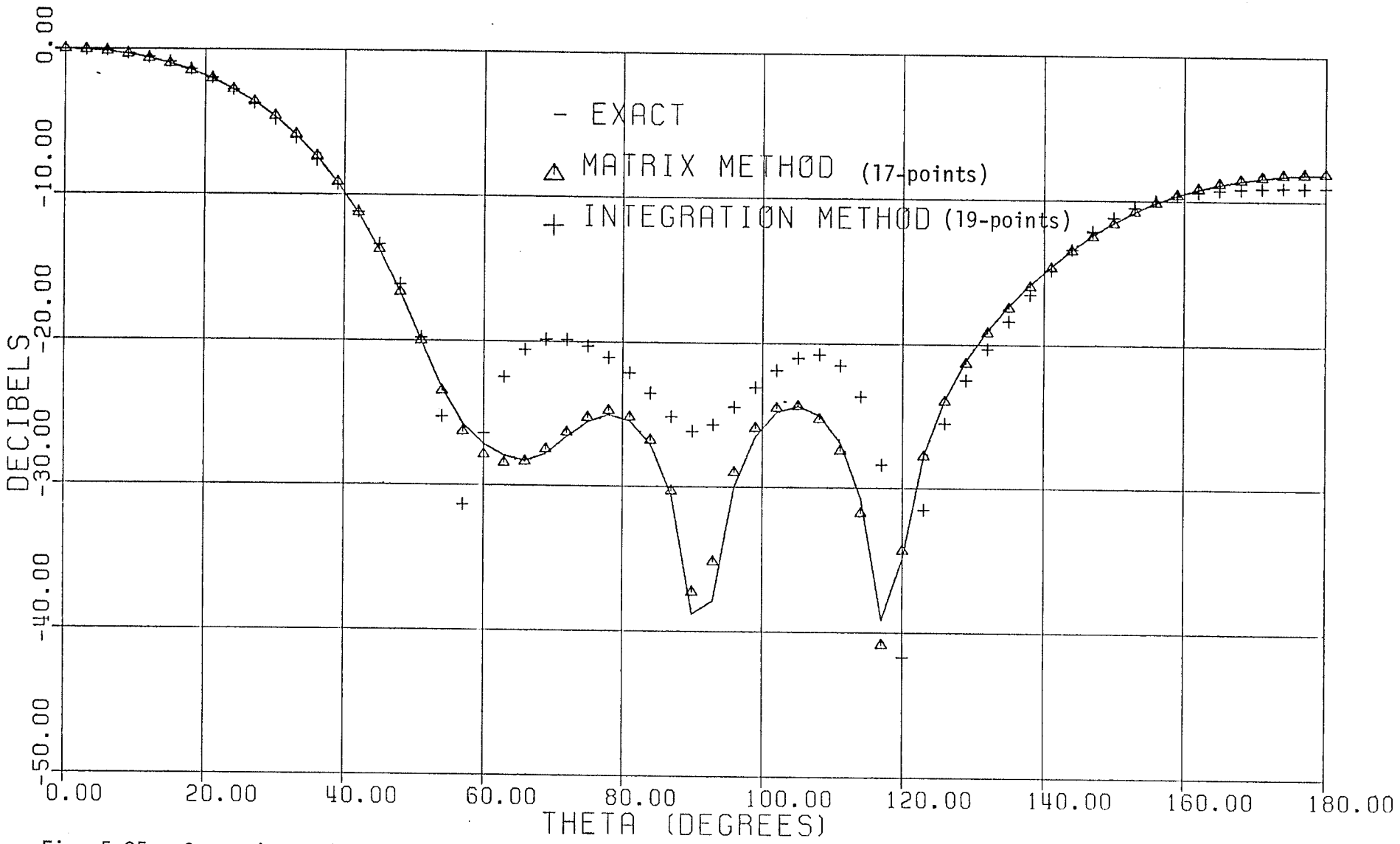

Fig. 5.35: Comparison of the calculated magnitude of E_θ with the exact one, four element dipole in presence of dielectric sphere, five measurement spheres, ϕ=0.

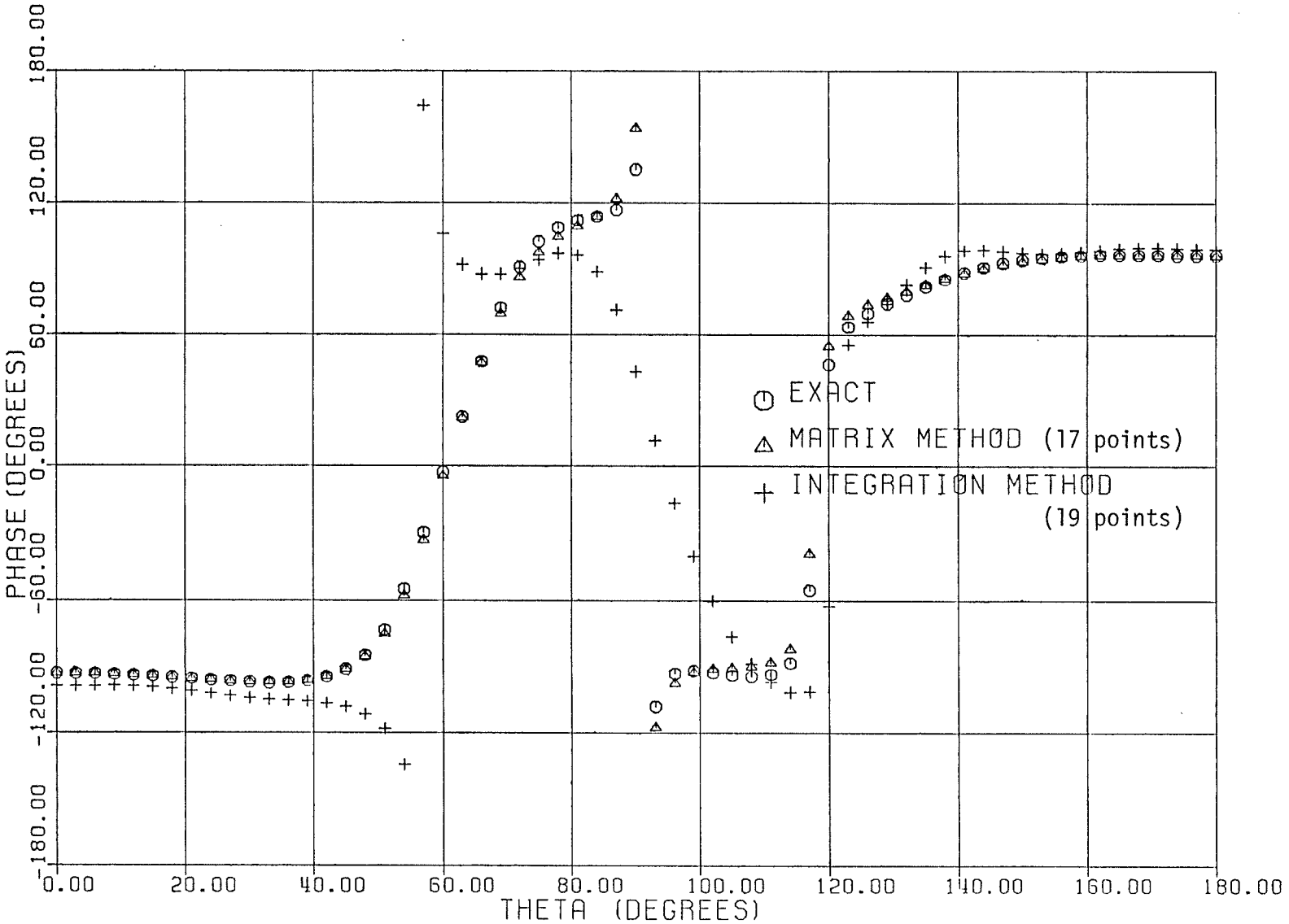

Fig. 5.36: Comparison of the calculated phase of E_θ with the exact one, four element dipole array in presence of dielectric sphere, five measurement spheres, ϕ=0.

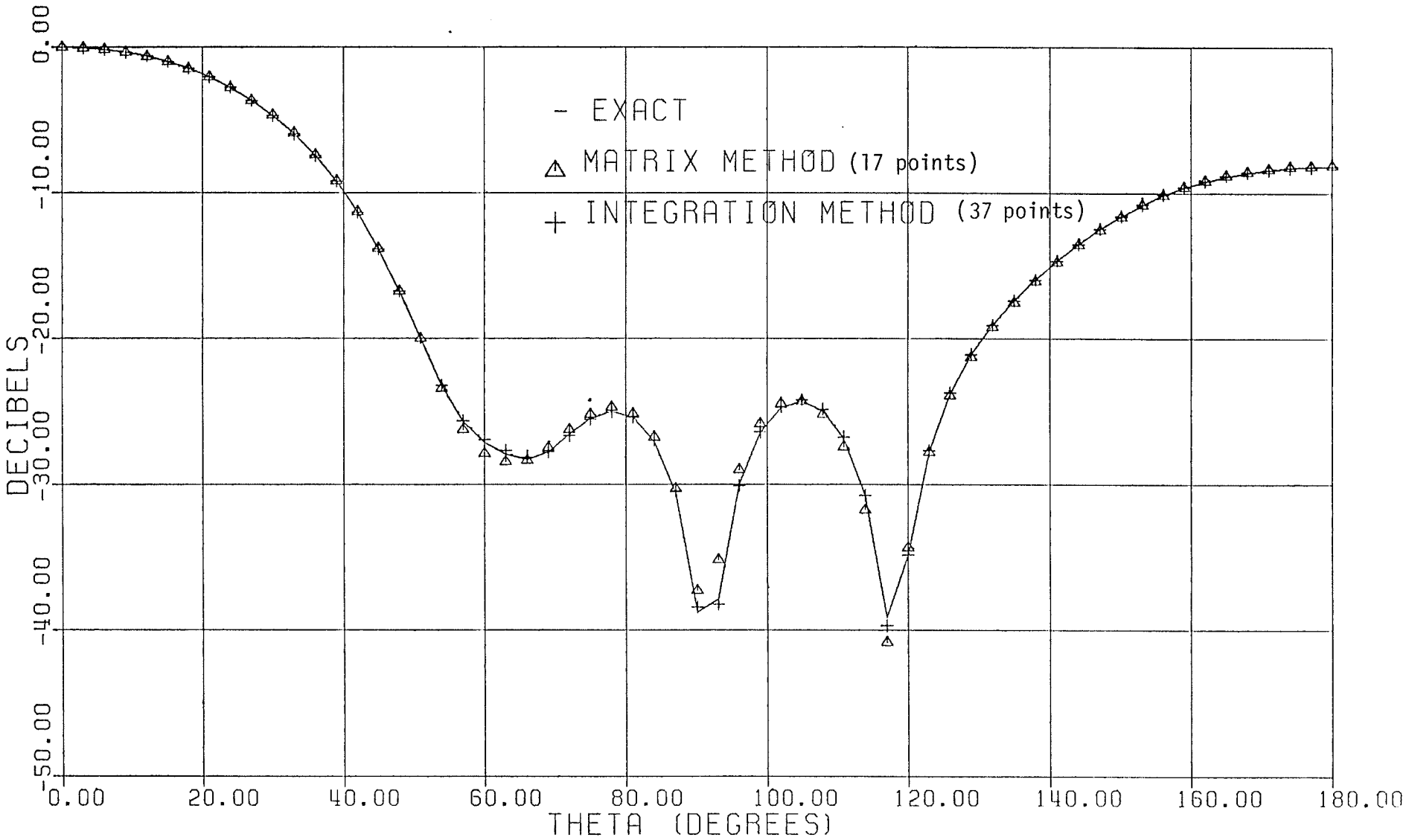

Fig. 5.37: Comparison of the calculated magnitude of E_θ with the exact one, four element dipole array in presence of dielectric sphere, five measurement spheres, ϕ=0.

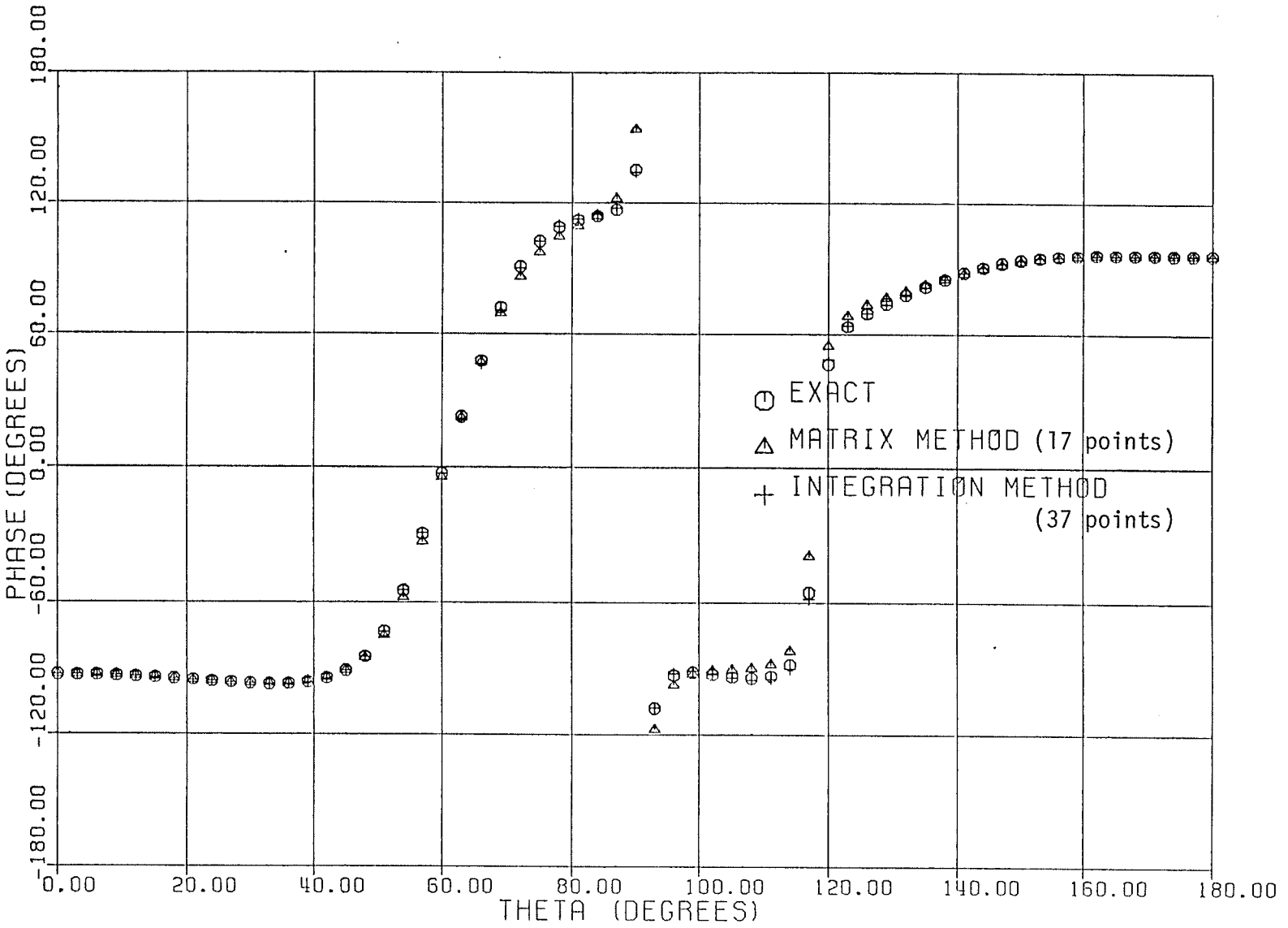

Fig. 5.38: Comparison of the calculated phase of E_θ with the exact one, four element dipole array in presence of dielectric sphere, five measurement spheres, ϕ=0.

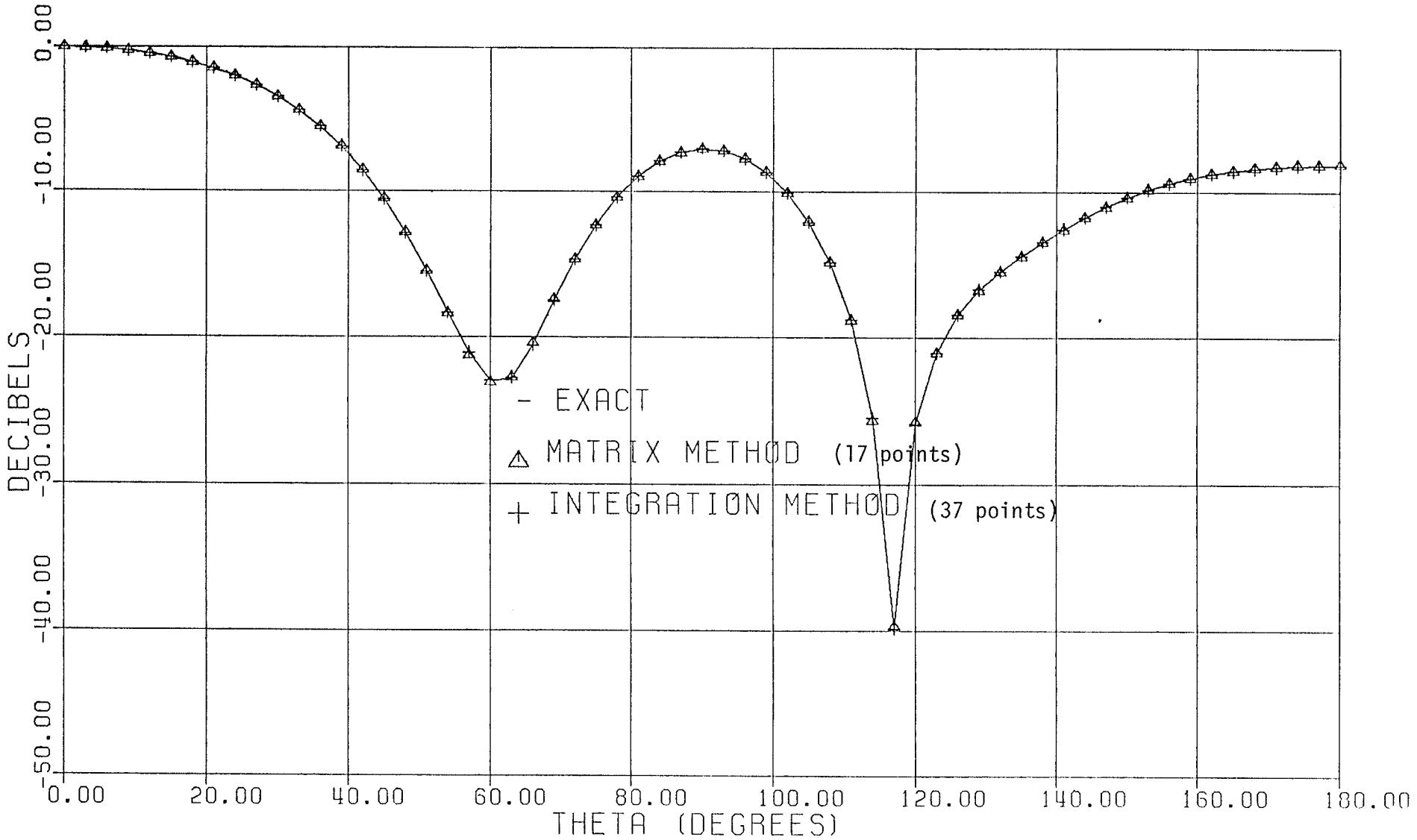

Fig. 5.39: Comparison of the calculated magnitude of E_ϕ with the exact one, four element dipole array in presence of dielectric sphere, five measurement spheres, $\phi = \frac{\pi}{2}$.

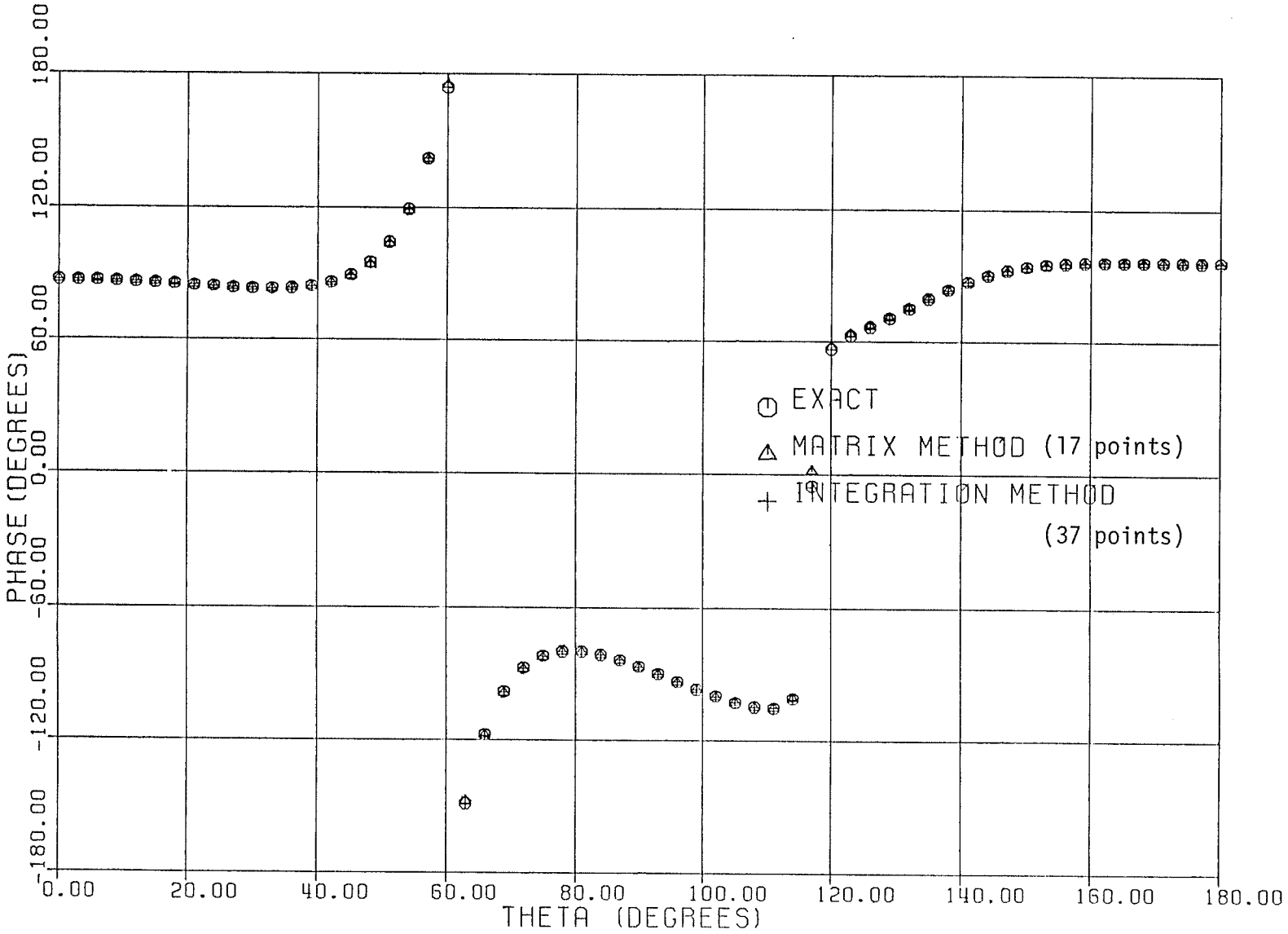

Fig. 5.40: Comparison of the calculated phase of E_ϕ with the exact one, four element dipole array in presence of dielectric sphere, five measurement spheres, $\phi = \frac{\pi}{2}$.

matrix method and agrees with similar results obtained in reference [34] for different examples.

5.5 DISCUSSIONS

In this chapter, the application of the field reconstruction using scattering data technique was investigated numerically. For the radiation source three different cases were considered, a plane wave, an electric dipole and a four-element electric dipole array. Considering any of these sources the field scattered by a specified dielectric sphere was obtained and was used together with the incident field to generate numerically the measurement data over specified measruement spheres. These measurement data were then used to obtain the field expansion coefficients within each expansion sphere. The calculated expansion coefficients were then used to reconstruct the initial source field. For various geometrical parameters, number of expansion spheres and their radii, the computational errors were computed and the accuracy of the reconstructed fields were studied in detail.

For the plane-wave, the convergence of the spherical expansion series of the reconstructed incident electromagnetic fields were investigated numerically. It was found for this case that, the expansion function series of the

reconstructed electric field is convergent to the exact solution with accuracy better than 0.01% if the truncation order satisfied the condition $N>2k_oA>2k_oa$, where a and A are the radii of dielectric and measurement spheres, respectively. In this case, the optimum distribution of the measurement points were used.

For the second source, an electric dipole, the reconstructed data were used to study the convergence of the spherical expansion series, to investigate the dependence of the spherical expansion series on the location of the dipole and to compare the accuracy of the reconstructed field with and without optimal distribution of the measurement points. It was found that, if the measurements are carried out over a measurement sphere at a larger distance from the source, the convergence of the series is faster and a smaller number of coefficients needs to be computed. This essentially means that a smaller number of measurements are to be carried out. In other words, to obtain a given degree of accuracy, in the calculated electromagnetic field using scattering data technique, it is better to scan the receiving probes far from the test antenna. This result is significant from the measurement point of view. It was also found that, the calculated fields using spherical wave expansion and non-optimum distributions of the θ-locations still converge to the exact solution. However,

a larger number of spherical harmonics were needed in this case than the optimum distribution case. This result is also important from the experimental point of view. Since in some cases, it may not be convenient to position the receiving probes at the optimum locations dictated by the optimization function of Equation (4.26). These results indicated that with non-optimum measurement points, accurate results can still be obtained provided that the conditions of Equations (5.16) are satisfied. This is very important for cases where, for practical reasons, one utilizes several fixed probes. The selection of non-optimum distribution of measurement points, however, reduces the accuracy of the results for a given number of spherical harmonics. This is the price which one normally will pay for the convenience of non-optimal distribution of the receiving points.

For the third case, a four element electric dipole array, the near-field of this source was calculated using the stepwise measurement technique of chapter four. Also, the same technique was utilized to evaluate the near-field of the same array in the presence of a dielectric sphere. In both cases, different number of measurement spheres were utilized. From these calculated near-field, the far-field radiation pattern of the isolated antenna and the antenna in the presence of a dielectric sphere were calculated. The calculated radiation patterns were compared with the exact one in three, four

and five measurement spheres cases. It was found from the numerical results that, when the number of measurements spheres is larger, the calculated near-and far-fields were more accurate. It was also concluded from the result of this case that, in the spherical near-field far-field transformation, the point matching technique (matrix method) requires less data points than if the integration method is used to give approximately the same accuracy. In the specific example which was mentioned in section 5.4, the integration method required roughly 2.2 times as many data points as the matrix method. This result agrees well with similar one obtained for different examples cited in reference [34].

CHAPTER VI

SUMMARY, CONCLUSIONS AND SUGGESTIONS FOR FUTURE WORK

6.1 SUMMARY AND CONCLUSIONS

A technique for reconstructing fields using scattering data was developed in this thesis. The problem consisted of using a dielectric scatterer; e.g., sphere (or cylinder), in the vicinity of the antenna whose radiation field is unknown. This technique can be used to calculate the near-field of the isolated antenna, or, of the antenna in the presence of the scatterer on a surface enclosing only the antenna or both antenna and the scatterer from measurements of the total field near the scatterer. From the calculated near-field, the far-field radiation pattern of the isolated antenna, or, the antenna and the scatterer combination can be determined. The problem has practical significance since dielectric scatterers are used to shape the radiation patterns of horns, waveguides and other radiating systems. Dielectric scatterers are also used to scatter the primary field of the antenna. In this manner, the wide angle scattering increases the signal strength in the regions of weak primary field and facilitate the accurate measurement of the near-field especially for the high gain antennas. In addition, this improvement of the field strength enables

one to carry out the field measurement on a larger surface than it is normally feasible.

When the spherical surface, enclosing both dielectric sphere and the antenna is small in size, the measurement can be carried out over this surface to obtain the total field. In addition, the field outside this spherical surface can be described by spherical wave functions with unknown coefficients. These unknown coefficients can then be obtained by matching the measured and the spherical wave expansion fields over the spherical surface which encloses the antenna and the scatterer. On the other hand, when the antenna, or its separation distance from the scattering sphere is large, the spherical surface enclosing them also becomes large. The measurement of the field over such a large surface requires large scanning system, which is practically undesirable. To utilize a small scanning system, the proposed stepwise measurement approach which is developed in this thesis, can be used and will be summarized here.

In this system, the measurements are carried out over small spherical surfaces near the antenna which are named measurement spheres. The results are then used to compute the field over a spherical surface, which encloses only the antenna or both antenna and the scatterer. The required

field outside this surface can therefore be obtained by the above spherical expansion approach.

To obtain the field over such surfaces, the following steps were used:

1. An expansion sphere was defined which enclosed the scatterer and one of the measurement spheres and was tangent to the antenna surface. The field inside the scattering sphere and between its surface and the surface of the expansion sphere were described by spherical wave functions with unknown coefficients. These unknown coefficients were obtained by matching the calculated and the measured field over the surface of the measurement sphere.
2. Within second, third and the remaining expansion spheres which enclosed one of the other measurement spheres, fields were also described by spherical wave functions about the origin of each surface and their unknown coefficients were found after the matching of their respective fields.

Following these steps, the total fields which were then known within each expansion sphere were used to calculate the required field components over the spherical surface which enclosed the isolated antenna, or, the antenna and the

scatterer. Note that, the expressions for the field inside second, third, and the remaining expansion spheres could be determined from the expressions of the field inside the first one, by replacing the dielectric constant with unity. The problem therefore reduced to the evaluation of the unknown field coefficients for the field inside the first expansion sphere, which enclosed the scatterer, and to the calculation of the required field components over part of the required surface which fell within the expansion sphere.

In chapter two, a review of the important antenna measurement techniques which are normally used to test an antenna were presented. Three different measurement methods were; the plane-wave, the focusing and the near-field probing. Each method was described in some detail and its advantage and limitations were given.

The mathematical modelling and solution for this problem in two and three-dimensional cases were developed in detail in chapters three and four, respectively.

Chapter three presented the solution of two-dimensional inverse source problems. The theoretical analysis was presented only for the transverse magnetic (TM) fields but

a similar analysis could be carried out for transverse electric (TE) or any general two-dimensional fields. The specific problem consisted of an unknown incident field and a dielectric cylinder which scattered the incident field. To formulate the problem, cylindrical wave functions were used to represent the incident, the scattered and the total fields. Boundary conditions were applied to obtain a matrix relationship between the coefficients of the unknown incident field and those of the total field. This formulation was used to study the effects of the number of cylindrical wave functions, angular range of measurement points and inaccuracies in the measurement data, on the accuracy of the incident field reconstruction. Comparing the reconstructed data with the exact one, it was found that to retain the maximum error to less than 0.5%, the number of cylindrical functions N in the series must satisfy the relationships $N \geq 3k_0a$ and $N \geq 1.5\ k_0A$, where a and A were the radii of the dielectric and measurement cylinders, respectively.

The effect of angular range of the measurement points on the accuracy of the results was also studied. It was found that limiting the measurement points to a range less than $0° \leq \phi \leq 180°$ reduced the accuracy of the reconstructed field. However, the decrease in the accuracy was negligibly small, as long as, the measurement range was retained between

45° and 135°. Further reduction of the measurement range deteriorated the accuracy at an accelerated rate.

Also, the measurement inaccuracies were simulated by modifying the exact data by a small percentage in a random manner. It was found that inaccurate data in only the magnitude, or, the phase of the measured field affected its respective reconstructed data of the incident field by a larger percentage. An error in magnitude of the measured field, introduced larger error in the amplitude of the reconstructed field than in its phase. Furthermore, an error in the phase caused more severe effect on the results than an error in the magnitude. The most interesting results were however found in introducing errors in both amplitude and the phase of the measurement data. The investigation showed that introducing errors in both amplitude and the phase has much smaller effect on the accuracy of the reconstructed field than introducing these errors in only the phase.

In chapter four, the theory of three dimensional field reconstructions using scattering data technique was presented. A stepwise approach to carry out the measurement over several small measurement spheres was also discussed.

A method of analysis and a solution of this problem was also presented. The calculation of the far-field radiation pattern using these techniques was then summarized.

In chapter five, the application of three dimensional field reconstructions using scattering data technique was investigated numerically. For the radiation source, three different cases were considered, a plane wave, an electric dipole and a four-element electric dipole array. Considering any of these sources the field scattered by a specified dielectric sphere was obtained and was used together with the incident field to generate numerically the measurement data over specified measurement spheres. These measurement data were then used to obtain the field expansion coefficients within each expansion sphere. The calculated expansion coefficients were then used to reconstruct the initial source field. For various geometrical parameters, the number of expansion spheres and their radii, the computational errors were computed and the accuracy of the reconstructed fields were studied in details.

The stepwise measurement technique was utilized successfully to evaluate the near-field on spherical surface enclosing a four-element electric dipole array, or, the same array in the presence of a dielectric sphere. In both cases,

different number of measurement spheres were utilized. From the calculated near-field, the far-field radiation pattern of the isolated antenna and the antenna in the presence of a dielectric sphere were also calculated. The calculated radiation patterns were compared with the exact ones using three, four and five measurement spheres. It was found from the results of the numerical investigation that, when the number of measurement spheres is large, the calculated results were more accurate. Also, it was concluded for spherical near-field far-field transformation, which was utilized in the above example that, the point matching technique (matrix method) required less data points than the integration method for a given accuracy.

In the same chapter, the reconstructed data for an electric dipole source was used to study the convergence of the spherical expansion series, to investigate the dependence of the spherical expansion series on the location of the source and to compare the accuracy of the reconstructed field with and without optimal distribution of the measurement points. It was found that, if the measurements are carried out over a measurement sphere at a larger distance from the source, the convergence of the series is faster and smaller number of coefficients needed to be computed. This, of course, means that smaller number of measurements need to be

carried out. In other words, to obtain the given degree of accuracy, in the calculated electromagnetic field using scattering data technique, it is better to scan the receiving probes far from the test antenna. It was also found that, the calculated fields using spherical wave expansion and non-optimum distributions of the receiving probe locations still converge to the exact solution. However, a larger number of spherical harmonics were needed in this case than the optimum distribution case.

6.2 SUGGESTIONS FOR FUTURE WORK

Some useful topics for future investigation would be the following extensions of the work presented here.

1. To apply field reconstruction using scattering data technique to different fields, e.g., ultrasound, X-ray, nuclear fields, lasers, etc.
2. To study the interaction between the test antenna and the scatterer.
3. To design on-line automated measurement set up using the technique described in this thesis.
4. To use planar scanning system and plane-wave near-field far-field transformation for the problem of

spherical scatterer to facilitate the measurements from practical point of view.

5. To apply the same technique to reconstruct the field of an antenna in presence of a different scatterer shape, e.g., thin discs, finite length cylinders, spheroids, etc.

REFERENCES

[1] J.D. Dyson, "Measurement of near-fields of antennas and scatters", IEEE Trans. Antennas Propag., Vol. AP-21, pp. 446-460, July 1973.

[2] R.C. Johnson, H.A. Ecker and J.S. Hollis, "Determination of far-field antenna patterns from near-field measurements", Proc. IEEE, Vol. 61, pp. 1668-1694, Dec. 1973.

[3] G. Sinclair, "Theory of models of electromagnetic systems", Proc. of the I.R.E., Vol. 36, pp. 1364-1370, Nov. 1948.

[4] J.S. Hollis, T.J. Lyon and L. Clayton, Microwave Antenna Measurements, Scientific-Atlanta, Inc., Atlanta, Georgia, USA, 1970.

[5] IEEE Standard Test Procedures for Antennas, IEEE Std. 149-1979, Published by Institute of Electrical and Electronics Engineers, Inc., New York, 1979.

[6] H. Jasik, Antenna Engineering Handbook, McGraw-Hill Book Co. Inc., New York, 1961.

[7] P.W. Arnold, "The slant antenna range", IEEE Trans. Antennas Propag., Vol. AP-14, pp. 658-659, Sept. 1966.

[8] L.H. Hemming and R.A. Heaton, "Antenna deisgn calibration on a ground reflection range", IEEE Trans. Antennas Propag., Vol. AP-21, pp. 532-537, July 1973.

[9] W.H. Kummer and E.S. Gillespie, "Antenna measurements 1978", Proc. of IEEE, Vol. 66, pp. 483-507, April 1978.

[10] W.H. Emerson, "Electromagnetic wave absorbers and anechoic chambers through the years", IEEE Trans. Antennas Propag., Vol. AP-21, pp. 484-490, July 1973.

[11] J. Appel-Hensen, "Reflectivity level of radio-anechoic chambers", IEEE Trans. Antennas Propag., Vol. AP-21, pp. 490-498, July 1973.

[12] W.H. Emerson and H.B. Sefton, "An improved design for indoor ranges", Proc. IEEE, Vol. 53, pp. 1079-1081, Aug. 1965.

[13] R.C. Johnson, H.A. Ecker and R.A. Moore, "Compact range techniques and measurements", IEEE Trans. Antennas and Propag., Vol. AP-17, pp. 568-576, Sept. 1969.

[14] D.W. Hess, F.G. Willwerth and R.C. Johnson, "Compact range improvements at 30 GHz", in 1977 Int. IEEE/AP-S Symp. Dig., pp. 264-267, June 1977.

[15] A.D. Olver, "The practical performance of compact antenna ranges", European Space Agency, Proc. Workshop on Antenna Testing Techniques, Noordwijk, Netherlands, pp. 129-133, June 1977.

[16] Scientific Atlanta Inc., "The compact range", Microwave Journals, Vol. 17, pp. 30-32, Oct. 1974.

[17] P.F. Wacker and A.C. Newell, "Advantages and disadvantages of planar, circular cylindrical, and spherical scanning and description of the NBS antenna scanning facilities", European Space Agency, Proc. Workshop on Antenna Testing Techniques, Noordwijk, Netherlands, pp. 115-121, June 1977.

[18] S. Silver, Microwave Antenna Theory and Design, (Rad. Lab. Ser. 12), McGraw-Hill Book Co., Inc., New York, 1949, Sec. 3-8.

[19] C.T. Tai, "Kirchoff Theory: scalar, vector, or dyadic?", IEEE Trans. Antennas Propag., Vol. AP-20, pp. 114-115, Jan. 1972.

[20] J. Appel-Hansen, Lecture notes on planar, cylindrical and spherical near-field scanning techniques in antenna measurements, Tech. Univ. of Denmark, Lyngby, July 1979.

[21] R.F. Harrington, Time-Harmonic Electromagnetic Fields, McGraw-Hill Book Co., Inc., New York, 1961.

[22] E.B. Joy and D.G. Bodnar, "Near-field antenna measurement activities at Georgia Tech", IEEE Newsletter Antenna Propag., Vol. 21, pp. 5-7, April 1979.

[23] E.B. Joy and D.T. Paris, "Spatial sampling and filtering in near-field measurements", IEEE Trans. Antennas Propag., Vol. AP-20, pp. 253-261, May 1972.

[24] D.T. Paris, W.M. Leach, Jr. and E.B. Joy, "Basic theory of probe-compensated near-field measurements", IEEE Trans. Antennas Propag., Vol. AP-26, pp. 373-379, May 1978.

[25] J.D. Brown and E.V. Jull, "The prediction of aerial radiation patterns from near-field measurements", Proc. IEE (London), Vol. 108, pt. B, pp. 635-644, Nov. 1961.

[26] W.M. Leach, Jr. and D.T. Paris, "Probe compensated near-field measurements on a cylinder", IEEE Trans. Antennas Propag., Vol. AP-21, pp. 435-445, July 1973.

[27] J. Appel-Hansen, "On cylindrical near-field scanning techniques", IEEE Trans. Antennas Propag., Vol. AP-28, pp. 231-234, March 1980.

[28] H.C. Minnett and B. MacA. Thomas, "Fields in the image space of symmetrical focusing reflectors", Proc. IEE (London), Vol. 115, pp. 1419-1430, Oct. 1968.

[29] F. Jensen, "Electromagnetic near-field far-field correlations", Ph.D. dissertation, LD15, Lab. of Electromagnetic Theory, Tech. Univ. of Denmark, Lyngby, July 1970.

[30] F. Jensen, "Spherical near-field technique", in 1977 Int. IEEE/AP-S Symp. Dig., pp. 378-381, June 1977.

[31] F. Jensen, "On the probe compensation for near-field measurements on a sphere", Archiv für Electronik und Übertragung Stechnik (Electronics and Communications), Vol. 29, No. 718, pp. 305-308, July/August 1975.

[32] F.H. Larson, "Probe correction of spherical near-field measurements", Elect. Letters, Vol. 13, No. 14, pp. 393-395, July 1977.

[33] A.C. Ludwig, "Near-field far-field transformation using spherical wave expansions", IEEE Trans. Antennas Propag., Vol. AP-19, pp. 214-220, Mar. 1971.

[34] A.C. Ludwig, "Spherical Wave Theory", Report No. NB119, Tech. Univ. of Denmark, Lyngby, Oct. 1978.

[35] A.C. Newell and A. Repjar, "Results of spherical near-field measurements on narrow beam antennas", in 1977 Int. IEEE/AP-S Symp. Dig., pp. 382-385, June 1977.

[36] P.D. Potter, "Application of spherical wave theory to Cassegrainian fed paraboloids", IEEE Trans. Antennas Propag., Vol. AP-15, pp. 727-736, Nov. 1967.

[37] J.A. Stratton, Electromagnetic Theory, McGraw-Hill Book Co., Inc., New York, 1941.

[38] P.J. Wood, "Spherical waves in antenna problems", Marconi Review, Vol. 34, No. 182, pp. 149-172, 1971.

[39] E.B. Joy, W.M. Leach, G.P. Rodrigue, and D.M. Paris, "Applications of probe-compensated near-field measurements", IEEE Trans. Antennas Propag., Vol. AP-26, pp. 379-389, May 1978.

[40] M.B. El-Arini and L. Shafai, "Field measurements using scattering data from a dielectric cylinder", submitted to Canadian Electrical Engineering Journal, 1980.

[41] M.B. El-Arini and L. Shafai, "Computer programs for solving the two- and three-dimensional inverse source problems in presence of a dielectric scatterer", Department of Electrical Engineering, University of Manitoba, Winnipeg, Canada, Report No. TR80-9, 1980.

[42] W.M. Boerner, F.H. Vandenberghe and M.A.K. Hamid, "Determination of the Electrical radius ka of a circular cylindrical scatterer from the scattered field", Can. J. of Physics, Vol. 49, pp. 804-819, 1971.

[43] W.M. Boerner and F.H. Vandenberghe, "Determination of the Electrical radius ka of a spherical scatterer from the scattered field", Can. J. of Physics, Vol. 49, pp. 1507-1535, 1971.

[44] J.D. Kraus, Antennas, McGraw-Hill Book Co., Inc., New York, 1950.

[45] M. Abramowitz and I.A. Stegun, Handbook of Mathematical Functions with Formulas, Graphs, and Mathematical Tables, Nat. Bureau of Standards, App. Math. Series, Vol. 55, U.S. Govt. Printing Office, 1964.

[46] M.B. El-Arini and L. Shafai, "A stepwise scanning method for generation of antenna near fields", submitted to IEEE Trans. Antennas Propag., 1980.

[47] D.S. Jones, The Theory of Electromagnetism, McMillan Co., Sec. 8-16, New York, 1964.

[48] M.V. Bradford, "The electromagnetic radiation from simple sources in the presence of a homogeneous dielectric sphere", Ph.D. dissertation, University of Michigan, 1972.